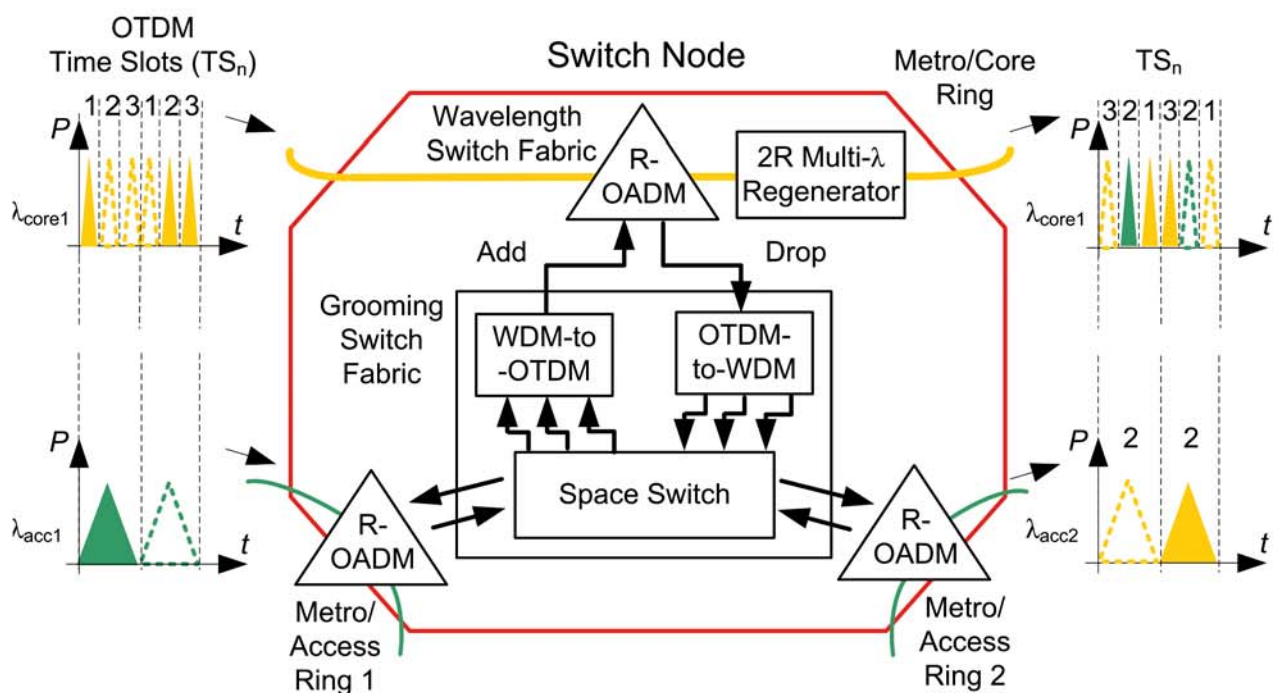


Philipp Vorreau

An Optical Grooming Switch for High-Speed Traffic Aggregation in Time, Space and Wavelength



Philipp Vorreau

**An Optical Grooming Switch for High-Speed Traffic Aggregation
in Time, Space and Wavelength**

Karlsruhe Series in Photonics & Communications, Vol. 6
Edited by Prof. J. Leuthold and Prof. W. Freude

Karlsruhe Institute of Technology,
Institute of Photonics and Quantum Electronics (IPQ)
Germany

An Optical Grooming Switch for High-Speed Traffic Aggregation in Time, Space and Wavelength

by
Philipp Vorreau

Dissertation, Universität Karlsruhe (TH)
Fakultät für Elektrotechnik und Informationstechnik, 2009

Impressum

Karlsruher Institut für Technologie (KIT)
KIT Scientific Publishing
Straße am Forum 2
D-76131 Karlsruhe
www.uvka.de

KIT – Universität des Landes Baden-Württemberg und nationales
Forschungszentrum in der Helmholtz-Gemeinschaft



Diese Veröffentlichung ist im Internet unter folgender Creative Commons-Lizenz
publiziert: <http://creativecommons.org/licenses/by-nc-nd/3.0/de/>

KIT Scientific Publishing 2010
Print on Demand

ISSN: 1865-1100
ISBN: 978-3-86644-502-4

An Optical Grooming Switch for High-Speed Traffic Aggregation in Time, Space and Wavelength

Zur Erlangung des akademischen Grades eines

DOKTOR-INGENIEURS

von der Fakultät für
Elektrotechnik und Informationstechnik
der Universität Karlsruhe (TH)

genehmigte

DISSERTATION

von

Dipl.-Ing. (FH) Philipp Vorreau

geboren in Hamburg

Tag der mündlichen Prüfung:

28. Juli 2009

Hauptreferent:

Prof. Dr. sc. nat. Jürg Leuthold

Korreferenten:

Prof. Dr.-Ing. Dr. h. c. Wolfgang Freude

Prof. Dr. rer. nat. Uli Lemmer

Contents

Contents.....	i
List of Figures.....	v
List of Tables.....	vii
Abstract (German).....	ix
Preface.....	1
1 Optical Transport Networks	5
1.1 Review of Existing Metro Network Implementations	5
1.1.1 Optical Transport Networks	6
1.1.2 Metropolitan Area Networks.....	7
1.2 The Metro Gap - Future MAN Requirements.....	9
1.2.1 Transparent Traffic Grooming	10
1.2.2 Flexibility	11
1.2.3 Scalability.....	11
1.2.4 Energy Efficiency.....	11
1.2.5 Regeneration.....	11
1.2.6 Multi-wavelength Operation	11
1.3 Summary	12
2 The Novel Optical Switch Node	13
2.1 Definition of the Network Architecture and Signal Structure.....	14
2.1.1 Metro Network Architecture	14
2.1.2 Signal Structure and Conditions.....	15
2.2 Definition of the Switch Node Architecture	17
2.3 Summary	19
3 Test Setups and Measurement Techniques.....	21
3.1 Signal Degradation in Optical High-Speed Systems.....	21
3.2 Mach-Zehnder Modulators.....	23
3.3 RZ-OOK 43 Gbit/s Transmitter and Receiver	26
3.3.1 Transmitter	26
3.3.2 Receiver with Optical Preamplifier.....	27
3.4 130 Gbit/s RZ-OOK OTDM Transmitter and Receiver.....	28
3.4.1 Time Multiplex.....	28
3.4.2 Short Pulse Sources.....	28
3.4.3 Lab Implementation of the Time Division Multiplexer.....	29
3.4.4 Time Demultiplex and Receiver	30
3.5 43 Gbit/s RZ-DPSK Transmitter and Receiver.....	31
3.5.1 Transmitter	31

3.5.2	Balanced Receiver	32
3.6	Methods for System Performance Characterization.....	33
4	WDM-to-OTDM Conversion	35
4.1	Introduction	35
4.2	Asynchronous Digital Optical Regeneration.....	35
4.2.1	Asynchronous Retiming and Connectivity	35
4.2.2	Operating Principle	37
4.2.3	Implementation.....	38
4.2.4	OTDM multiplexing.....	40
4.2.5	Network Reach.....	40
4.3	Experiment	42
4.4	Results and Discussion.....	43
4.5	Summary	44
5	OTDM-to-WDM Conversion	45
5.1	Introduction	45
5.2	SPM Based OTDM-to-WDM Conversion.....	47
5.2.1	Operation Principle	47
5.2.2	Scalability.....	47
5.2.3	Experimental Setup	48
5.2.4	Results and Discussion.....	49
5.3	XPM-based OTDM-to-WDM Conversion using an NOLM	52
5.3.1	Operation Principle	52
5.3.2	Scalability.....	54
5.3.3	Experimental Setup	55
5.3.4	Results and Discussion.....	56
5.4	Conclusions	57
6	Optical Clock Recovery	59
6.1	Fundamentals	60
6.1.1	Oscillating Frequency Dividers.....	60
6.1.2	The Injection Locked Oscillator as a Clock Recovery.....	63
6.2	Implementation of the Clock Recovery	64
6.2.1	Choice of the Critical Components	65
6.2.2	Locking of the Optoelectronic Oscillator.....	66
6.3	Results	68
6.3.1	Free Running Oscillator	68
6.3.2	Optoelectronic Oscillator as Clock Recovery	71
6.3.3	Scalability.....	74
6.4	Comparison with Results from Literature.....	74
6.5	Summary	75
7	All-Optical Signal Regenerators	77
7.1	Fiber-Based Multi-Wavelength Regenerators.....	78
7.1.1	Fundamentals	78

7.1.2	Multi-Wavelength Regeneration of 43 Gbit/s WDM Channels.....	80
7.1.3	2R Regeneration of Two Counterpropagating 130 Gbit/s Channels.....	85
7.2	SOA-MZI based Regenerator for DPSK Signals.....	90
7.2.1	Introduction.....	90
7.2.2	DPSK Wavelength Conversion Scheme and Experiment.....	90
7.2.3	Cascadability.....	92
7.2.4	Regenerative Properties.....	93
7.3	Summary.....	95
8	Switch Node Demonstration.....	97
8.1	Introduction.....	97
8.2	Testbed Implementation.....	98
8.3	Results and Discussion.....	100
8.4	Switch Node Scalability and Cascadability.....	103
8.5	Summary.....	105
9	Achievements and Outlook.....	107
	Appendix.....	109
	A 1 Methods for System Performance Characterization.....	109
A 1.1	Bit-Error Ratio Measurements.....	109
A 1.2	Q-Factor Measurements.....	111
	A 2 Fiber Nonlinearities.....	112
A 2.1	Nonlinear Phase Modulation.....	112
A 2.2	Self-Phase Modulation.....	112
A 2.3	Cross-Phase Modulation.....	113
	Glossary.....	115
	Symbols.....	119
	Bibliography.....	121
	Acknowledgements (German).....	129
	List of Own Publications.....	131
	Patents.....	131
	Journal Papers.....	131
	Conference Contributions.....	132
	Curriculum Vitae.....	137

List of Figures

Fig. 1.1. (a) The optical transport network with its different coverage areas.	7
Fig. 1.2. Optical cross connect with N input fibers.	8
Fig. 1.3. Reconfigurable optical add-drop multiplexer with one input fiber.	9
Fig. 2.1. Metro network scenario.	14
Fig. 2.2. Conceptual diagram of a slotted network.	16
Fig. 2.3. Switch node block diagram.	17
Fig. 3.1. Principle setup of a push-pull Mach-Zehnder modulator.	23
Fig. 3.2. Amplitude $E(t)$ and power transfer function $P(t)$ of a Mach-Zehnder modulator.	24
Fig. 3.3. 127 bit long pseudo random bit sequence ($2^7 - 1$ bits).	25
Fig. 3.4. Experimental setup of 43 Gbit/s RZ-OOK transmitter.	26
Fig. 3.5. Setup of the receiver with optical preamplifier.	27
Fig. 3.6. Setup of a 43 Gbit/s to 130 Gbit/s OTDM multiplexer.	29
Fig. 3.7. Typical FWHM pulse width of the EAM for different bias voltages.	31
Fig. 3.8. Setup of the 43 Gbit/s DPSK transmitter.	32
Fig. 3.9. Setup of the balanced receiver with optical preamplifier.	33
Fig. 4.1. Functional diagram of a dual-gate ADORE.	37
Fig. 4.2. Experimental setup of the 42.7 Gbit/s dual-gate ADORE.	38
Fig. 4.3. WDM-to-OTDM traffic grooming utilizing the asynchronous retiming concept.	40
Fig. 4.4. Experimental implementation of the WDM-to-OTDM conversion.	42
Fig. 4.5. Receiver bit error rate measurements for the three OTDM tributaries.	43
Fig. 5.1. Operation principle of the OTDM to WDM conversion.	47
Fig. 5.2. Experimental implementation of the OTDM-to-WDM conversion.	48
Fig. 5.3. Signals at various positions in the OTDM-to-WDM setup.	49
Fig. 5.4. Optical spectra at various positions in the OTDM-to-WDM setup.	50
Fig. 5.5. Eye diagrams of the demultiplexed signals forming the WDM channels.	50
Fig. 5.6. Bit error rates of the three 43 Gbit/s outputs of the OTDM-to-WDM subsystem.	51
Fig. 5.7 Operation principle of the OTDM-to-WDM conversion technique.	52
Fig. 5.8. Experimental setup of the TDM-to-WDM conversion.	55
Fig. 5.9. BER and receiver sensitivity of each WDM channel.	57
Fig. 6.1. General model of an LC oscillator as a positive feedback loop.	60
Fig. 6.2. Adler's injection-locking oscillator circuit.	61

Fig. 6.3. Schematic illustration of locking range ω_1	62
Fig. 6.4. Implementation of the optoelectronic oscillator used for the clock recovery.....	64
Fig. 6.5. Setup for the experimental study of the free running oscillator.....	68
Fig. 6.6. RF spectrum of the free running oscillator.	68
Fig. 6.7. Time-averaged RF spectrum of the free running oscillator.	69
Fig. 6.8. Experimental setup to study the bandpass characteristic of the O-E oscillator.	70
Fig. 6.9. Transmission characteristic of the opto-electronic oscillator.	70
Fig. 6.10. Experimental setup for characterization of the clock recovery.	71
Fig. 6.11. Eye diagram of the OTDM signal and RF spectrum of the recovered clock.....	72
Fig. 6.12. Single side band phase noise jitter performance of the clock recovery.....	73
Fig. 7.1. Schematic of an optical regenerator based on SPM and offset filtering.....	78
Fig. 7.2. Schematic illustration of optical power transfer function.....	79
Fig. 7.3. Schematic of the dispersion-managed -regenerator.....	81
Fig. 7.4. Experimental setup of the 2R regeneration experiment with 3×43 Gbit/s signals. .	81
Fig. 7.5. Fiber parameters and chromatic dispersion map of the whole fiber assembly.	82
Fig. 7.6. Experimental average-power transfer functions.	83
Fig. 7.7. BER measurements in single- and dual-channel operation (1200 GHz spacing).....	83
Fig. 7.8. Q and BER measurements in three-channel operation (600 GHz spacing).....	84
Fig. 7.9. Schematic of the bi-directional regenerator.....	85
Fig. 7.10. Experimental setup for counter-propagation scheme.	86
Fig. 7.11. Average power transfer functions of Channel 1 and Channel 2.....	87
Fig. 7.12. BER curves for the undistorted and distorted back-to-back signals.....	88
Fig. 7.13. Setup with DPSK transmitter, wavelength converter, and differential receiver.....	91
Fig. 7.14. Logic operation performed by the differential encoder and the optical DI.	92
Fig. 7.15. Effect on DPSK output power and output phase if a distorted bit is introduced.....	93
Fig. 7.16. Constellation diagrams of DPSK input signals and phase-encoded output signals. 94	
Fig. 7.17. Evolution of signal quality with number of DPSK wavelength converter laps.	95
Fig. 8.1. Functional diagram of the testbed.....	98
Fig. 8.2. Node architecture for switching scenario 1.	100
Fig. 8.3. Optical spectra, eye diagrams and Q-factors at various points of the setup.	101
Fig. 8.4. Table with three switching scenarios giving time slot constellations.....	102
Fig. 8.5. BER measurements for switching scenario 1.	103
Fig. 8.6. Node architecture for an advanced capacity scenario.....	104
Fig. A.1. Possible differences when comparing two bit error ratio curves.....	110

List of Tables

Table 6.1. Combination of harmonics that can lead to injection locking.....	67
Table 6.2. Characteristic parameters of the clock recovery.	74
Table 6.3. σ_{RMS} and input bitrate referred phase noise (IBRPN) of the oscillator.	75

Abstract (German)

Die vorliegende Arbeit befasst sich mit der hochbitratigen Anbindung von zukünftigen optischen Kern- und Stadtbereichsnetzen. Zur Anbindung dieser Netze bedarf es neuer optischer Netzwerkknoten, die große Datenmengen unabhängig von der Anwendung auf transparente, energieeffiziente und flexible Weise vermitteln. In dieser Arbeit wird ein neuartiger optischer Vermittlungsknoten zur speicherfreien Anbindung von Kern- und Metronetzwerken mit Schaltfunktionalitäten im Zeit-, Raum-, und Frequenzbereich vorgeschlagen, aufgebaut und experimentell untersucht. Dabei werden neuartige Konzepte für die Bereitstellung der Kernfunktionalitäten des Knotens entwickelt: Bündelung von Datenströmen mit Zeitschlitzvertauschung, Umsetzung von Wellenlängenmultiplex (engl. wavelength division multiplexing - WDM) in optischen Zeitmultiplex (engl. optical time division multiplexing - OTDM) und umgekehrt, sowie die gleichzeitige Regeneration mehrerer hochbitratiger Signale.

Im Rahmen der Arbeit werden zunächst die grundlegenden Eigenschaften von heutigen optischen Transportnetzwerken vorgestellt. Basierend darauf werden die Anforderungen an zukünftige Stadtbereichsnetze im Hinblick auf Kanaldatenraten, Transparenz, Flexibilität, Energieeffizienz und Mehrwellenlängenfähigkeit analysiert.

Der vorgeschlagene Vermittlungsknoten erfordert die gleichzeitige Synchronisation von mehreren 43 Gbit/s WDM Kanälen und die anschließende Umsetzung in ein 130 Gbit/s-OTDM-Signal. Zum ersten Mal wird im Rahmen der vorliegenden Arbeit die Auswirkung von speicherfreier optischer Synchronisierung im Rahmen eines 3×43 Gbit/s WDM auf 130 Gbit/s OTDM Konversionsexperiments untersucht. Es wird nachgewiesen, dass die gleichzeitige Synchronisierung mehrerer Kanäle bei einer vernachlässigbaren Leistungsabnahme von 1.0 dB unabhängig voneinander betrachtet werden kann.

Eine weitere Schlüsselfunktion des Vermittlungsknotens ist die Abbildung eines OTDM-Signals auf mehrere WDM-Kanäle. Praxisgerechte Lösungen müssen die Umsetzung aller OTDM Zeitschlitz in einer einzelnen Baugruppe ermöglichen. Im Bezug auf diese Anforderung werden im Rahmen der vorliegenden Arbeit zwei unterschiedliche Verfahren zur OTDM-WDM Umsetzung untersucht. Beide Verfahren basieren auf der Verwendung von hoch nichtlinearer Faser (engl. highly non-linear fiber - HNLF) und setzen ein 130 Gbit/s-Eingangssignal in drei 43 Gbit/s-Ausgangssignale um.

Im ersten Verfahren wird die HNLF als Teil eines nichtlinearen optischen Ringreflektors verwendet. Drei unterschiedliche WDM-Taktsignale werden in den Ringreflektor gekoppelt. Ein gleichzeitig injizierter Hochleistungspuls des OTDM-Datensignals führt zu einer Phasenänderung von π durch Kreuzphasenmodulation in der HNLF. Dadurch wird am Ausgangsarm des Ringreflektors die Information jedes OTDM-Kanals auf eine spezifische Wellenlänge umgesetzt. Erstmals wird in der vorliegenden Arbeit mit dieser Technik die gleichzeitige Um-

setzung von 130 Gbit/s in 3×43 Gbit/s gezeigt. Experimentell wird die fehlerfreie Funktion der Baugruppe mit Leistungsbußen von 0.5 dB bis 3.5 dB für die WDM-Kanäle nachgewiesen.

In der zweiten Lösung wird das 130 Gbit/s-OTDM-Signal zunächst auf drei Wellenlängen umgesetzt, danach um jeweils ein Bit zueinander verzögert und dann mit 43 Gbit/s abgetastet, um die WDM-Signale zu erhalten. Für die Wellenlängenumsetzung wird eine Technik verwendet, die auf der Filterung von durch Selbstphasenmodulation verbreiterten Spektren beruht (auch bekannt unter dem Namen Mamyshev-Regenerator). Beide vorgestellten Verfahren zeigen in Abhängigkeit der konkreten Anwendung unterschiedliche Vor- und Nachteile. Für den Prototyp des Vermittlungsknotens wird aufgrund des einfacheren Aufbaus und des stabileren Verhaltens die zweite Lösung verwendet.

Beide OTDM-WDM-Umsetzungsverfahren benötigen die zeitliche Abtastung bei einer Frequenz von 43 GHz. In der vorliegenden Arbeit wird deshalb eine Taktrückgewinnung geplant und aufgebaut, die das Taktsignal mit einer zum Eingangssignal subharmonischen Frequenz von 43 GHz zur Verfügung stellt. Das Verfahren basiert auf einem injektionsgekoppelten opto-elektronischen Oszillator. Der quadratische Mittelwert des Jitters des extrahierten Takts ist mit $\sigma_{\text{RMS}} = 72$ fs sehr klein. Das exzellente Resultat wird in Kombination mit der OTDM-WDM-Baugruppe bestätigt und eine Einbettung der Ergebnisse in die Theorie injektionsgekoppelter Oszillatoren vorgenommen.

Zur rein optischen Regeneration von hochbitratigen Signalen werden drei neuartige Methoden implementiert und experimentell untersucht. Als erste Lösung wird das bekannte Mamyshev-Verfahren auf Mehrwellenlängenbetrieb erweitert und eine Technik zur gleichzeitigen Regeneration von drei intensitätsmodulierten 43 Gbit/s-Kanälen vorgeschlagen. Bei diesem Verfahren laufen die Kanäle in gleicher Richtung durch eine Faser mit einem speziell entwickelten Dispersionsprofil, die das nichtlineare Übersprechen der Kanäle stark reduziert. Im Zweikanalbetrieb mit einem Kanalabstand von 1200 GHz wird eine Verbesserung der Leistungsbuße um 2.5 dB gegenüber einem qualitativ schlechten Eingangssignal erreicht.

Als zweite Lösung wird ein bidirektionaler Aufbau für die gleichzeitige Regeneration von zwei 130 Gbit/s-Kanälen vorgeschlagen. Im Experiment wird keine Verschlechterung der Regeneration durch die Gegenwart des zweiten Kanals beobachtet. Dieses Experiment stellt die bisher höchste Zweikanalregeneration überhaupt dar und wird ermöglicht durch eine sehr sorgfältige Wahl der HNLF-Parameter.

Optische Phasenmodulation ist aufgrund der höheren Toleranz gegenüber Fasernichtlinearitäten und der höheren Empfängerempfindlichkeit für bestimmte Übertragungssysteme eine interessante Alternative zur Intensitätsmodulation. Deshalb wird, basierend auf interferometrisch angeordneten optischen Halbleiterverstärkern, als drittes Verfahren ein neuartiger Regenerator und Wellenlängenumsetzer für phasenmodulierte Signale entwickelt. Die Machbarkeit des Konzepts wird experimentell bei Bitraten von 25 Gbit/s bis 40 Gbit/s bestätigt und die Grenzen des Konzepts diskutiert.

Nach der Entwicklung der einzelnen Baugruppen liegt die Herausforderung in der Zusammenführung der verschiedenen Technologien auf das gleiche Wellenlängenraster und im Auf-

bau des kompletten optischen Vermittlungsknotens mit allen Funktionalitäten. Die experimentelle Untersuchung vieler Schaltszenarien im Labortest (ohne Übertragungsstrecke) demonstriert alle Funktionalitäten des neuartigen Vermittlungsknotens und bestätigt damit die exzellenten Eigenschaften der vorgeschlagenen Lösung. Fehlerfreie Datenvermittlung mit Q-Faktoren von über 21 dB für alle Schaltszenarien wurde erreicht.

Preface

The rising popularity of the internet, voice over internet protocol (VoIP), and IP television (IPTV) has changed the landscape of optical telecommunications networks. Several new challenges are evolving in terms of technology, applications, services, and business models. Wide area networks, on one hand, are optimized for transmission, and their capacity has increased by orders of magnitude in recent years, thanks to innovations in optical transmission and especially in wavelength division multiplexing (WDM) technology. On the other hand, because of the growing number of applications in the communications networks of today, access networks use a very broad range of protocols, which constantly evolve. In recent years, residential cable, digital subscriber line (DSL) modems have increased user access rates from kilobits to megabits, and new emerging technologies promise even higher data rates per user (e.g. fiber to the home - FTTH). These technological leaps in the backbone and access parts of the network have not been matched so far with progress in the metro part. This is why the literature refers to the “metro gap” [1],[2], meaning that metropolitan area networks (MANs) will need an upgrade in order to cope with future traffic demands.

However, in order to deal with the increase in data traffic, 40 Gbit/s is emerging as a viable and important bit rate in future metro networks. More specifically, the international telecommunications union (ITU) defined optical transport units (OTUs) with OTU3 having a line rate of approximately 43 Gbit/s. In addition, 100GE is being standardized by IEEE P802.3ba task force for links up to 40 km. It is expected that such traffic will be transported in the core network in serial form using OTU4 containers (currently under development in ITU-T study group 15). OTU4 containers will also be dimensioned for the transport of multiple OTU3's, resulting in a line rate close to 130 Gbit/s. Therefore, grooming from lower 43 Gbit/s bit rates to 130 Gbit/s through optical time-division multiplexing (OTDM) by the edge switch node will be required when moving from metro to core networks. In addition, protocol transparency becomes a key requirement in metro networks access networks due to the constantly growing number of protocols used. Technically this is not a simple task, and has various implications related with the physical implementation and performance.

However, dynamic sub-wavelength grooming functionalities are currently unavailable in the optical layer, and will be required when jumping to 130 Gbit/s data rates. Network studies have shown that deploying alternatives to electronic grooming potentially will have the largest impact on reducing overall network cost [3].

This thesis focuses on high capacity ring interconnection between metro-core, carrying 130 Gbit/s OTDM traffic, and metro access-rings carrying 43 Gbit/s WDM traffic. More specifically, we design, develop and test a novel optical switch that integrates optical switching, transparent traffic aggregation/grooming and optical regeneration. Innovative node subsystems are developed in this thesis enabling these functionalities, including: all-optical multi-

wavelength regenerators, all-optical OTDM-to-WDM converters with clock recovery, and opto-electronic WDM-to-OTDM converters. The proposed switch node features flexibility in bandwidth provisioning, scalability to higher traffic volumes, and backward compatibility with existing MAN implementations in a future-proof way.

The thesis is structured as follows: In Chapter 1, we review the existing solutions for global and in particular metro network architectures. In addition, the existing and emerging applications that future networks should support are identified and the requirements for these future MANs both in terms of capacity and features are derived.

In Chapter 2, we define the proposed architecture for next-generation MANs, which is based on upgrading the current implementation. We then discuss three possible signal structures that are considered in this work, which are: circuit switched traffic carried over continuous connections, circuit switched traffic carried over a burst mode transport layer, and burst mode traffic. The proposed switch node architecture is defined which integrates all the crucial functionalities that are currently provided by digital cross-connects, i.e. switching, traffic aggregation/grooming and regeneration in the optical layer. The findings of this chapter have been published in a journal article (J6) and international conference contributions (C29, C21). All publications are summarized on pp. 131.

The testing of optical high-speed systems is a highly complex task, and results always have to be understood in the context of the corresponding test system. For this reason, Chapter 1 gives detailed information on the test setups and techniques that are used in this work. However, the discussion of methods and limitations of bit-error ratio and Q-factor measurements and a brief discussion of fiber nonlinearities are shifted to the Appendices A 1 and A 2, respectively.

The switch node proposed in this thesis requires retiming of multiple WDM channels and subsequent WDM-to-OTDM conversion for interconnecting 43 Gbit/s and 130 Gbit/s network rings. In Chapter 4, we experimentally investigate for the first time the impact of asynchronous retiming in a 3×43 Gbit/s to 130 Gbit/s buffer-less WDM-to-OTDM traffic grooming experiment. We confirm that a number of asynchronous digital optical regenerators employed in parallel may be considered independently with a negligible power penalty of 1.0 dB associated with clock phase tuning of adjacent channels. In addition, the potential network reach for this concept is discussed. The findings of this chapter have been published in an international conference contribution (C31). A journal article including these results has been submitted.

Another key functionality of the switch node is mapping of an OTDM signal to different WDM channels. A practical solution requires simultaneous demultiplexing of all OTDM channels with a single device. In Chapter 5, we propose and experimentally demonstrate two different OTDM-to-WDM conversion schemes based on highly-nonlinear fibers, which convert a 130 Gbit/s OTDM signal to three 43 Gbit/s WDM signals.

For the first solution, the HNLF is included inside a nonlinear optical loop mirror (NOLM). Three different WDM probe pulse streams were input to the NOLM, and the OTDM signal was used as a control signal to switch the time interleaved WDM probes. Using this technique, we report the first demonstration of OTDM-to-WDM conversion from 130 Gbit/s simultaneously to three 43 Gbit/s WDM channels. Error free performance is achieved with

power penalties ranging from 0.5 dB to 3.5 dB for all three WDM channels. This solution enables full flexibility for selecting the output WDM channel wavelengths as required in future all-optical networks. The results have been published in an international conference contribution (C25).

For the second solution, a 130 Gbit/s OTDM signal is replicated in three copies at different wavelengths, and the resulting signals are delayed to achieve relative timing shifts of one bit period followed by time gating to obtain the WDM signal. For the multi-wavelength conversion we used the technique developed by Mamyshev [4], which is based on offset filtering of a self-phase-modulation (SPM) broadened spectrum.

While good performance is achieved with both configurations, the two schemes present advantages and disadvantages. For the system demonstration of the switch node, the second approach is chosen because of the simpler setup, ease of operation and because of better long-term stability.

Both OTDM-to-WDM solutions require optical time gating at the tributary bit rate. Therefore we report in Chapter 6 on the design and demonstration of a 43 GHz sub-harmonic optical clock recovery from 130 Gbit/s data streams, which is based on an injection-locked optoelectronic oscillator. The RMS timing jitter of the recovered clock is as low as $\sigma_{\text{RMS}} = 72$ fs (100 Hz – 1 MHz). The minimum average optical power of the data input signal required for stable injection locking was $P_{\text{data}} = 5.0$ dBm with a dynamic range of 5 dB. The excellent performance of the clock recovery is verified by using it in combination with the OTDM-to-WDM subsystem.

In Chapter 7, we propose three different methods for high-speed all-optical regeneration. As a first solution, we extend the Mamyshev approach for single-wavelength operation and propose a 43 Gbit/s multi-wavelength scheme for regenerating up to three 43 Gbit/s intensity-modulated channels. This technique is based on co-propagation of the channels in the fiber with a carefully designed dispersion map for reducing the nonlinear inter-channel cross-talk. In dual-channel operation with 1200 GHz channel spacing we achieve a power penalty improvement of 2.5 dB for a degraded input signal. The results have been published in a journal article (J5) and an international conference contribution (C27).

As a second solution, a bi-directional scheme is exploited to demonstrate the simultaneous regeneration of two 130 Gbit/s intensity-modulated channels. No degradation was observed due to the presence of the second channel. This represents the highest speed dual-channel regenerator ever reported in a single fiber and is made possible by a very careful choice of the HNLF parameters. The results have been published in an international conference contribution (C33) and will be included in a journal article that has been submitted.

Offering improved sensitivity and robustness to nonlinear impairments as compared to pure intensity modulation, differential phase shift keying is becoming another modulation format of choice for future networks [5]. Therefore, the last section of the chapter is dedicated to a novel SOA-based Mach-Zehnder interferometer (MZI) wavelength converter and regenerator for differentially phase-modulated signals. In an experiment we show the feasibility and predict the limits of the reamplifying, retiming and reshaping (3R) all-optical DPSK wavelength

converter. We further discuss how this device can be cascaded an arbitrary number of times. The results of this subchapter have been published in a journal article (J3) and an international conference contribution (C6).

After introducing and experimentally characterizing all switch node subsystems, the challenge was to make all the different optical technologies work on a common wavelength grid, assemble the optical switch node with its functionalities and perform testing at bit-rates of 43 Gbit/s and 130 Gbit/s. Chapter 8 reports the results of the experimental demonstration with multiplexing in frequency and time. The excellent performance of the proposed solution is verified by studying a manifold of switching scenarios, showing dynamic bandwidth allocation for time-varying traffic demands. Q-factors are above 21 dB, and error free performance is achieved. In addition, the scalability of the proposed switch node in terms of channel bit-rates and port-count as well as its cascadability is discussed. The findings in this chapter have been published in a conference contribution (C29). A journal article has been submitted.

Chapter 9 finally summarizes the main achievements of the work.

1 Optical Transport Networks

An optical transport network is composed of interconnected nodes (also called network elements), software, and operation processes that must function together to provide services [1]. The optical communication network extends over several point-to-point links and comprises several nodes. It can be divided into different coverage areas, represented by network planes operating on top of each other: wide-area networks (WAN), metropolitan-area networks (MAN), and access networks.

In this chapter, we introduce the basic characteristics of state-of-the-art optical transport networks. First, we introduce the concept of a global network. We then concentrate on metro networks in terms of their architecture, protocols, network elements, and the underlying physical layer. We introduce the concepts of optical cross-connects (OXC) and optical add-drop multiplexers (OADMs) as primary optical network elements and we discuss their traffic grooming capabilities. In addition, the limitations of MANs in terms of capacity, scalability and flexibility are identified. This part of the chapter can be considered standard knowledge and is subject of various textbooks. Particularly comprehensive presentations of legacy metro networks can be found in [6] and [7]. Traffic grooming in optical networks is studied in detail in [2].

Next, we identify the major applications and service drivers of next generation access and metro networks. The improvement of access technologies on the end-user side will help delivering high-bandwidth to satisfy the demand growth brought by new applications. At the same time, in the regional/long-haul network, several technologies are mature enough to guarantee high connectivity and supply the high bandwidth requirements of lower network levels. Based on the discussion on legacy metro networks it becomes clear that new metro solutions are required that offer superior price/performance alternatives over legacy solutions. We point out the requirements for these future MANs both in terms of capacity and features such as flexibility, scalability, energy efficiency, etc.

This subchapter is structured as follows: Section 1.1 reviews the existing solutions for global and in particular metro network architectures. Section 1.2 identifies the existing and emerging applications that future networks should support, and it identifies the requirements for these future MANs both in terms of capacity and features.

1.1 Review of Existing Metro Network Implementations

To avoid confusion, let us first define some fundamental terms that will be used in this work.

All-Optical: The term all-optical means that optical signals are transmitted without any intermediate optical/electrical/optical (OEO) conversion. As a matter of fact, it is most appro-

privately used for devices that traditionally would be expected to operate electronically but now have been replaced by a device that operates all-optically. We follow this convention.

Transparency: A network is transparent if the signals are transmitted optically from source to destination. Actually, there are many shades of transparency. The transparency might be limited to bit-rate, format, protocol, or amplitude. If the network is transparent with respect to only some of the aforementioned characteristics, we speak of *selective transparency* and we only speak of *strict transparency* if the network is transparent in every aspect [7].

Traffic Grooming: One refers to the term traffic grooming when talking about the combination of data aggregation and switching.

Tributary Signal: In time-division multiplexing schemes, the term tributary refers to a lower bit-rate signal which is assigned to a specific time slot in a time-division multiplexer.

Switching Granularity: The granularity of the traffic switching g is defined as [2]:

$$g = \frac{\text{channel capacity}}{\text{baseband data rate}} = \frac{130 \text{ Gbit/s}}{43 \text{ Gbit/s}} = 3, \quad (1.1)$$

e.g. for a 130 Gbit/s TDM channel carrying several 43 Gbit/s streams, the granularity $g = 3$. Optical switching can be done at various levels of granularity and time scales that include: waveband switching, wavelength switching, sub-wavelength time slot level switching, burst switching, and packet switching. Wavelength level switching techniques allow circuit switched sharing of a wavelength.

Network Topology: The term topology refers to the shape of a network and how different nodes in a network are connected to each other. Common network topologies comprise the point-to-point, the bus, the tree, the ring, the star and the mesh network.

1.1.1 Optical Transport Networks

The concept of a global network with its different coverage areas, represented in the form of network planes operating on top of each other, is illustrated in Fig. 1.1a. These planes represent different levels of aggregated traffic and inter-node distances.

Wide-Area Network

The wide-area network (WAN, also called global backbone or long-haul network) is a network that spans over large geographical areas and carries aggregated global network traffic. In optical communications it represents any continental, terrestrial or undersea system.

Metropolitan-Area Network

The metropolitan-area network (MAN) is topologically ranked between the WAN and the access network plane. It serves the service providers and carriers to transport traffic within the own network and serves as an access network for the global WAN. Very often, the metro networks are further divided into (Fig. 1.1(b)):

Metro-Core: A ring network with a typical circumference of 100 – 200 km which aggregates higher bit-rate traffic (e.g. 2.5 Gbit/s, 10 Gbit/s Ethernet) from various metro-access rings.

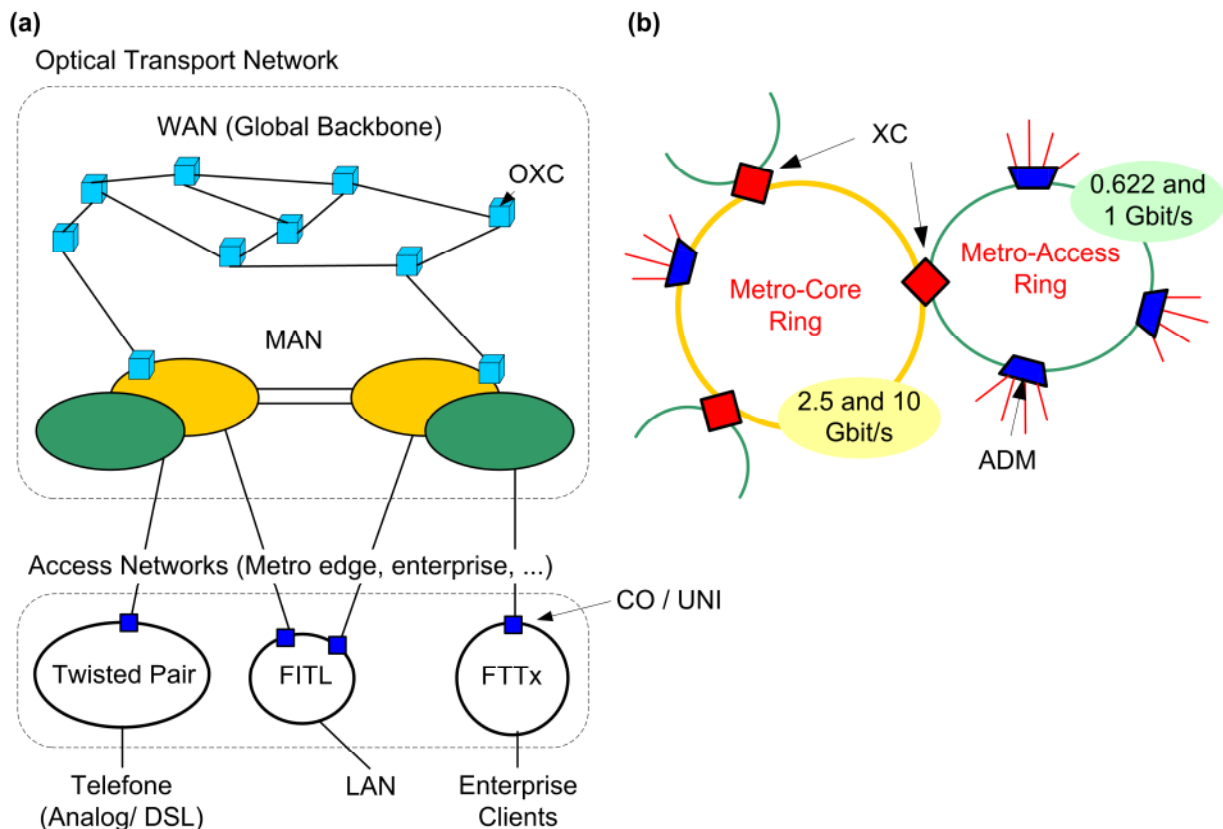


Fig. 1.1. (a) The optical transport network with its different coverage areas: WAN (wide-area network) or global backbone and MAN (metropolitan-area network). The MAN connects to access networks, that aggregate traffic from different sources. (b) Interconnected metro-core and metro-access rings with typical bit-rates. (O)XC – (optical) cross connect; ADM – add-drop multiplexer; CO – central office; UNI – user-network interface; FITL – fiber in the loop; DSL – digital subscriber line; FTTx – fiber to the x; LAN – local area network; IP – internet protocol.

Metro-Access: A ring network with a typical circumference of 30-60 km which aggregates low bit-rate traffic (e.g. 622 Mbit/s, 1 Gbit/s Ethernet) coming from the metro edge nodes (e.g. local area networks (LAN), enterprise clients, etc.).

Access Networks

The access network is that part of the public switched network that connects a central office (CO) with the user-to-network interface (UNI) of subscribers [8]. For instance, the access network includes the subscriber loops, the fiber in the loop (FITL) or fiber to the x (FTTx, where x stands for “home”, “business”, etc.) access networks. The traditional access network is the twisted-pair (TP) copper network, known as the subscriber loop. The subscriber loop might be an analog or a digital subscriber line (DSL).

1.1.2 Metropolitan Area Networks

Architectures

Ring architectures are widely used in MANs, see Fig. 1.1(b). This choice has been dictated by the ease of implementing protection mechanisms with this topology. As such, metro networks

usually consist of a group of metro-access rings interconnected by one or several interconnected metro-core rings that sometimes form a mesh-like topology.

Transmission Protocols

Most metro networks today consist of synchronous digital hierarchy (SDH) / synchronous optical network (SONET) interconnected rings [2]. SDH/SONET formats were developed when voice transmission was the dominant end-user application and are thus most efficient for multiplexing a large number of low rate signals. The SDH/SONET framework has evolved from the need to standardize multi-vendor interconnectivity at the fibre level. It also provides networking functionalities such as transport, multiplexing, add/drop, switching, regeneration and protection. It should be noted however, that Gigabit Ethernet (GbE) and 10 GbE has emerged as a new contender in the edge network space, because much of the traffic originates in Ethernet format [2]. Ethernet is promising better bandwidth utilization and network simplification by the elimination of Ethernet-to-SDH/SONET interfaces.

Network Elements

Optical cross-connect (OXC) switches: Used to interconnect the metro-access rings to the metro-core rings, and also to provide connections among different metro-core rings. Fig. 1.2 shows an OXC with input fibers. The WDM signal in each fiber is demultiplexed into separate channels. Afterwards the channels are guided into an electrical or optical switch fabric and directed to the assigned output port. XC switches must be divided into two categories: Conventional electrically switched digital cross-connects (DXCs) and optical cross-connects (OXC). DXCs perform optical-electrical conversion, regeneration, error correction, demultiplexing, switching, and again multiplexing and electrical-optical conversion before transmission through the metro-core ring. In addition, they perform time-slot interchange (TSI) on time-division multiplexed (TDM) signals. The optical-electrical-optical (OEO) conversion makes DXCs expensive and complex with large footprints and power consumption [9],[10]. When implemented as an all-optical device, OXS overcome the electronic bandwidth limitation offering data rate and protocol transparent wavelength switching.

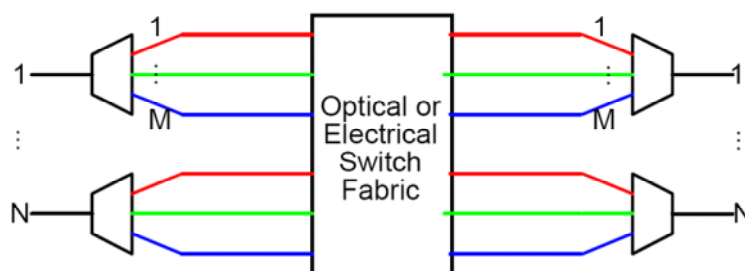


Fig. 1.2. Optical cross connect with N input fibers carrying M wavelength division multiplexed channels [11].

Add-drop multiplexer (ADM): Used to interconnect various customer sites to the metro-access rings at the UNIs. A multiplexer combines several lower-bandwidth data channels into a single wavelength channel and performs signal regeneration. At the same time, it can extract or drop other low-bandwidth signals, removing them from the stream and redirecting them to some other network path. An ADM also has the capability to add one or more lower-

bandwidth signals to an existing high-bandwidth data stream. For WDM rings, reconfigurable optical ADMs (ROADMs) are necessary where an optical switch fabric switches some of the incoming wavelength channels to the drop port while others are optically bypassed and new traffic is added via the add path (Fig. 1.3). In case of single wavelength rings, no optical switch fabric is needed and the incoming wavelength channel is terminated at each electronic ADM. However, an ROADM can be regarded as a special case of an OXC in view of traffic grooming capabilities. Unlike OXCs, an ROADM has only one input optical-line port and one output port. Hence, it manages moderate magnitudes of traffic compared to a small OXC, and therefore involves less grooming. Note that a bandwidth upgrade for a ring means that all ADMs and DXC interfaces have to be upgraded, which is a costly, time consuming and traffic-disruptive procedure.

Physical Layer / Medium

The fibre installed in the metro area is – in most cases – a standard single-mode fibre (SSMF) and is expected to be the medium of optical transmission in the metro well into the future because of its abundance, relative uniformity and standardization, and the fact that the installation of the fiber represents a large investment in every metro network.

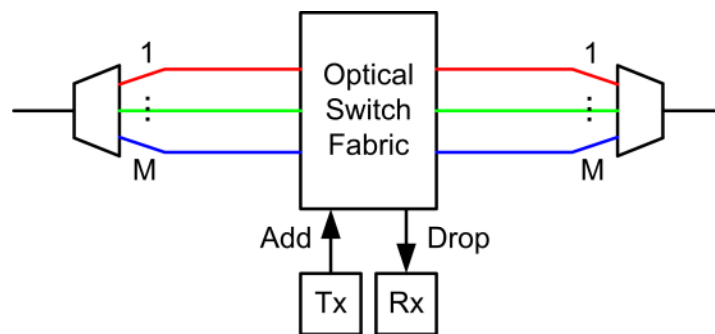


Fig. 1.3. Reconfigurable optical add-drop multiplexer with one input and one output fiber carrying M wavelength division multiplexed channels .

1.2 The Metro Gap - Future MAN Requirements

Internet data communication has shown persistent growth over the last years. Studies based on actual traffic data from providers collected during 2004 indicate a yearly increase of 115 % for aggregate average international internet traffic [12]. The applications behind this growth are now familiar to most computer users (email, file transfer, web browsing, peer-to-peer applications, online gaming, etc.). Besides the traditional voice and data transactions, a variety of new applications and associated services are emerging in today's telecommunication market. These include content-intensive applications like:

- Video distribution and video conferencing;
- Large image transfer;
- Virtual reality;
- Very high-speed internet access;
- Point-to-point protocol over Ethernet (1 Gbit/s, 10 Gbit/s and 100 Gbit/s in the future).

The possibility to offer to end users integrated TV, broadband internet access and telephone services (triple-play) is a strong driving force of the end-user telecommunication market. But high communication bandwidth at home is not limited to entertainment purposes; at the same time, high-bandwidth connections and advanced services are expected to drive the enterprise market where large amounts of data have to be transferred to assure database replication, business continuity, disaster recovery etc.

Recent forecasts for broadband penetration using the example of households and apartments that will be connected via fiber-to-the-building (FTTB) predict a dramatic increase in penetration of over 800 % in the next four years [13]. Countries like Sweden and Slovenia are predicted to have a household penetration of FTTH as high as 30 % by 2013. The improvement of access technologies on the end-user side will help delivering high-bandwidth to satisfy the demand growth brought by new applications. At the same time, in the regional/long-haul network, several technologies are mature enough to guarantee high connectivity and supply the high bandwidth requirements of lower network levels.

Clearly new metro solutions are required that offer superior price/performance alternatives to legacy SONET/SDH solutions. This is why the literature refers to the “metro gap” [1],[2], meaning that MANs will need an upgrade in order to cope with future traffic demands. Having identified the major applications and service drivers of next generation access and metro networks, some general conclusions can be drawn. This subchapter points out the requirements for future networks both in terms of capacity and features.

1.2.1 Transparent Traffic Grooming

In order to deal with the increase in data traffic, 40 Gbit/s is emerging as a viable and important bit rate in future metro networks. More specifically, the International Telecommunications Union (ITU) defined optical transport units (OTUs) with OTU3 having a line rate of approximately 43 Gbit/s. In addition, 100GbE is being standardized by the IEEE P802.3ba task force for links up to 40 km. It is expected that such traffic will be transported in the core network in serial form using OTU4 containers (currently under development in ITU-T study group 15), which will also be dimensioned for the transport of multiple OTU3's, resulting in a line rate close to 130 Gbit/s. Therefore, grooming from lower 43 Gbit/s bit rates to 130 Gbit/s will be required when moving from metro to core networks at the edge switching nodes.

In addition, the upgrade of the transmission rates brings along a diversity of protocols and transmission rates. Also considering that, within this network segment, different traffic types at lower data rates need to be aggregated at the edge between metro and core segments into high data rate channels and vice versa, it is important to offer transparent mechanisms for traffic grooming, i.e. sub-wavelength switching granularity. This will assist in simplifying the network architecture and eliminate unnecessary opto-electronic conversions having a direct impact on the cost and energy consumption of the overall system. Technically this is not a simple task, and has various implications related with the physical implementation and performance.

However, dynamic sub-wavelength grooming functionalities are currently unavailable in the optical layer, and will be required when jumping to 130 Gbit/s data rates. Network studies have shown that deploying alternatives to electronic grooming potentially will have the largest impact on reducing overall network cost [3].

1.2.2 Flexibility

A network scenario where high capacity is available to both residential users and companies demands flexibility in the network in order to establish new connections and support bandwidth-on-demand services. Furthermore, new dynamic services and applications will require fast provisioning as well as flexible and large aggregation capabilities.

1.2.3 Scalability

Another key requirement for metro networks is its scalability. Upwards scalability is achieved by (i) increasing the number of wavelengths per fiber link (leading to WDM) and (ii) increasing the bit-rate per wavelength (therefore, bit-rate transparency is required). At the same time, it is necessary to accommodate network upgrades on a pay-as-you-grow basis. This means that modular solutions have an advantage over inflexible high-capacity systems.

1.2.4 Energy Efficiency

The energy consumption of the internet is growing exponentially with a significant contribution from cross connects and buffers [14]. Heat dissipation problems and increasing current leakage will prevent the current network technologies from scaling up their capacity to the constantly increasing network traffic [15]. Completely novel network technologies should therefore be developed so as to allow the ever-increasing traffic. All-optical network elements have the potential of offering high energy efficiency.

1.2.5 Regeneration

Future MAN networks will evolve to more flexible and diverse architectures. Due to that, point to point impairment compensation methods will lose their relevance, and regeneration will be a more common tool in many network nodes. With regeneration, SMF has been proven to be a medium capable of transmitting ultra-high bit-rate WDM signals over hundreds of kilometers.

The introduction of optically transparent nodes in future MAN networks enlarges the distance that a signal has to pass between OEO regeneration points, and therefore creates a need to get some level of all-optical regeneration in the optical layer in the transparent nodes themselves.

1.2.6 Multi-wavelength Operation

As mentioned above, WDM metro rings offer advantages in flexibility and scalability. However, this is true only if all network elements involved can handle all wavelengths in parallel. Any node that requires demultiplexing of the wavelengths to single wavelengths and then multiplexing back after performing a function (like amplification, wavelength conversion or regeneration) is a node that deteriorates the cost effectiveness of this network architecture.

That is the reason why future improvements in metro nodes must keep the capability to perform the same function on multiple wavelengths without demultiplexing and using per wavelength functions in the network. The main functional unit lacking this capability these days is signal regeneration.

1.3 Summary

We have reviewed the basic characteristics of state-of-the-art optical transport networks. We then concentrated on metro networks in terms of their architecture, protocols, network elements, and the underlying physical layer. In addition, the concepts of optical cross-connects (OXC) and optical add-drop multiplexers (OADMs) as primary optical network elements have been discussed. In the second part of the chapter, the major applications and service drivers of next generation access and metro networks were reviewed. Based on the discussion on legacy metro networks it became clear that new metro solutions are required that offer superior price/ performance alternatives to legacy solutions. Requirements for these future MANs in terms of transparency, flexibility, scalability, energy efficiency, and multi-wavelength operation capability have been identified.

2 The Novel Optical Switch Node

In Chapter 1 we have reviewed the existing metro network implementations and the key requirements for future MANs. Recent advances in long haul transmission and switching technology have shifted the operational and bandwidth bottleneck from the core to the edge of the network [3],[16]. Replacing expensive OEO equipment with scalable all-optical solutions promises significant capital and operational cost savings due to the reduced power requirements and the service transparent bandwidth provisioning [17],[18],[19]. However, any new all-optical solution must be competitive in terms of both performance and cost compared to legacy SONET/SDH solutions. These should offer not only the traditional switching/routing and regeneration functionalities but also protocol transparent mechanisms for sub-wavelength level traffic grooming. Sub-wavelength traffic grooming means grooming of individual time slots of a WDM channel (instead of only grooming entire channels) and implies TDM.

In this work we propose a novel sub-wavelength grooming switch enabling protocol transparency between circuit or burst switched lower bit-rate metro-access networks and a higher bit rate metro-core ring network. Key functionalities of the node are traffic aggregation with time-slot interchange, OTDM-to-WDM conversion of the high speed channels into lower bit rate tributaries as well as all-optical multi-wavelength regeneration. A micro-electro-mechanical system (MEMS) switch in combination with all-optical wavelength conversion guarantees non-blocking space and wavelength switching functionality for any tributary, thus offering remote reconfigurability. It builds upon existing network architectures assuring backward compatibility, but enhances the state-of-the-art solutions in the switching nodes. We believe that our proposed solution has the potential to boost the progress in the metro networks and may match the technological leaps that have already been carried out at the backbone and access parts.

This chapter is structured as follows: In Section 2.1, we define the architecture for next-generation MANs, which is based on upgrading the current implementation. We then discuss three possible traffic structures that are considered in this work, which are: circuit switched traffic carried over continuous connections, circuit switched traffic carried over a burst mode transport layer, and burst mode traffic. In Section 2.2, the proposed switch node architecture is defined which integrates all the crucial functionalities that are currently provided by digital cross-connects (DXCs), i.e. switching, traffic aggregation/grooming and direct regeneration in the optical layer. In addition, we introduce the subsystems that provide the key functionalities. Detailed studies of the individual building blocks are presented in subsequent chapters (see Chapter 4 to Chapter 7). Finally, we summarize the key aspects and characteristics of the envisioned network solution.

Parts of this chapter have previously been published in [20], [21], [22].

2.1 Definition of the Network Architecture and Signal Structure

In this section we define the network architecture of the proposed future MAN meeting the key requirements identified in Chapter 1. We introduce the signal structures that are considered in this network architecture, which relate to both the format of the physical layer implementation and the routing protocol used.

2.1.1 Metro Network Architecture

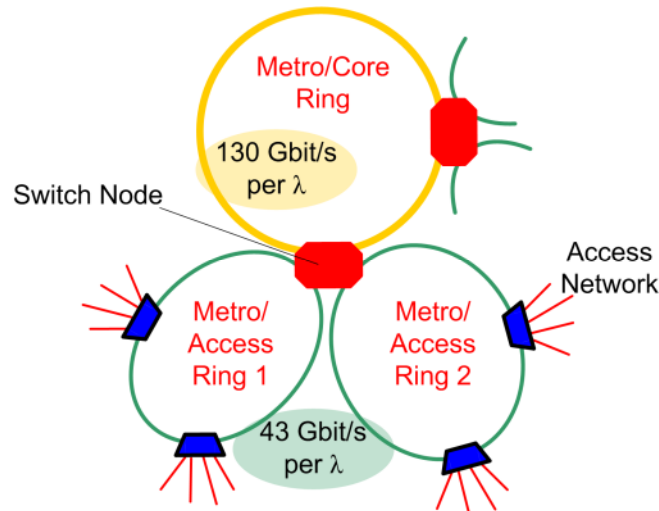


Fig. 2.1. Metro network scenario. Two metro/access rings are interconnected to a metro/core ring via the grooming switch. Each ring carries a multiple of WDM channels, either at 43 Gbit/s or 130 Gbit/s per wavelength.

In this work we design and implement a novel switch node architecture that offers a protocol transparent interconnection of different metro networks, i.e. between metro/access and metro/core at bit-rates of 43 Gbit/s and 130 Gbit/s, respectively, see Fig. 2.1. Note that the 43 Gbit/s WDM metro-access channels are aggregated into 130 Gbit/s OTDM metro-core channels. Thus, the optical switch node is operated here as an “edge node” that interconnects a WDM domain with an OTDM domain. This approach for next-generation MANs proposed in this thesis is based on upgrading the current architecture, providing a transparent interconnection node. This novel node can efficiently replace complicated and expensive electronic DXCs and adds further advantages to reconfigurable networks by providing functionalities currently unavailable in the optical layer such as protocol transparent traffic grooming/aggregation and optical regeneration. In such a way, it builds upon existing architectures assuring backward compatibility, but enhances the state-of-the-art solutions in the switching nodes. As such, the proposed network architecture answers to the requirements for the features and capabilities of future MANs.

Note that using different concrete implementations, the switch node can interconnect a variable number of metro-access rings to the metro-core ring. It can also be used to interconnect two or more core rings or provide connectivity to the backbone network.

2.1.2 Signal Structure and Conditions

This work considers circuit-switched architectures from the point of view of physical routes through the network. Traditional SDH networks would utilize buffer stores within add-drop multiplexers (ADM) to accommodate for variations in propagation delay along various network routes, however, such buffer stores are not practical for an all-optical switch. It is thus necessary at points of traffic aggregation to account for jitter, wander and clock frequency drifts [6] without recourse to buffers. Within this work, such aggregation occurs at the edges of the network, e.g., at the intersection of metro-access and metro-core rings (see Fig. 2.1), with typical ring lengths of up to 200 km.

Three possible traffic structures have been considered in this work which relate to both the format of the physical layer implementation and the routing protocol used, which are: circuit switched traffic carried over continuous connections, circuit switched traffic carried over a burst mode transport layer, and burst mode traffic. The choice of the signal structure not only impacts the required switching speeds of the WDM routers and the synchronization dynamics of the WDM-to-OTDM aggregation, but also changes the design of transmitter, receiver and amplifier circuits. In the following, the three structures will be discussed successively.

Circuit Switched Traffic carried over Continuous Connections

For circuit switched traffic carried over continuous connections it is envisioned that the WDM metro-access ring traffic presented to the switch node would be aggregated to optical time-division multiplexed (OTDM) data signals. In a laboratory environment, where all signals typically originate from a single high quality frequency reference, this may be achieved for sufficiently long periods for performing practical measurements. And indeed, continuous traffic is used in the switch node lab demonstration, see Chapter 8. Even for small networks it seems to be most efficient to simply resend frames, which are damaged due to synchronization of the WDM input channels.

However, in larger networks, it is necessary to account for long term variations (diurnal and seasonal) in the optical path length, and for aspects arising from the operation of transmitter clocks in a free running holdover mode¹ without synchronization information. Both of these effects result in small, but finite frequency differences in the WDM signals arriving at the optical router. In order to match the output frequencies, the frequency differences either lead to dropped bits or require bit stuffing (insertion of no-information bits into the input signal streams for synchronization). Such operations require complex processing of the signal in the optical domain, which lies beyond the scope of this work. Furthermore, for the selected ring network architecture, synchronization over diverse paths is essential.

¹ In synchronous networking, the network elements used to transport the data are tightly synchronized across the entire network, using local atomic clocks. In case the local clock fails, a network element goes into holdover mode. In holdover mode, stored data is used (acquired during normal operation) to derive clock information for synchronization. Holdover terminates when the higher quality timing becomes available again.

A standard solution to this problem is the use of distributed phase locked loops. Unfortunately, the distributed phase locked loop is severely jitter limited for transmission distances of 200 km and may not simultaneously accommodate delay variations over diverse paths [23].

Burst Mode Transport Layer

In order to accommodate the potential clock frequency differences of channels arriving at the routing node, an alternative approach is to develop a slotted network, where guard bands are employed (Fig. 2.2). Conceptually, the required bit stuffing or bit dropping occurs within the guard bands, and this redundant information is simply not transmitted. In practice, the guard-bands are used to reset (switch between) optical delays in order to align the bits. Among other options, these guard bands may be used to either reset continuous delay lines with finite tuning range to the centre of their tuning range, or to allow for the operation of an asynchronous retiming unit [24], with the latter being used in this thesis.

The slotted transport layer may be used to establish either circuit switched connections or burst mode connections. For circuit switched connections a particular configuration of WDM switches establishes a temporary route across the network between two nodes, and the connection is operated with slotted traffic to account for path length and frequency variations. On the other hand, for a burst mode connection, routing decisions and retiming decisions would occur simultaneously, on a burst-by-burst basis.

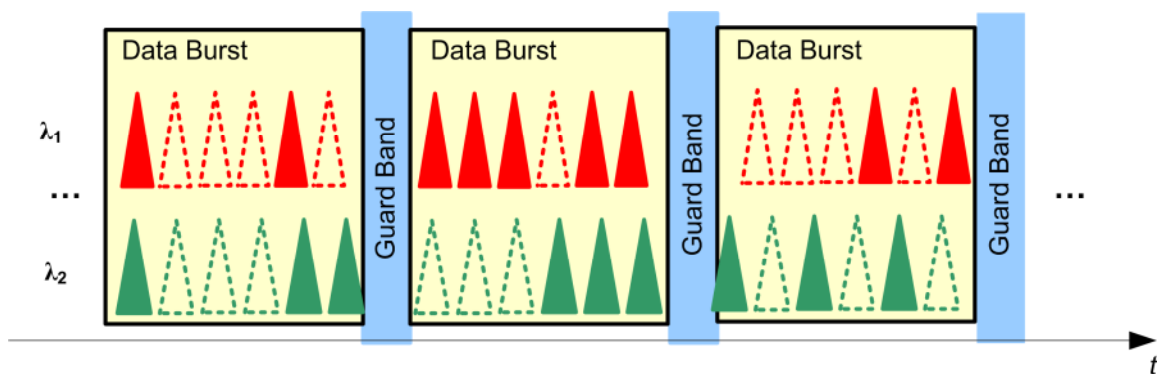


Fig. 2.2. Conceptual diagram of a slotted network, with two wavelength channels (λ_1 , λ_2) operating at slightly different clock frequencies. For traffic aggregation, the guard bands are used to switch between different optical delays in order to align the bits.

2.2 Definition of the Switch Node Architecture

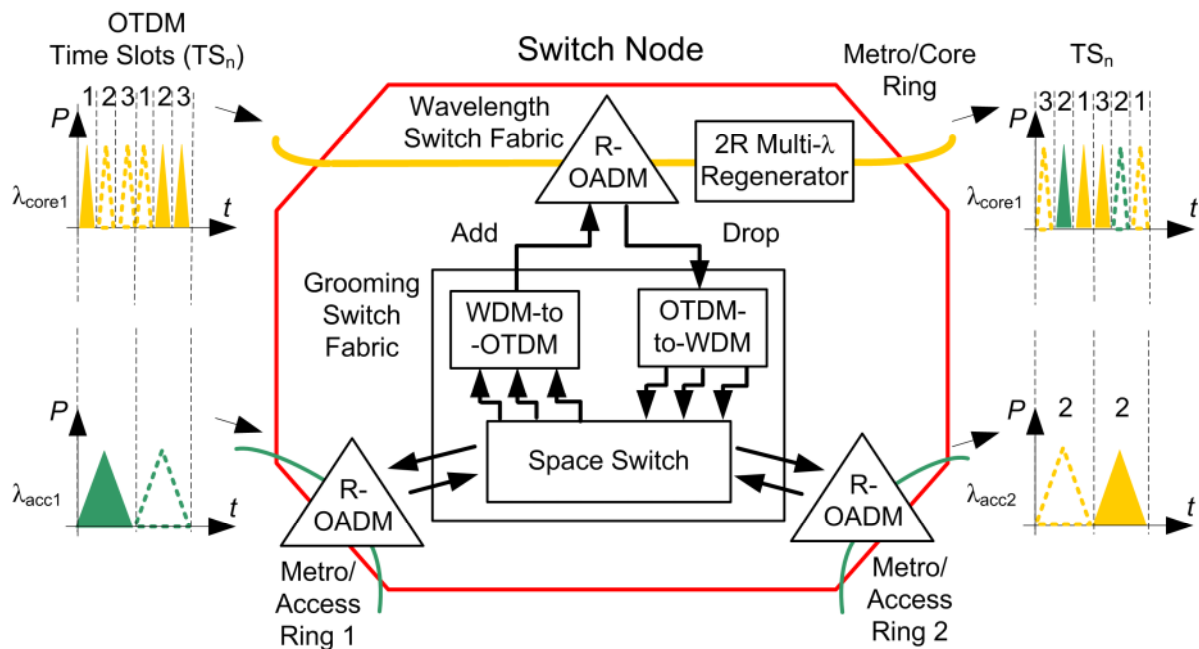


Fig. 2.3. Switch node block diagram. Traffic from the metro-access rings is switched by the space switch either to the other access rings, or via the add path to the metro-core ring. Conversely, an OTDM channel from the metro-core ring can be dropped, and any of the three OTDM tributaries may be mapped to any of the metro-access rings or back to the core ring. The signals in this plot show one possible switching scenario: Three OTDM tributaries at λ_{core1} are dropped to the OTDM-to-WDM converter. Two of its outputs (carrying time-slots TS_1 and TS_3) are switched to the WDM-to-OTDM converter, slot-interchanged and looped back to the core ring. Channel λ_{acc1} from metro ring 1 is added and mapped to time-slot TS_2 . In addition, the dropped time-slot TS_3 is mapped to λ_{acc2} on metro ring 2.

In this section we define the switch node architecture with its subsystems. In addition, the key functionalities offered by the novel architecture are reviewed.

A schematic illustration of the switch node is depicted in Fig. 2.3. Irrespective of any specific network scenario, the switch node can be classified as a traffic grooming optical cross-connect (OXC) [25], which consists of three wavelength switch fabrics in the form of reconfigurable optical add-drop multiplexers (ROADMs) and a grooming fabric in the center of the switch. The ROADMs allow for adding and dropping of traffic from the access or the core network to the grooming fabric. The grooming fabric performs TDM and WDM multiplexing, demultiplexing, and switching between low-speed (43 Gbit/s) and high-speed (130 Gbit/s) connections.

In detail, the grooming switch works as follows (Fig. 2.3): Traffic from any of the metro rings is switched by means of an optical space switch (micro-electro-mechanical system (MEMS)) to any of the metro rings, or via the add path to the core ring. When the traffic is switched to the core add path, a WDM-to-OTDM unit retimes the incoming asynchronous data signals

with reference to a local clock. The retimed signals are converted to short high-repetition rate pulses at a new wavelength in conformity to the OTDM channel requirements. The WDM-to-OTDM conversion operation is based on the asynchronous digital optical regenerator (ADORE). The assignments and order of the time-slots of the WDM tributaries within the output OTDM can be chosen freely by the space switch. Conversely, a core OTDM channel may be dropped via the ROADM to the OTDM-to-WDM converter. Any of the three OTDM tributaries can then be mapped to any of the access rings or back to the core ring. Therefore, the time-slots can be interchanged. To guarantee the quality of the 130 Gbit/s traffic in the core ring all-optical multi-wavelength regenerators are added.

Subsystem Functionality

In detail, the key functionalities of the switch node can be summarized as:

- **Wavelength selective optical switching**, which is achieved through a reconfigurable optical add-drop multiplexer (ROADM).
- **Traffic grooming**, which is achieved by utilizing WDM-to-OTDM conversions (transmultiplexing) and vice versa.
- **Time-slot interchange (TSI)**, where traffic in the core ring can be switched from one wavelength/time-slot to any other wavelength/time-slot at the node. This includes the possibility to interchange the time-slots of one wavelength by dropping and looping-back that wavelength through the add path. TSI is achieved by utilizing WDM-to-OTDM conversions and vice versa in combination with the space switch.
- **Optical multi-wavelength 2R regeneration** of the signals that leave the node via the core ring.

The wavelength switching functionality that is enabled by the space switch/ROADMs allows dynamic wavelength selection and thus switching of the individual channels to any fiber ring. This dynamic allocation of the optical bandwidth and the on-demand establishment of connections will enable the supply of broadband services to end-users.

The traffic aggregation and grooming that is enabled by the WDM-to-OTDM and OTDM-to-WDM converters also plays a critical role in reducing the network operational expenditure (OPEX). Future networks must support a variety of traffic protocols. Considering that this inhomogeneous traffic at lower data rates needs to be aggregated at the edge between metro and core segments into high data rate channels, it is important that the offered traffic aggregation and grooming mechanisms are also transparent to traffic protocols. This will further assist in simplifying the network architecture and eliminating a large number of costly optoelectronic conversions.

The quality of the 130 Gbit/s traffic in the core ring is guaranteed by an all-optical multi-wavelength regenerator. The multi-wavelength 2R regeneration (see Fig. 2.3) is also very important in terms of cost-efficiency. It provides simultaneous regeneration of a WDM signal incorporating three individual wavelength channels. Therefore, it will eliminate the requirement of demultiplexing WDM signals into individual wavelength channels, and the use of a

single regenerative device per wavelength followed by subsequent multiplexing. The multi-wavelength processing capability of our regenerator mirrors that of optical amplification, with the added benefit of restoration of the signal quality.

Detailed descriptions and experimental investigations of the individual subsystems are presented in the following chapters.

2.3 Summary

We proposed a novel optical switch node that integrates all the crucial functionalities for future MANs, i.e. switching, traffic aggregation-grooming and direct regeneration in the optical layer. The network architecture for these next-generation MANs was defined and three possible traffic structures were discussed that are considered in this work, which are: circuit switched traffic carried over continuous connections, circuit switched traffic carried over a burst mode transport layer, and burst mode traffic. In addition, we introduced the subsystems that provide the key functionalities. Our approach offers broadband access for every user and interoperability with existing infrastructures. Therefore, it can be a future-proof alternative to legacy SONET/SDH networks accommodating the high processing and capacity requirements of the emerging services and applications in a cost effective way. We believe that our proposed solution has the potential to boost the progress in the metro networks and may match the technological progress that has already taken place in the backbone and access parts.

3 Test Setups and Measurement Techniques

The operation of optical high-speed transmission systems is a highly complex task. For this reason, this chapter gives detailed information on the basic setups and techniques that were used in this work. All system tests are done without fiber transmission (so-called back-to-back (B-to-B) configuration).

Two modulation formats have been used as test signals for characterization of the different subsystems proposed in this thesis: Amplitude shift keying (ASK, also called on-off-keying (OOK)) and differential phase shift keying (DPSK), both at 43 Gbit/s. In addition, testing of the proposed network architecture (see Chapter 2) requires OOK signals at 130 Gbit/s. This signal is produced by optical time division multiplexing of three 43 Gbit/s OOK tributaries.

This chapter is organized as follows. First, Section 3.1 briefly reviews the signal degradations in optical high-speed systems. Section 3.2 discusses the fundamentals of the Mach-Zehnder modulator used for all modulation purposes in this work. Then, the OOK transmitter and receiver setups and characteristics for 43 Gbit/s and 130 Gbit/s are discussed in detail in Section 3.3 and Section 3.4, respectively. In Section 3.5, the DPSK transmitter and the balanced receiver are presented. The chapter closes with Section 3.6, which introduces the methods and figures of merit for performance characterization used in this work.

3.1 Signal Degradation in Optical High-Speed Systems

Optical signals suffer during transmission from different effects that degrade the signal quality. For high speed transmission, the following effects play a role:

Attenuation and Noise – Glass fiber exhibits its smallest attenuation of $\alpha \approx 0.2$ dB / km at wavelengths of around $\lambda = 1.55$ μm (also called centre-band or C-band), which is the wavelength range of choice in this work. For long transmission distances or after traversing network elements and subsystems that additionally attenuate the signal, reamplification of the signal is necessary. This is done by using Erbium-doped fiber amplifiers (EDFAs). However, the signal-to-noise ratio (SNR) degrades with each amplification step. Maintaining a sufficiently good SNR is relevant especially for high data rates, since the SNR requirement increases with data rate.

Group Velocity Dispersion – The term dispersion, or, more precisely, group velocity dispersion (also called intramodal dispersion), is a consequence of the frequency dependence of the effective group refractive index (and hence the group velocity) of a signal propagating within the optical fiber. The frequency-dependence of the effective refractive index can be

approximated by a Taylor series. We define a wavelength-dependent chromatic dispersion factor $C_\lambda(\lambda) = C + D\Delta\lambda$ which is approximated by a straight line near the reference wavelength λ_1 ,

$$\frac{\Delta t_g}{L} = C_\lambda(\lambda)\Delta\lambda = (C + D\Delta\lambda)\Delta\lambda = C\Delta\lambda + D(\Delta\lambda)^2. \quad (3.1)$$

The dispersion coefficients $C \equiv C(\lambda_1)$ (in ps / (km nm)), and $D \equiv D(\lambda_1)$ (in ps / (km nm²)) are constants of the Taylor expansion at a certain reference wavelength $\lambda = \lambda_1$. For short pulses with broad spectra, also the second order dispersion coefficient D is relevant. Dispersion leads to pulse broadening during propagation along the fiber. The shorter the pulses are at the beginning, the stronger is the effect. Therefore, at high data rates dispersion compensation is required. As dispersion is a linear effect, it is reversible: The initial pulse shape can be recovered if the pulses traverse a fiber with dispersion having the opposite sign. Dispersion can even be used for mitigation of non-linear effects within the fiber. In Chapter 7 a signal regeneration technique using a specially designed dispersion map is presented.

Polarization Dependence – In real optical systems, waveguides of the optical fiber and components are not perfectly cylinder symmetric. The two most important effects are polarization dependent loss (PDL) and polarization mode dispersion (PMD). In this work, PDL plays a role for discrete components, which need a fixed input polarization due to their PDL. PMD is created by waveguide birefringence. Since the state of polarization at the input of the waveguide does generally not correspond to an eigenstate of the waveguide, the state of polarization (e.g. linear polarization) changes during propagation. E.g., a linear polarization launched into a birefringent fiber in general transforms into an elliptical polarization at the output. PMD is a consequence of the fact that different polarization states experience different group delays. Since PMD is only significant for long transmission distances it does not play a role in this work.

Nonlinearities – Nonlinear effects appear in fibers for high optical intensities. For short pulses, this is crucial since high peak pulse powers are reached even for moderate average powers. However, in combination with highly nonlinear fibers (HNLF), nonlinear effects like self-phase modulation (SPM) and cross-phase modulation (XPM) are also used for all-optical signal processing, e.g. wavelength conversion and signal regeneration. In this work, two different switch node subsystems based on non-linear effects are presented: First, the OTDM-to-WDM converter (based on either XPM or SPM), see Chapter 5, and second, the signal regenerator (based on SPM), see Chapter 7. In Appendix A 2 the basic characteristics of SPM and XPM are introduced.

3.2 Mach-Zehnder Modulators

For the majority of the experiments in this work, amplitude modulation is used. This is due to two reasons: First, legacy metro and core networks almost exclusively employ intensity modulated signals and compatibility is an important for deploying new network concepts. Second, commercial amplitude modulation transmitters and receivers are relatively low priced as compared to other, more complicated modulation format transmitters. Nevertheless, using phase modulation and multilevel formats can be advantageous for various network applications and has received increased attention recently. Therefore, this work also presents a wavelength converter and signal regenerator for phase modulated signals (see Chapter 7).

A phase change can be impressed on an optical carrier wavelength by the electro-optic effect (Pockels-effect). The material mostly used for this purpose is Lithium Niobate (LiNbO_3). For amplitude modulation, this phase modulation is converted into an amplitude modulation using Mach-Zehnder interferometers. The so-called Mach-Zehnder modulators (MZM) are exclusively used for amplitude and phase modulation in this work.

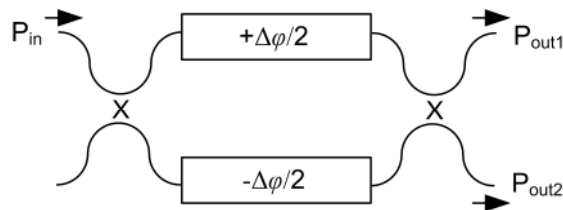


Fig. 3.1. Principle setup of a push-pull Mach-Zehnder modulator.

The setup of a push-pull-MZM is depicted in Fig. 3.1: In each arm of the modulator, half of the desired phase shift $\Delta\varphi$ is induced. Using an anti-symmetrical electrical drive signal avoids an undesired chirp (phase modulation) of the output signal, and the optical carrier in the two arms experiences a phase shift of $+\frac{\Delta\varphi}{2}$ and $-\frac{\Delta\varphi}{2}$.

In addition to the time-variant drive signal, a DC voltage called modulator bias is applied and leads to a static phase shift. By this bias the interferometer is set to the desired operating point. The total phase shift is given by

$$\Delta\varphi(t) \sim V_{MZM}(t) = V_{bias} + V_{NRZ}(t), \quad (3.2)$$

where V_{MZM} denotes the total drive voltage of the MZM comprising the static part V_{bias} and the dynamic part V_{NRZ} (electrical NRZ bit sequence).

The power at both interferometer outputs are given by [7]

$$P_{out1}(\Delta\varphi) = P_{in} \cdot \sin^2 \frac{\Delta\varphi}{2} \quad (3.3)$$

$$P_{out2}(\Delta\varphi) = P_{in} \cdot \cos^2 \frac{\Delta\varphi}{2} \quad (3.4)$$

$$\Rightarrow P_{out1}(\Delta\varphi) + P_{out2}(\Delta\varphi) = P_{in} \cdot \underbrace{\left(\sin^2 \frac{\Delta\varphi}{2} + \cos^2 \frac{\Delta\varphi}{2} \right)}_{=1} \quad (3.5)$$

These equations not only apply for push-pull modulators, but in general for all interferometric arrangements used in this work. Energy conservation of the lossless interferometer according to Eq. (3.5) leads to the conclusion that the outputs of an interferometer are complementary. For all states where $\Delta\varphi = n \cdot \pi$ ($n \in \mathbb{Z}$), the power is either completely at the upper output or at the lower output. This is exploited for balanced detection after the interferometer and for demodulating a DPSK signal.

The transfer function T_{MZM} for both outputs of the MZM is then given by

$$T_{MZM}(\Delta\varphi) = T(V_{MZM}) = \frac{P_{out1,2}}{P_{in}} = \cos^2 \frac{\Delta\varphi}{2} \quad (3.6)$$

and is depicted in Fig. 3.2. The voltage needed for a phase swing of $\Delta\varphi = \pi$ is called V_π .

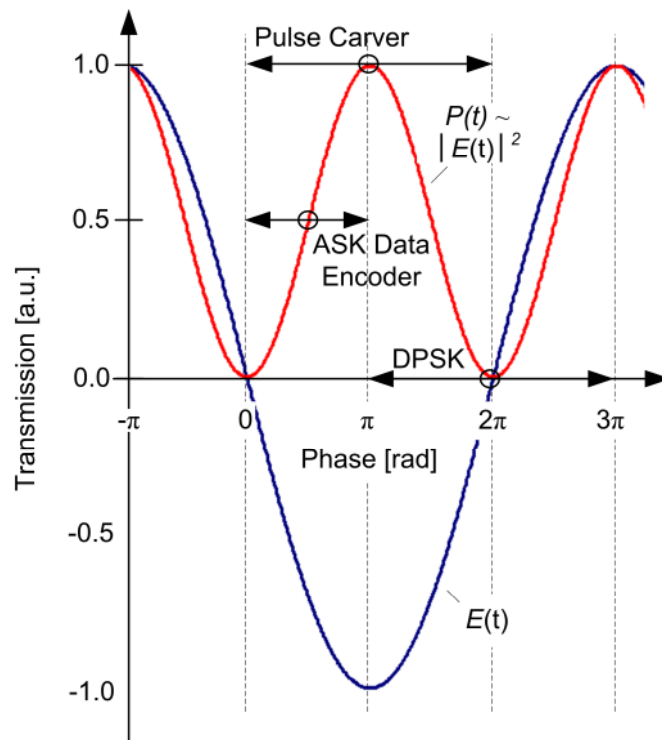


Fig. 3.2. Amplitude $E(t)$ and power transfer function $P(t)$ of a Mach-Zehnder modulator with bias points and drive voltage amplitudes for pulse carving (33% duty cycle), amplitude shift keying (AKS) and DPSK, respectively.

Amplitude Shift Keying

For amplitude shift keying (ASK), the bias is set to the ASK operating point as depicted in Fig. 3.2. The electrical drive signal has to have an amplitude of $V_\pi/2$ for each arm in push-pull operation for switching between ON and OFF state. The exact operating point is adjusted by optimizing the BER and the eye diagram. Achievable ON/OFF extinction ratios are around 15 dB. In case of the return-to-zero (RZ) format, a second MZM is used for pulse carving. The standard

pulse duty cycle of 33 % is achieved when applying a sinusoidal drive voltage with half the clock frequency ($f_{\text{clk}}/2 = 21.5$ GHz) and a peak-to-peak voltage of V_π for each arm. The operating point for the pulse carver has to be in the maximum of the transfer function.

Differential Phase Shift Keying

Modulators based on MZI are also used for phase modulation in this work [7]. For DPSK modulation, the bias and drive amplitude has to be adapted as shown in Fig. 3.2. The bias is now chosen to be in the minimum of the transfer function. This is easy to adjust: With the drive signal being switched off, the bias is set to the minimum output power. Note that the electrical drive signal V_{NRZ} now has to be set to V_π for each arm.

Test Signals

Binary data are represented by non-return-to-zero (NRZ) sequences. In the lab, so-called pseudo random bit sequences (PRBSs) are used as test signals instead of real traffic. They have a length of $2^N - 1$, with $N = 7, 11, 15, 23$ or 31. The shortest sequence of $2^7 - 1$ is depicted in Fig. 3.3. The longest sequence of equal bits contained in a PRBS is equal to the exponent N . Depending on the PRBS sequence, some devices under test can show parasitic effects (pattern effects). In some of the experiments of this work, the non-existence of pattern effects have been checked by using a $2^{31} - 1$ bit long PRBS. Other experiments have been done using short sequences for two reasons: First, the optical time division multiplexer is configured for decorrelation of 127 bit sequences. Second, an oscilloscope for signal monitoring can only be used with short bit sequences, otherwise the pattern trigger frequency will be too low. The actual PRBS lengths used for the different experiments in this work are given in the respective chapters.

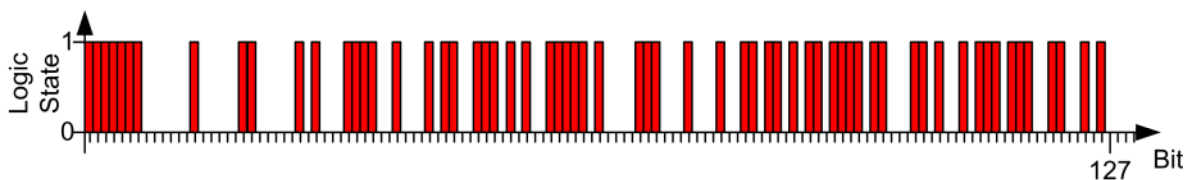


Fig. 3.3. 127 bit long pseudo random bit sequence ($2^7 - 1$ bits).

3.3 RZ-OOK 43 Gbit/s Transmitter and Receiver

3.3.1 Transmitter

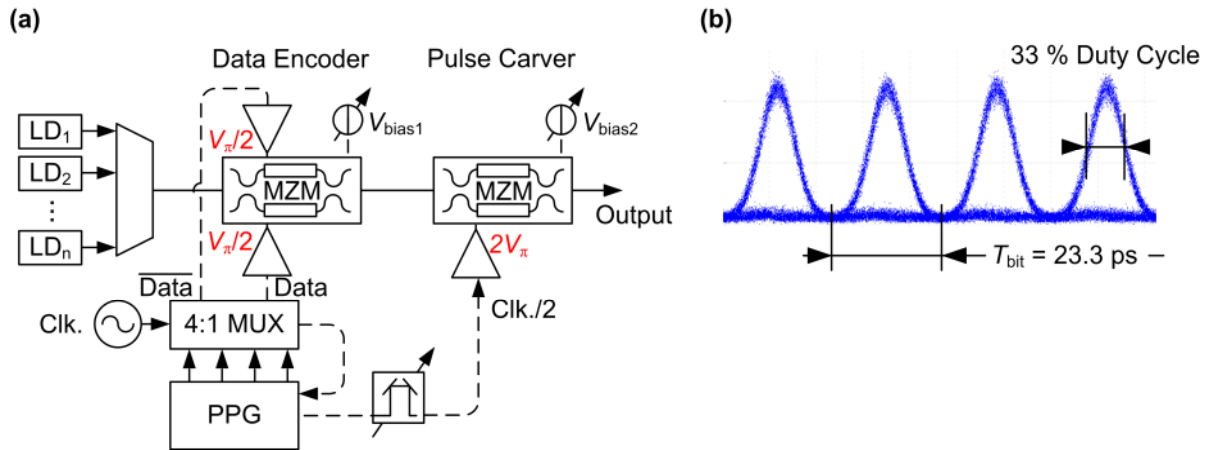


Fig. 3.4. (a) Experimental setup of 43 Gbit/s RZ-OOK transmitter. WDM laser diodes (LD_1, LD_2, \dots, LD_n) are amplitude modulated by two MZMs. The data encoder is a dual-drive push-pull MZM driven with an amplitude of $V_{\pi}/2$ in each arm. The pulse pattern generator (PPG) generates 4×10.8 Gbit/s PRBS signals that are multiplexed (MUX) to 43.2 Gbit/s. The pulse carver is a single-drive push-pull MZM driven by half the clock frequency with a peak-to-peak voltage of V_{π} for each arm. An electrical phase shifter is used for adjustment of the pulse phase with respect to the data signal. (b) Typical output eye diagram of the transmitter with a pulse duty cycle of 33 %.

The transmitter setup is depicted in Fig. 3.4(a). Distributed feed back (DFB) laser diodes (LD_1, LD_2, \dots, LD_n) generate C-band WDM carriers which are modulated by two MZMs. Both modulators are push-pull Mach-Zehnder interferometers. The dual-drive data encoder is driven with an amplitude of $V_{\pi}/2$ in each arm and has a 3-dB opto-electronic bandwidth $BW = 36.0$ GHz. The pulse pattern generator (PPG) generates 4×10.8 Gbit/s PRBS signals that are electronically multiplexed in the time-domain (MUX) to 43 Gbit/s. The pulse carver is a single-drive push-pull MZM (3-dB $BW = 36.4$ dB) driven by half the clock frequency with a peak-to-peak voltage of $2V_{\pi}$. An electrical phase shifter is used for adjustment of the pulse phase with respect to the data signal. Fig. 3.4(b) shows a typical, very clean output eye diagram of the transmitter with a pulse duty cycle of 33 % (telecom standard). This configuration has the advantage of producing a chirp-free signal since only modulates the amplitude and not the phase of the input field. This setup is used for system characterization in Chapter 4 and Chapter 7.

3.3.2 Receiver with Optical Pre-amplifier

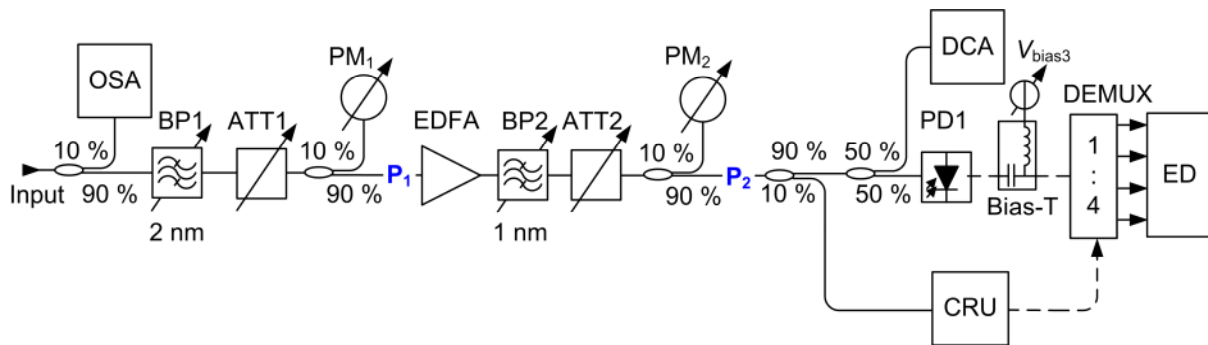


Fig. 3.5. Setup of the receiver with optical pre-amplifier. The input signal is filtered, optically amplified and filtered again. Part of the signal is split off for use in the clock recovery unit (CRU) which feeds the recovered clock to the electronic DEMUX. A broadband photo detector (PD1) detects the signal which is fed into the DEMUX. The decision threshold for data recovery can be varied via a bias-T. The error detector (ED) measures the BER. OSA – optical spectrum analyzer; BP1, BP2 – band pass filter; ATT1, ATT2 – variable attenuators; PM1, PM2 – power monitors; EDFA – Erbium doped fiber amplifier; DCA – digital communication analyzer. P_1 and P_2 denote optical power levels at different points in the setup.

The receiver setup with optical pre-amplifier is depicted in Fig. 3.5. The input signal spectrum is monitored by an optical spectrum analyzer. Then, the WDM channel of interest is selected by a tunable band pass filter with a 3-dB bandwidth (BW) of 2 nm. An Erbium-doped fiber amplifier (EDFA) amplifies the signal, which then is again filtered (1 nm 3-dB BW) in order to suppress the outband amplified spontaneous emission (ASE) noise of the EDFA. The amplifier used has a flat gain spectrum from 1529 nm to 1562 nm, a very low noise figure [26] $F < 4$ dB ($P_{in} = -25$ dBm), a small signal gain $SSG > 40$ dB ($P_{in} = -40$ dBm), and an output saturation power $P_{sat} = 18$ dBm. The signal is detected with a broadband PIN photodiode with an RF bandwidth of 45 GHz. The data signal is recovered and demultiplexed by a 1:4 DEMUX. For Q-factor measurements (for details see Appendix A 1) the electrical signal can be varied against the decision threshold via a broadband bias-T (65 GHz) at the DEMUX input. The bit error ratio (BER) is measured by the error detector (ED). For BER vs. input power measurements (for details see A 1), the receiver input power P_1 is adjusted by an attenuator (ATT1) and monitored by a calibrated power monitor (PM1). At the same time, the input power of PD1 has to be kept to the optimum value. This is done by ATT2 and PM2. Part of the optical signal is used for clock recovery (CRU), which clocks the DEMUX. The excellent measured receiver sensitivity (defined as the minimum input power P_{sens} required for a $BER = 10^{-9}$) of this setup in combination with the 43 Gbit/s 33% RZ-OOK transmitter described above is $P_{sens} = -32.5$ dBm.

3.4 130 Gbit/s RZ-OOK OTDM Transmitter and Receiver

3.4.1 Time Multiplex

A real system for time-division multiplexing three 43 Gbit/s channels into a 130 Gbit/s would consist of three transmitters. As identical wavelengths are needed for all three lower bit-rate tributaries, the signal would be derived from a 43 GHz short pulse source which will be modulated separately by three modulators.

In the lab the setup is simplified such that only one transmitter is used. Then, a time multiplexer constructs the 130 Gbit/s signal out of three identical 43 Gbit/s tributaries. In addition to the temporal interleaving, for this lab implementation, decorrelation of the data is desirable. Such a decorrelation is not needed for three independent transmitters and real data, having the advantage that long delay lines (leading to phase instability, see below) can be avoided.

3.4.2 Short Pulse Sources

The pulse source plays a key role in OTDM transmission. A suitable short pulse source needs to fulfill the following requirements:

- The repetition rate should be $f_{\text{clk}} = 43$ GHz to avoid additional OTDM stages adding instability to the setup.
- Pulse width should be close to 1/9 of the 43 Gbit/s period $T_{\text{bit}} = 23.3$ ps. This leads to a duty cycle of 33 % at 130 Gbit/s with a FWHM pulse width of $\tau = 2.6$ ps. Since this requirement needs to be fulfilled at the receiver (after some dispersion during transmission), the transmitter pulse width should rather be $\tau < 2.6$ ps.
- For avoiding coherent superposition of neighboring pulses a good extinction ratio is required such that the pulse power has strongly dropped at the position of the neighboring pulse.
- Low timing jitter for good interplay with the optical DEMUX switch at the receiver.

For the experiments presented in this work, mode-locked lasers (MLL) with ring cavities were used. Active mode coupling is needed to operate the laser at 43 GHz repetition rate, which is stabilized by a phase-locked loop. Two MML from the same manufacturer and same model are used in the experiments. The repetition rate is $f_{\text{clk}} = 43$ GHz, the output power is $P_{\text{out}} = 20$ dBm, the wavelength range extends from 1535 nm to 1565 nm, the timing jitter is $\sigma_{\text{RMS}} < 70$ fs, and the spectral modulation depth is 35 ... 40 dB. The pulse width is adjustable and is set to $\tau < 2.6$ ps FWHM with approximate sech² shape. The advantage of these short pulse sources is low jitter and high output power. A disadvantage is the weak long-term stability required for system measurements.

3.4.3 Lab Implementation of the Time Division Multiplexer

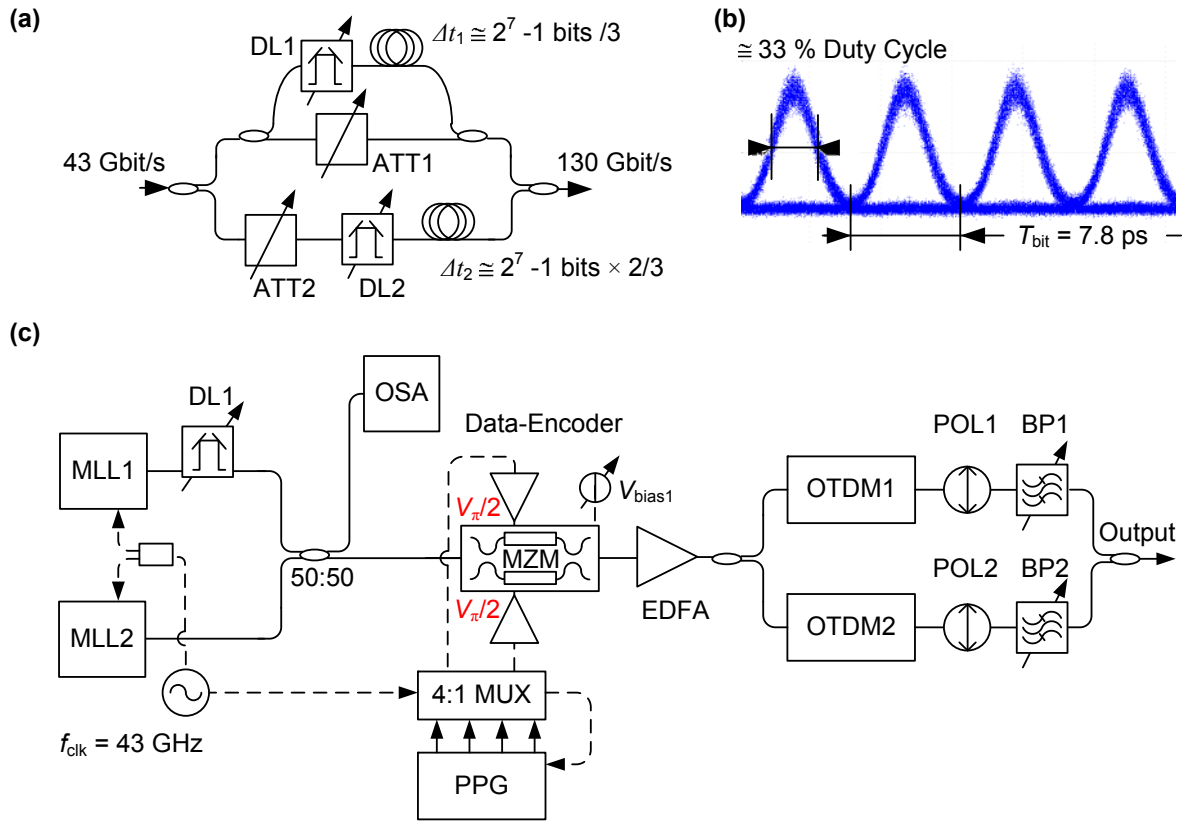


Fig. 3.6. (a) Setup of a 43 Gbit/s to 130 Gbit/s OTDM multiplexer consisting of a child MZI integrated in one arm of a parent MZI. Each interferometer features a tunable free-space delay line (DL1, DL2) in one of its arms for precise length adjustment, and pieces of single mode fiber for data decorrelation. Attenuators ATT1 and ATT2 are used for power adjustment. (b) Optical OTDM eye diagram measured with an ultra-fast optical sampling scope. (c) Complete setup of the 130 Gbit/s transmitter. Ultra-short MLL (MLL1 and MLL2) pulses are data encoded by a dual-drive push-pull MZM driven with an amplitude of $V_{\pi}/2$ in each arm. The pulse pattern generator (PPG) generates 4×10.8 Gbit/s PRBS signals that are multiplexed in the time-domain (MUX) to 43 Gbit/s. The signals at both wavelengths are fed into OTDM multiplexer, at the outputs of which band-pass filters (BP1, BP2; $BW = 5$ nm) are used to reject one of the wavelengths. Polarizers (POL1, POL2) guarantee single polarization output signals.

An OTDM multiplexer for 3×43 Gbit/s to 130 Gbit/s is depicted in

Fig. 3.6(a). It consists of a child MZI integrated in one arm of a parent MZI. Each interferometer features a tuneable free-space delay line in one of its arms for precise length adjustment. Delay for data decorrelation is realized by using long pieces of standard single mode fiber (SMF). However, this is only possible for the shortest PRBS sequence of $2^7 - 1$ bits for stability reasons. Maximum decorrelation is achieved for $\Delta t_1 = \text{PRBS}/3$ and $\Delta t_2 = 2/3 \times \text{PRBS}$, corresponding to 19.7 cm and 39.4 cm of standard SMF, respectively, with the group velocity:

$$v_{gr} = \frac{c_0}{n_g} \approx 200 \frac{\mu\text{m}}{\text{ps}} \quad (3.7)$$

(c_0 - vacuum speed of light and $n_g = 1.5$ group refractive index of glass). Since for the experimental implementation we were partly relying on a commercially available multiplexer for 43 Gbit/s to 172 Gbit/s, the optimum delays could only be approximated. Using the variable delay lines (approximately ± 100 ps) while monitoring the signal on an ultra-high bandwidth optical sampling scope (BW = 500 GHz), precise adjustment (< 100 fs) of the temporal interleaving can be achieved. In each MZI a variable attenuator is installed to compensate for losses in the SMF pieces and asymmetries in the fiber couplers used. At the output a polarizer is used for assuring a single polarization signal.

Phase Relation

Because of the large delays and footprint this interferometric setup is not phase stable in time. This leads to changes in the phase relation of neighbouring bits on a time scale of seconds to minutes. For amplitude modulated signals as used in this work, this means that the data format at 130 Gbit/s constantly varies from RZ-OOK to carrier-suppressed-(CS-)RZ-OOK including the intermediate states. Disregarding the possible influence of the phase constellation on the nonlinearities during transmission, one can also see variations of the signal (both in the time and frequency domain) in back-to-back configuration. The reason is that the pulse tails overlap, leading to coherent cross-talk. Depending on the phase relation, this leads to constructive interference (RZ-OOK, identical phase of neighbouring pulses) or destructive interference (CS-RZ-OOK, alternating phase of neighbouring pulses). Consequently, the amplitude of the signal fluctuates, leading to a fluctuation of the BER performance on the time scale of the phase fluctuation. Therefore, when using short BER integration times below 10 seconds (corresponding to the smallest measurable error rate of 0.25×10^{-9} at 40 Gbit/s), it is possible to overestimate the system performance by far (effective error rate is worse than the one measured). This necessitates longer BER integration times (> 10 second).

3.4.4 Time Demultiplex and Receiver

In this work only optical switches based on electro-absorption modulators (EAMs) are used. Since EAMs being electro-optic devices are driven by an electrical signal, they are easy to handle and do not require additional complex optical elements. In EAMs, a band-edge tilt under the influence of an electric field (RF drive signal) leads to an increased tunnelling probability hence a reduced absorption of the device. Since this effect is ultra-fast, EAMs are widely used as fast electro-optic switches.

All EAMs used later in this work are sourced from the same manufacturer with the same model number and similar specifications (opto-electronic BW = 39.5 GHz). To assess the performance of the EAM, the gating window generated by the EAM is measured for different wavelengths, different drive signal biases, and both TE and TM polarization of the optical input signal (see Fig. 3.7): A CW laser signal is injected into the EAM while it is driven by a sine shaped signal at 43 GHz with a peak-to-peak amplitude of 4 V. The bias of the drive signal is then varied from -1.5 V to -2.5 V and the FWHM of the optical output pulses is measured. This is repeated for different wavelengths. The shapes of the transmission windows are measured with an ultra-fast optical sampling scope.

The setup of the complete 130 Gbit/s to 43 Gbit/s demultiplexer is shown in Fig. 3.7(b). A band pass filter (BP) selects the input channel, a polarization controller (PC) sets the polarization that is launched into the EAM. The device is driven by the 43 GHz clock signal, the bias voltage is set via the bias-T (BW = 65 GHz). The demultiplexed signal is fed into the preamplified 43 Gbit/s receiver (see Section 3.3).

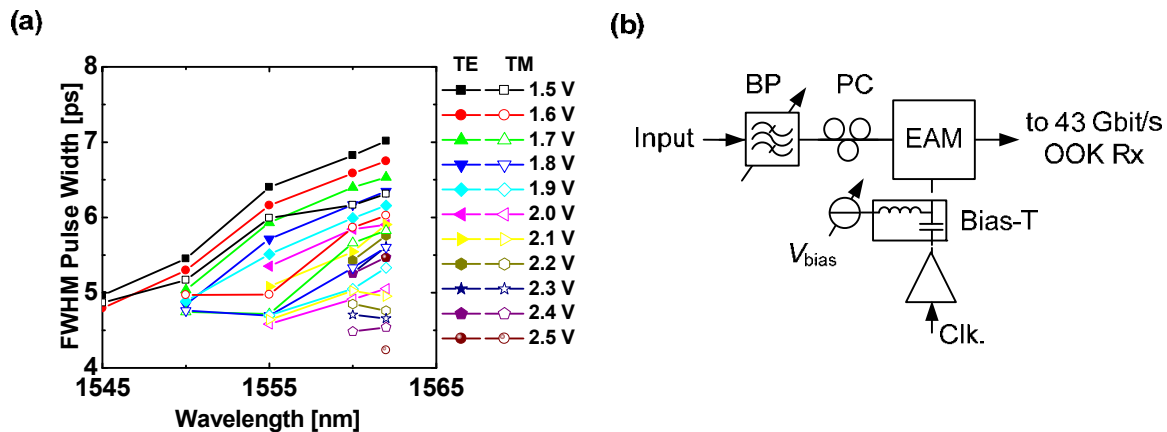


Fig. 3.7. (a) Typical FWHM pulse width of the EAM for different bias voltages depending on the wavelength. Both TE and TM polarization have been measured. (b) Setup of the 130 Gbit/s to 43 Gbit/s demultiplexer. A band pass filter (BP) selects the input channel, a polarization controller (PC) sets the polarization of the input field into the electro-absorption modulator (EAM) for demultiplexing. The EAM is driven by the 43 GHz clock signal, the bias voltage is set via the bias-T. The demultiplexed signal is fed into the preamplified 43 Gbit/s receiver.

3.5 43 Gbit/s RZ-DPSK Transmitter and Receiver

3.5.1 Transmitter

Logic Precoding for DPSK Signals

In case of a differential phase shift keying (DPSK) implementation, logic pre-coding of the bit sequence has to be considered. Clearly, differential coding changes the logic of the original signal: for differential coding, the information is encoded in the transitions between two neighboring logic states, not in the logic states itself. However, for lab experiments using PRBS sequences for DPSK, precoding is not needed. Since all possible combinations occur in a PRBS sequence, all these combinations also appear in the received signal: It is again a PRBS sequence (shifted, maybe inverted). Consequently, in the case of the DPSK format PRBS sequences will be received. The logic operation and experimental implementation of differential precoders and decoders as well as issues when cascading multiple pre- and decoders are discussed in Section 7.2.

Experimental Setup

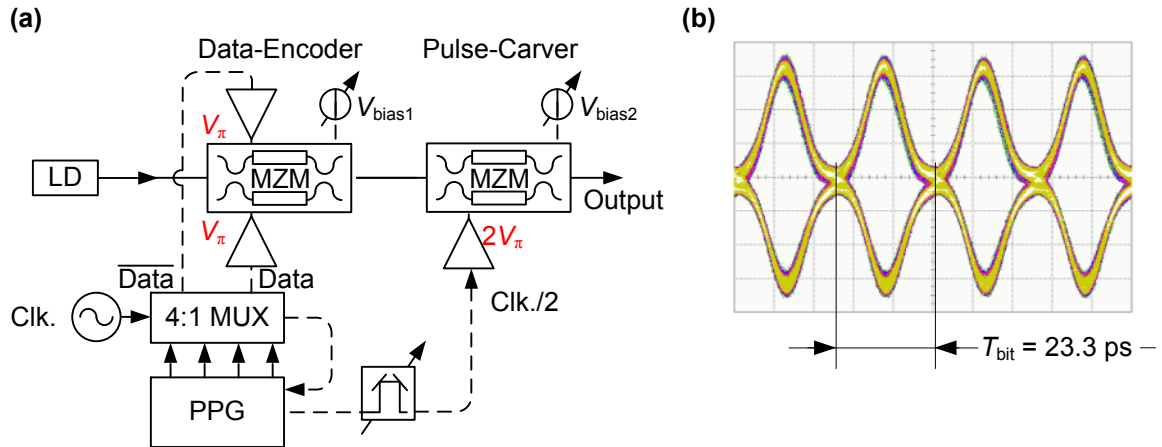


Fig. 3.8. (a) Setup of the 43 Gbit/s DPSK transmitter. A laser diode LD is modulated by two MZMs. The data encoder is a dual-drive push-pull MZM driven with V_π in each arm, modulating the phase of the input field. The pulse pattern generator (PPG) generates 4×10.8 Gbit/s PRBS signals that are TDM multiplexed (MUX). The pulse carver is a single-drive push-pull MZM driven at half the clock frequency with $2V_\pi$ swing. An electrical phase shifter is used for adjustment of the pulse phase with respect to the data signal. (b) Typical output eye diagram of the transmitter after detection with the balanced receiver are described below.

The setup of the DPSK transmitter is depicted in Fig. 3.8(a). A DFB laser diode LD is modulated by two MZMs. Both modulators are push-pull Mach-Zehnder interferometer. The dual-drive data encoder has a 3-dB opto-electronic bandwidth $BW = 36.0$ GHz and is driven by amplitudes of V_π in each arm. The pulse pattern generator (PPG) generates 4×10.8 Gbit/s PRBS signals that are electronically TDM multiplexed (MUX) to 43 Gbit/s. The pulse carver is a single-drive push-pull MZM (3-dB $BW = 36.4$ GHz) driven at half the clock frequency with a peak-to-peak voltage of $2V_\pi$. An electrical phase shifter is used for adjustment of the pulse phase with respect to the data signal. Fig. 3.4(b) shows a typical, very clean output eye diagram of the transmitter in combination with the balanced receiver described below. This configuration has the advantage of producing a chirp-free signal. This setup is used for system characterization in Section 7.2.

3.5.2 Balanced Receiver

The optically preamplified balanced receiver setup is depicted in Fig. 3.9. The channel of interest is selected by a tunable band pass filter with a 3-dB bandwidth (BW) of 2 nm. An Erbium-doped fiber amplifier (EDFA) amplifies the signal which then is again filtered (1nm 3-dB BW) in order to suppress outband amplified spontaneous emission (ASE) noise of the EDFA. For amplifier specifications see Section 3.3.2. A delay interferometer is used for differentially converting the DPSK signal into an amplitude modulated signal [7]. The DI used here is built with SMF 50:50 couplers, the phase shifter (PS) for precise optical carrier phase adjustment is implemented by a heater near one arm of the DI. The two output signals are detected with a balanced detector consisting of two broadband PIN photodiodes (one inverted,

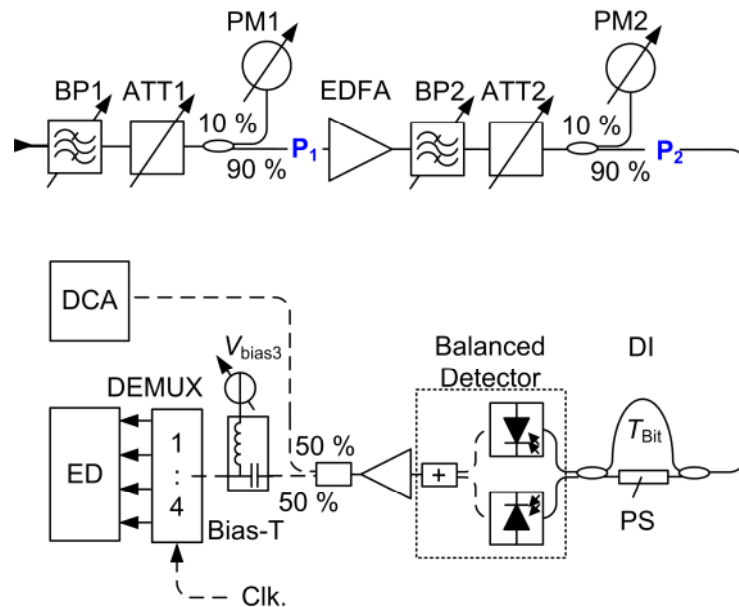


Fig. 3.9. Setup of the balanced receiver with optical preamplifier. The input signal is filtered, optically amplified and filtered again. A delay interferometer (DI) differentially converts the DPSK signal back to an amplitude modulated signal. A balanced detector detects both DI output signals individually. The detected signals are combined, amplified and fed into the DEMUX. The decision threshold for data recovery can be varied via a bias-T. The error detector (ED) measures the BER. BP1, BP2 – band pass filter; ATT1, ATT2 – variable attenuators; PM1, PM2 – power monitors; EDFA – Erbium doped fiber amplifier; DCA – digital communication analyzer; PS – phase shifter. P_1 and P_2 denote optical power levels at different points in the setup.

one non-inverted) with RF bandwidths $BW = 45$ GHz and an RF power combiner with $BW = 65$ GHz. The data signal is recovered and demultiplexed by a 1:4 DEMUX. For Q-factor measurements (for more detail see Appendix A 1.2) the electrical signal can be varied against the decision threshold via a broadband bias-T (65 GHz) at the DEMUX input. The BER is measured with the error detector (ED). For BER vs. input power measurements (see A 1.1), the receiver input power P_1 is adjusted and monitored by an attenuator (ATT1) and a calibrated power monitor (PM1). While varying the input power the power onto the PD has to be kept to the optimum value. This is done by ATT2 and PM2. The measured receiver sensitivity of this setup in combination with the 43 Gbit/s 33% RZ-DPSK transmitter described above is $P_{\text{sens}} = -33.8$ dBm.

3.6 Methods for System Performance Characterization

Bit error ratio (BER) measurements are the most important system performance characterization tools. In measuring the absolute number of errors occurred and, for sufficiently long measurement times, also the bit error ratio, all effects of the system under test can be taken into account. However, measurement of the BER is unspecific to the cause of the error. The BER is defined as the ratio of the number of bits incorrectly received to the total number of bits received during a specific time interval. BER is sometimes erroneously referred to as bit error rate, which is not dimensionless.

A discussion on what trends are to be expected for different measurements of the BER as a function of the received optical power is presented in Appendix A 1.1.

For ultra-low error ratio measurements, BER measurements are meeting their limits: To obtain 100 errors for being able to evaluate the statistical distribution (95 % confidence interval, see [27]), one has to measure 2500 s = 40 min for a BER = 10^{-12} at 40 Gbit/s. For an error rate of 10^{-18} , the measurement time is as long as 79 years.

In a real system, the error ratio is not applicable for performance monitoring since the transmitted bit pattern has to be known for error evaluation. However, a multitude of other (indirect) performance parameters exist for monitoring (optical signal to noise ratio, Q-factor, eye opening penalty etc.). The Q-factor with its measurement techniques is introduced in Appendix A 1.2, for a comprehensive study refer to [28].

4 WDM-to-OTDM Conversion

4.1 Introduction

Optical time division multiplexing (OTDM) is very attractive for next generation transmission systems and networks. A major challenge when time-multiplexing lower-rate wavelength-division multiplexed (WDM) data streams is bit-level synchronisation, especially if the tributaries originate from geographically distant transmitters. In electronic time-division multiplexing, e.g. in SONET/SDH, traffic grooming is made possible by a combination of network-wide clock synchronization and electronic buffers at the TDM multiplexer inputs. This synchronization and storage utilises significant resources and restricts the benefits of optical networking. An alternative concept to the aforementioned synchronization schemes is introduced in [24], which eliminates the need for buffers and enables protocol transparent optical implementations. In this ‘asynchronous retiming’ concept, each TDM multiplexer relies on a high-quality local clock to retime all tributaries, allowing bit-slippages within traffic guard-bands.

Previously, experimental results for a dual-gate asynchronous digital optical regenerator (ADORE) have been presented [29],[30], which performs asynchronous retiming, pulse width adaptation, and wavelength conversion, while at the same time featuring some regenerative properties.

In this work, we propose an optical grooming switch, including WDM-to-OTDM conversion and vice-versa, for interconnecting 42.7 Gbit/s and 128.1 Gbit/s network rings (see Chapter 2). In this chapter, we experimentally investigate the impact of phase alignment in a 3×42.7 Gbit/s to 128.1 Gbit/s WDM-to-OTDM traffic grooming experiment, and we confirm that a number of ADORE units employed in parallel may be considered independently with negligible penalty associated with phase tuning of adjacent channels.

This chapter is organized as follows: First, Section 4.2 introduces the single-wavelength asynchronous retiming concept and its implementation for use in WDM-to-OTDM conversion. In addition, the limits of the network reach for this concept is discussed. Section 4.3 and Section 4.4 present the experimental setup and results for 3×42.7 Gbit/s to 128.1 Gbit/s WDM-to-OTDM conversion. Finally, Section 4.5 summarizes the main results of this chapter.

Parts of this chapter have been published previously in [31] and [32].

4.2 Asynchronous Digital Optical Regeneration

4.2.1 Asynchronous Retiming and Connectivity

In terms of implementation of the WDM-to-OTDM converter, i.e. the subsystem aggregating a number of individual WDM channels (3 channels) of lower data rates to a higher data rate

channel, a synchronous unit is required that will synchronize all individual WDM channels before they are aggregated to a single high data rate channel. The required synchronization can be performed either using a single WDM synchronization unit or a number of individual synchronization units, or more specifically one unit per WMD wavelength channel. In the case that a single WDM synchronization unit is used due to implementation constraints, all WDM channels that are synchronized by this unit need to be of different wavelengths. However, the individual channels that need to be processed by one single WDM-to-OTDM converter may originate from different fiber rings supported by the proposed switching node (see Chapter 2). This implies that if full non-blocking connectivity needs to be provided between the rings (for maximum network flexibility), the channels that are processed by a single WDM-to-OTDM converter may be of the same wavelength in some particular cases. Therefore, although having a single WDM synchronization unit seems to be the most compact solution that will reduce the implementation cost, it comes at the expense of limited overall network performance and flexibility.

This limitation can be overcome by using of a set of synchronization units (one per wavelength channel) that will replace the single WDM synchronization unit. This approach will naturally increase the number of components used in the system but it will improve the flexibility and functionality of the node at the network level, simultaneously offering cost benefits.

4.2.2 Operating Principle

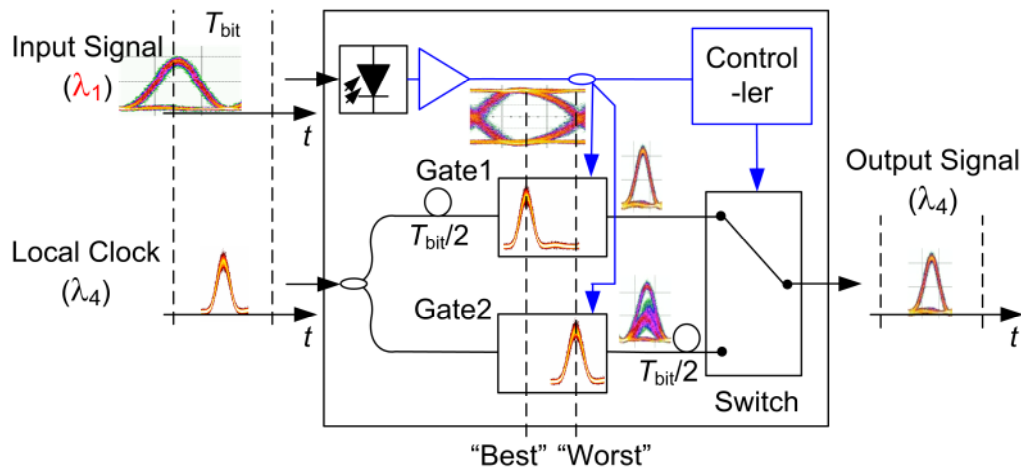


Fig. 4.1. Functional diagram of a dual-gate ADORE. Local optical clock pulses are applied to two gates, one of them being delayed relative to the other by half of the bit period $T_{\text{bit}}/2$. In case of a “1” bit within the RZ-OOK input signal stream, the two gates will be opened simultaneously. Typically, one of the local optical clock pulses will coincide better with the gating window (in this case Gate1 opens optimally, while Gate2 opens at the eye crossing point). The selection of the path with the higher signal quality (Gate1, best signal quality) is provided by the controller in combination with a 2×1 optical switch. For the The output signal is thus retimed and exhibits the pulse width and wavelength of the local optical clock. Insets: eye diagrams; PD – photo diode.

Converting the incoming WDM signals to OTDM is a challenging operation, because it involves simultaneous processing in the wavelength and the time domain. The critical difficulty associated with such conversion arises from the unknown wavelength and clock phase of each of the incoming data signals.

The concept of asynchronous optical digital retiming is depicted in Fig. 4.1 for the case of a single input signal. Our technique is based on the dual-gate ADORE scheme [29], where low bit-rate WDM tributaries are synchronized to the same local clock, pulse widths are shortened and mapped to the same wavelength. In detail, the dual-gate ADORE operates as follows. Local optical clock pulses are generated by a local clock oscillator with a frequency $f_{\text{bit}} = 1/T_{\text{bit}}$ (see Fig. 4.1). These optical clock pulses are applied to the inputs of two gates, one of these inputs being delayed relative to the other by half of the bit period $T_{\text{bit}}/2$. The incoming RZ-OOK signal is detected with a high-speed photodiode and electrically amplified before being applied to the gates as the control signal. In case there is a “1” bit within the input signal stream, the two gates will be opened simultaneously. Typically, one of the local optical clock pulses will be better in synchronization with the gating window, thus leading to a higher signal quality (higher eye opening). By reversing the delays before and after the optical gates, both possible clock signal paths are of identical total length, so that the output signal will be synchronized to the local clock. Selecting the path with the higher signal quality provides the full information of the input signal – yet retimed to the local optical clock and with the pulse width and wavelength of a core ring OTDM tributary.

4.2.3 Implementation

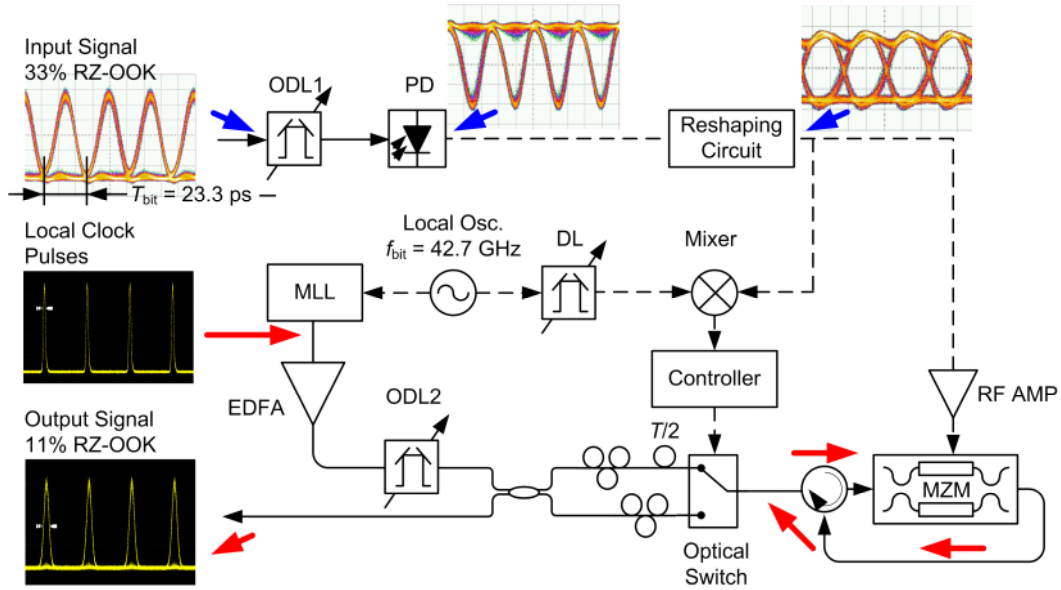


Fig. 4.2. Experimental setup of the 42.7 Gbit/s dual-gate ADORE using a single Mach-Zehnder interferometer (MZM). DL – RF delay line; ODL1, ODL2 – optical delay lines; EDFA – erbium doped fiber amplifier. The insets show typical eye diagrams at various points in the setup.

The experimental setup for the above mentioned dual gate ADORE using a single MZM is shown in Fig. 4.2. This configuration has been proposed in [30]. To generate local optical clock pulses, a mode locked laser (MLL) is used, which is driven by a locally generated RF clock signal at $f_{\text{bit}} = 42.7$ GHz. Note that this local clock is not in synchronisation with the 130 Gbit/s OTDM channels in the core ring (see Fig. 2.3). The locally generated optical pulses are then amplified using an Erbium doped fiber amplifier (EDFA) and split by a 3-dB coupler. The two copies of the clock pulse trains are passed through two optical paths which contained polarization controllers. The two optical paths are arranged to provide a relative delay of half a bit, $T_{\text{bit}}/2 \approx 11.7$ ps, at the output of the optical switch.

The incoming 42.7 Gbit/s RZ-OOK data signal is generated using the transmitter setup described in Section 3.3. The RZ-OOK signal is passed through an optical delay line to vary the relative phase of the data signal to the local ADORE clock signal. The signal is then detected by a high-speed inverting photodiode (PD, 3-dB bandwidth of 45 GHz) before being reshaped by a high-speed logic comparator. The reshaping of the RZ-OOK signal essentially converts the signal to an NRZ-OOK signal, which guarantees a wide switching window for the ADORE operation. The reshaped NRZ-OOK electrical signal is amplified before it is applied to the RF port of a Mach-Zehnder modulator (MZM) biased at the quadrature point (see also Section 3.2). In this way, the MZM is serving as the optical gate for both local clock paths. The optical 1×2 switch then selects the path with the higher signal quality. The selection process is based on the radio frequency (RF) phase comparison between the incoming RZ-OOK data signal and the locally generated clock. These two phases are mixed using a double balanced mixer. The control circuits then sets the optical switch accordingly with a switching

speed of 440 ns. The limited switching speed sets an upper level for the acceptable frequency offset between the local clock and the input signal. If the frequency offset is too large, the switch can not switch fast enough to select the path with momentarily higher signal quality.

Depending on the phase selecting optical switch, the MZM transfers the information from the data signal to one of the paths carrying the clock pulses. This regenerated RZ-OOK output exhibits the same wavelength, pulse width, and clock phase as the local optical clock pulses. The resulting RZ-OOK signal is returned to the optical switch through the circulator. The output signal is now temporally aligned for subsequent OTDM multiplexing, although a one-bit relative delay ambiguity between the two cases is generated. Note that this ambiguity has negligible impact for a burst switched network with guard bands of a few ns, since under normal conditions in this shot guard band no clock changes of a whole bit period will happen. However, initial alignment of the incoming clock phase is required when setting up the ADORE.

Note that for burst traffic, switching is only allowed during guard bands. For this case, a separate input to the switch controller needs to be provided by a low-speed photodiode (not shown in Fig. 4.2) which detects the average power of the input data signal. By increasing the mark/space ratio (ratio of 1's to 0's) of the guard band as compared to the burst, the average power of the guard band is increased and its start is detected by the slow-speed guard-band detection circuitry.

4.2.4 OTDM multiplexing

In addition to synchronization of the incoming lower-bit-rate WDM channels at different wavelengths, WDM-to-OTDM conversion requires wavelength conversion and pulse width adaptation of the WDM channels. Using the ADORE, these three functions are performed simultaneously. In addition, the relative delay between the ADORE output signals need to be adjusting precisely such that they can be correctly interleaved.

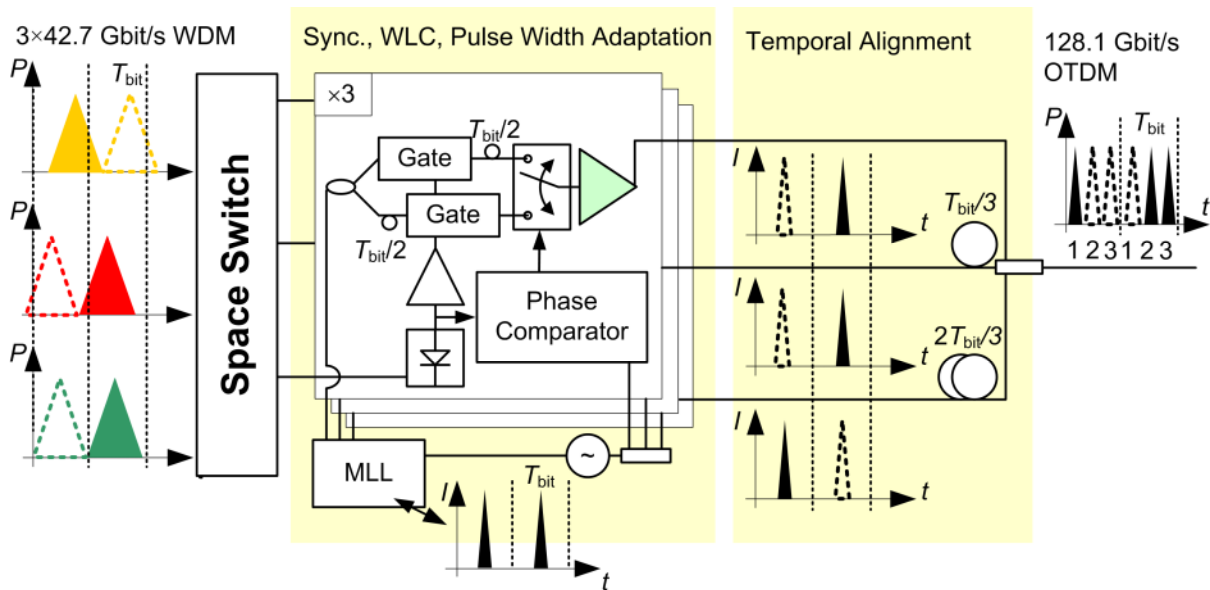


Fig. 4.3. WDM-to-OTDM traffic grooming utilizing the asynchronous retiming concept. The incoming 42.7 Gbit/s signals are synchronized to a local oscillator, wavelength converted and the pulse width is shortened using three ADOREs. The short pulse output signals are temporally aligned and combined to form the 128.1 Gbit/s OTDM signal. Sync. – synchronization; WLC – wavelength conversion; MLL – mode-locked laser.

The concept of WDM-to-OTDM conversion is depicted in Fig. 4.3 for the case where three tributaries are multiplexed to a single OTDM signal. A micro-electro-mechanical system (MEMS) switch (not shown in Fig. 4.3) connects the input tributaries to an equal number of ADORE units. The same ADORE scheme is applied to each of the WDM input signals resulting in three synchronized OTDM tributaries at the same wavelength. The three OTDM tributaries are subsequently temporally aligned and combined to form the OTDM channel. It should be noted that since each ADORE unit is associated with a certain OTDM tributary, by reconfiguring the space switch, time-slot interchange (TSI) can be performed.

4.2.5 Network Reach

It is of interest to consider the possible reach of the asynchronous retiming scheme when one wants to transparently interconnect two distant OTDM domains via a WDM domain using the ADORE units.

For the duration of a data burst (i.e. between guard bands) the ADORE cannot switch to an alternative sampling phase without loss of data. Therefore, during a data burst, random changes in the data phase should not accumulate to more than a small fraction of the bit-slot

duration T_{bit} . In dispersion-compensated links in which small wavelength drifts do not affect travel time, there are two mechanisms which change the data phase: Firstly, the clock accuracy is limited leading to a frequency deviation between the local clock to the ADORE and the remote one. Secondly, the travel time in the fiber might vary, which – in the absence of residual dispersion – depends on its thermal expansion coefficient.

In terms of clock accuracy, technological advancements in chip-scale atomic clocks [33] to accuracies better than 10^{-11} enable the introduction of affordable, compact atomic clocks in metro-access and core networks. Therefore, if we consider 2 parts in 10^{11} relative drift in frequency between two clocks of 10^{-11} accuracy, 40 GHz clock frequency, and 1 ms data burst length, the expected maximum phase drift within a data burst would be less than $10^{-3} T_{\text{bit}}$ [24].

Let us consider a typical value for fiber thermal expansion of 10^{-6} [6] (which is equivalent to 0.5 nm/100 km/°C), and a 1°C uniform change in temperature over 8 minutes over a ultra-long haul (ULH) link. In this case, asynchronous retiming can exceed 100,000 km reach with 1 ms data burst length at 40 Gbit/s, assuming that the ADORE can tolerate $10^{-1} T$ phase drift within a data burst.

Therefore, it is likely that the asynchronous retiming concept will also work over global distances. However, studies on the statistics of short term travel time variations due to fiber expansion over ULH links would need to be done to confirm the above.

4.3 Experiment

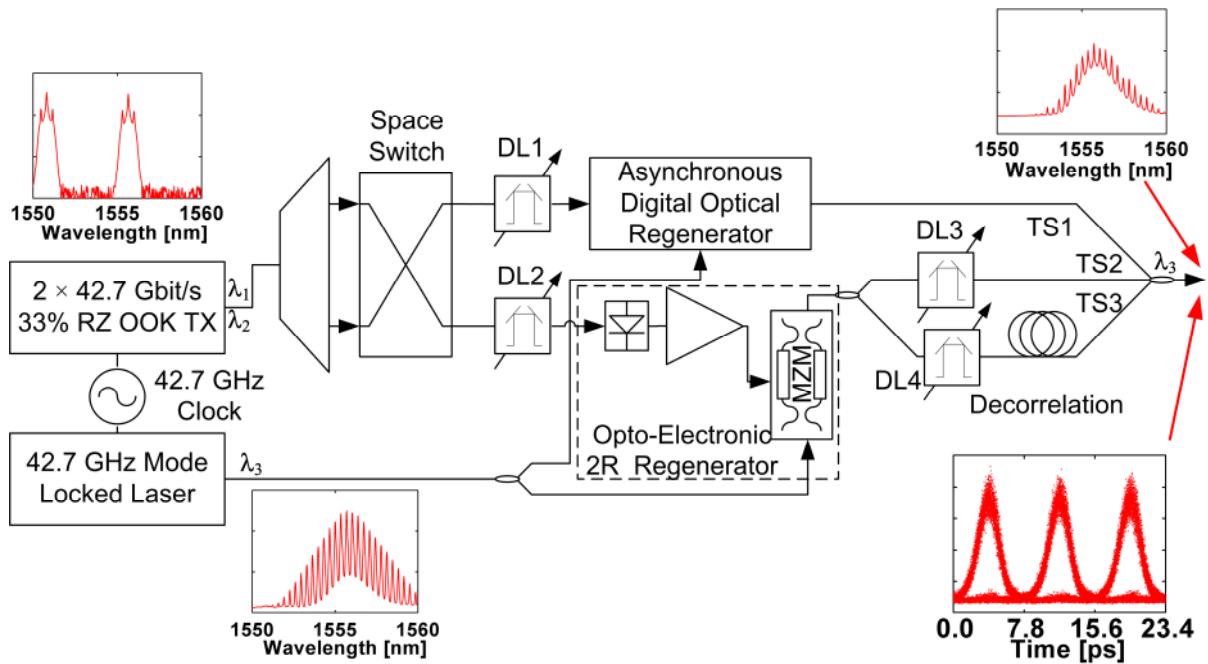


Fig. 4.4. Experimental implementation of the WDM-to-OTDM conversion with timeslot interchange using one asynchronous digital optical regenerator (ADORE) and one opto-electronic 2R regenerator. (The vertical scale on the optical spectra plots is 20dB/div). Due to equipment constraints, the setup is implemented using one full ADORE and a simple opto-electronic 2R regenerator.

Fig. 4.4 depicts the experimental setup (note that optical attenuators, amplifiers, and polarisation controllers are not shown, for clarity). Due to equipment constraints, the WDM-to-OTDM conversion setup is implemented using one full ADORE and one simple opto-electronic 2R regenerator.

Two continuous 42.7 Gbit/s 33% RZ-OOK $2^7 - 1$ PRBS signals at $\lambda_1 = 1550.92$ nm and $\lambda_2 = 1555.75$ nm are generated by a transmitter comprising two Mach-Zehnder modulators (MZMs) for data encoding and pulse carving (see Section 3.3.1 for more details). These channels are subsequently wavelength demultiplexed and connected to the MEMS space switch. One of the channels is input to an ADORE. The other channel is input to a simple opto-electronic (O-E) 2R regenerator comprising a photodiode (PD), an RF amplifier, and a MZM. This MZM-based O-E 2R regenerator has a performance nominally identical to that of the ADORE when being operated at fixed and optimum input data phase (However, the performance experienced was slightly worse for the O-E 2R regenerator than for the ADORE due to specification differences in the component). Consequently, retiming capability is attained only with the ADORE, whereas the input data bit-slot phase to the O-E 2R regenerator has to be maintained at optimum. Variable optical delay lines (DLs) at both the ADORE (DL1) and the O-E 2R regenerator (DL2) inputs are used in order to control the data bit-slot

phase with respect to the phase of the optical clock. DL2 in front of the O-E 2R regenerator is adjusted to ensure optimum data phase at all times. DL1 in front of the ADORE is varied before each experimental condition in order to test the performance under various optimum and non-optimum data phases. The output of the O-E 2R is split by a 50:50 splitter into two paths in order to create two OTDM tributaries. These two identical OTDM tributaries (TS2 and TS3) are subsequently decorrelated by adding 20 cm of fiber length, which corresponds to approx. $1/3$ of the $2^7 - 1$ PRBS pattern length at 42.7 Gbit/s. DL3 and DL4 are used in both of these paths to control the relative delays of the three tributaries in order to form the OTDM signal after the output couplers, with the tributaries TS1, TS2, and TS3 at relative delay 0, $T_{\text{bit}}/3$, and $2T_{\text{bit}}/3$, respectively. Demultiplexing of the three tributaries for subsequent bit-error rate (BER) testing is accomplished with the 130-Gbit/s receiver with optical preamplifier introduced in 3.4.4.

4.4 Results and Discussion

To show that error free WDM-to-OTDM multiplexing is possible independent of the respective clock phase of the WDM input signals, we performed an experiment as follows: While keeping the relative time synchronization of two OTDM tributaries (timeslots TS2 and TS3) optimum we varied the input WDM signal synchronization of a third tributary (TS1) over a whole bit period while observing the BER performance of all three OTDM tributaries. Fig. 4.5(a) shows the sensitivity penalty of the three tributaries after demultiplexing using an EAM. TS1 was measured at both best ('ADORE best') and worst input data synchronization ('ADORE worst'), see also Fig. 4.1. The worst synchronization corresponds to the point just before or just after the dual-gate ADORE switches from one optical path to the other. Measurements on either side of the switching window (corresponding to crossing points of the input data eye diagram in Fig. 4.1) were taken ('ADORE worst 1' and 'ADORE worst 2'). The

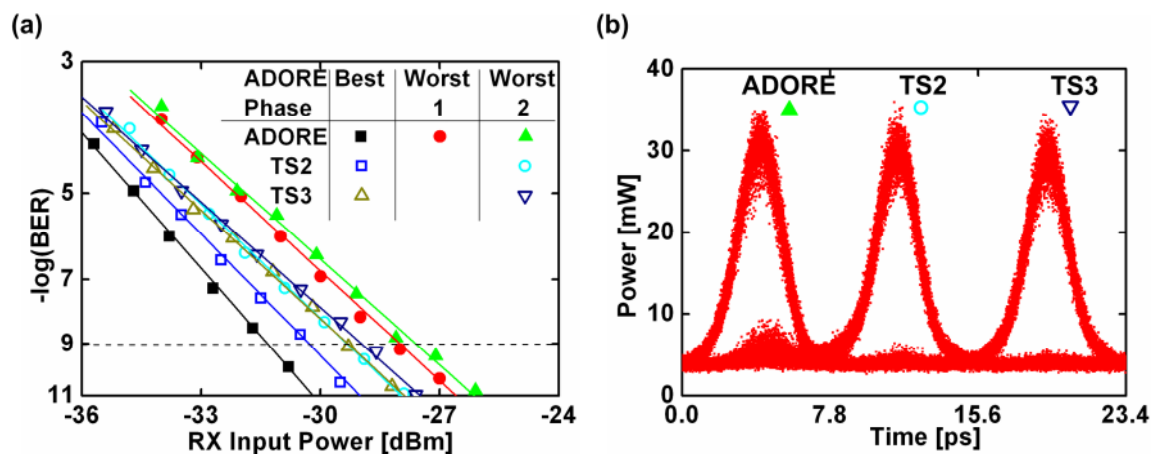


Fig. 4.5. (a) Receiver bit error rate measurements for the three OTDM tributaries (namely ADORE, TS2, TS3) under best and worst input data clock phases to the ADORE. (b) Eye diagram (Picosolve™ optical sampling scope) for the worst input phase to the ADORE.

worst phase position was verified before each curve was taken by precisely adjusting the T/2 delay inside the ADORE. It can be seen that the variation of receiver sensitivity between best and either of the worst data phases was approx. 3.5 dB (at BER = 10^{-9}). The majority of this sensitivity penalty is attributed to a slight degradation in the extinction ratio corresponding to small signal levels leaking through from adjacent bit slots for the worst case relative phase (see also ADORE time slot in Fig. 4.5(b)). The other two time-slots (TS2 and TS3), corresponding to the output of the O-E 2R regenerator, were also measured under best and worst ADORE phase, in order to investigate whether data phase variations at the ADORE input affect the other OTDM time-slots. The curves ‘TS2 ADORE best’ and ‘TS2 ADORE worst’ correspond to the TS2 slot when the data input to the ADORE was at best and worst phase, respectively. Corresponding curves were also taken for TS3. It can be seen that the performance of TS2 degrades by 1 dB, while TS3 does not degrade as the data phase is varied to the ADORE input. Fig. 4.5(b) shows the 128.1 Gbit/s eye diagram that was recorded at the EAM input, in the case of worst data phase at the ADORE input, and when the TS2 was found to be degraded. With reference to Fig. 4.5(b), the TS2 degradation most likely originates from demultiplexing cross-talk due to the imperfect EAM used in the receiver, in combination with the presence of residual power in the TS1 (“ADORE”) ‘0’s to the side of the TS2. The Picoscope™ high bandwidth optical oscilloscope also indicates that there is no cross-talk between the channels before demultiplexing. These results are expected to hold also for the case where all three WDM channels are retimed using identical single-wavelength ADOREs.

4.5 Summary

In this chapter we proposed and experimentally investigated data protocol transparent 3×42.7 Gbit/s to 128.1 Gbit/s WDM-to-OTDM conversion based on an asynchronous retiming scheme. Bufferless OTDM traffic grooming with a worst case power penalty of less than 3.5 dB has been demonstrated. The results show that, after demultiplexing, the BER fluctuations due to phase variability are limited to the tributary channel of interest, and negligible crosstalk variation is observed. The network reach when using asynchronous retiming in combination with burst mode traffic (1 ms data burst length) is estimated to exceed 100,000 km.

5 OTDM-to-WDM Conversion

5.1 Introduction

All-optical networks operating at ultra-high bit rates are characterized by the coexistence of different multiplexing schemes: Whereas optical time division multiplexing (OTDM) is deployed in higher hierarchy parts of the network (metro/backbone network), wavelength division multiplexing (WDM) running at lower bit rates can be found closer to the end user of the network (metro/access network). One of the key functions in all-optical networks is hence the mapping of an OTDM-signal to different WDM-channels. A practical solution requires simultaneous demultiplexing of all OTDM channels with a single device. Simultaneous demultiplexing of four and three WDM channels has been reported in the past using either four-wave mixing [34] or self-phase modulation related spectral broadening [35], respectively. In this chapter, we experimentally demonstrate two different OTDM-to-WDM conversion schemes, which convert a 130 Gbit/s OTDM signal to three 43 Gbit/s WDM signals.

The first technique is based on self phase modulation (SPM) in a highly nonlinear fiber (HNLF). In our implementation, a 130 Gbit/s OTDM signal was replicated in three copies at different wavelengths and the resulting signals were delayed to achieve relative timing shifts of one bit period followed by temporal demultiplexing to obtain the 43 Gbit/s WDM signal. For the multi-wavelength conversion we used the technique presented by Mamyshev [4], which is based on offset filtering of a self-phase modulation (SPM) broadened spectrum. BER measurements show no error floor and a maximum of 2.2 dB penalty for the central channel at $\text{BER} = 10^{-9}$. The results were published partly in [32]. Note that the Mamyshev-technique is also used for performing multi-wavelength regeneration in this work (see Section 7.1).

As a matter of fact, SPM techniques are not fully flexible in terms of output wavelength allocation. XPM-based techniques could basically give a user the freedom to map any OTDM channel to any desired output wavelength. The second technique is therefore based on cross-phase modulation XPM.

An XPM based technique where an OTDM channel has been mapped onto a sequence of rectangularly-shaped, linearly-chirped pulses within a nonlinear optical switch has been proposed in the past. Such pulses can be generated using either a commercial dynamic gain equalizer [36],[37], or a chirped fiber Bragg grating (CFBG) [38]. However, the studies reported in [38] highlighted the strong dependence among the key system parameters, such as chirp, switching efficiency and WDM channel separation at high repetition rates for optimal OTDM to WDM conversion performance.

To relax these parameter dependencies, we used a specially designed and manufactured highly nonlinear fibre (HNLF) minimizing the channel walk-off and reducing the cross-talk between the various WDM channels. The HNLF was included inside a nonlinear optical loop mirror (NOLM). Three different WDM probe pulse streams were input to the NOLM and the

OTDM signal was used as a control signal to switch the time interleaved WDM probes. Using this technique, we report the first demonstration of OTDM-to-WDM conversion from 130 Gbit/s simultaneously to three 43 Gbit/s WDM channels. The success of the experiment depends crucially on a novel specially designed highly nonlinear fiber (HNLF) exhibiting low dispersion and low dispersion slope such that low walk-off operation across the C-band is possible. Error free performance is achieved with penalties ranging from 0.5 dB to 3.5 dB for all three WDM channels. This enables full flexibility for selecting the output WDM channel wavelengths as required in future all-optical networks. The results were with some modifications published in [39].

This chapter is organized as follows: In Section 5.2 the solution based on spectral broadening and offset filtering is presented. As the underlying wavelength conversion technique is discussed in detail in the chapter on multi-wavelength regenerators (see Section 7.1), only its application to OTDM-to-WDM conversion is presented. Then the actual implementation and experimental validation of this conversion concept is reported.

Section 5.3 discusses the basic principle of the NOLM operation as a wavelength converter, points out the practical implications when moving toward high bit rates and draws conclusions about the optimization of the operation of the NOLM. Also, the challenges when moving to multiwavelength operation are identified and the key parameters for improving the performance of the NOLM for OTDM-to-WDM conversion applications are derived. Finally, we experimentally proof the concept.

Finally, in Section 5.4, we compare the two concepts in terms of performance, complexity of the setups and ease of operation. This comparison leads to the decision which solution is later used in the full switch node demonstration presented in Chapter 8).

5.2 SPM Based OTDM-to-WDM Conversion

5.2.1 Operation Principle

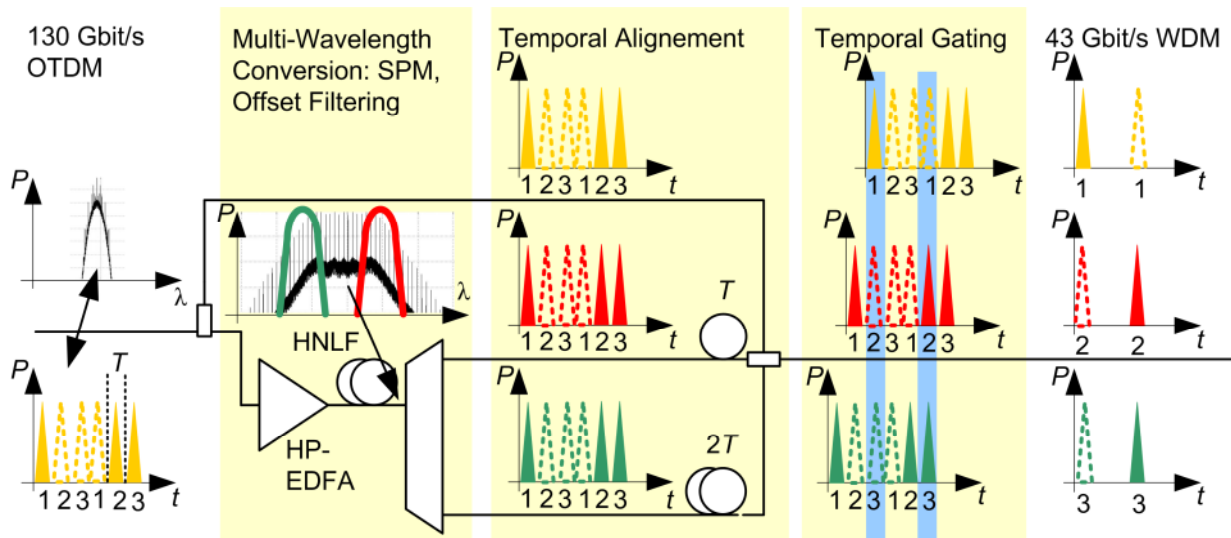


Fig. 5.1. Operation principle of the OTDM to WDM conversion. HP-EDFA – high-power EDFA; HNLF – highly-nonlinear fiber.

The operating principle of the OTDM-to-WDM conversion unit is illustrated in Fig. 5.1 [40]. Here a 130 Gbit/s OTDM signal is converted to three WDM tributaries running at 43 Gbit/s each. This is achieved through the following three-stage process. In a first stage, the 130 Gbit/s OTDM signal is replicated at three different wavelengths by means of a multi-wavelength converter. The multi-wavelength conversion process is based on a technique proposed by Mamyshev [4]. Using a highly nonlinear Kerr medium, which in our case is a highly nonlinear fiber (HNLF), the input OTDM signal experiences spectral broadening due to the self-phase modulation (SPM) effect. Two replicas of the input signal are then obtained by performing simultaneous symmetrical filtering on the right and left sides of the broadened spectrum. The third replica is obtained by just tapping of part of the signal power before entering the HP-EDFA. The second stage of the subsystem performs temporal alignment of the time slots of the three tributaries. This is achieved by an array of optical delay lines (ODLs). In the final step, temporal gating of the three replicas takes place, which isolates every third pulse in its corresponding WDM channel. For this operation we used a commercially available electro-absorption modulator (EAM).

5.2.2 Scalability

In principle, this scheme is not limited to 1-to-3 conversion since it is based on SPM and offset filtering. Properly optimizing the input power and the HNLF increases the spectral broadening, and thus more output WDM channels are practicable. A conversion of 40 Gbit/s to four 10 Gbit/s channels has been demonstrated [35].

More importantly, due to the fixed filters, the subsystem can only accept a specific input wavelength. However, scalability of the OTDM-to-WDM subsystem is provided by adding additional wavelength-specific OTDM-to-WDM converters for each core channel that needs to be dropped.

5.2.3 Experimental Setup

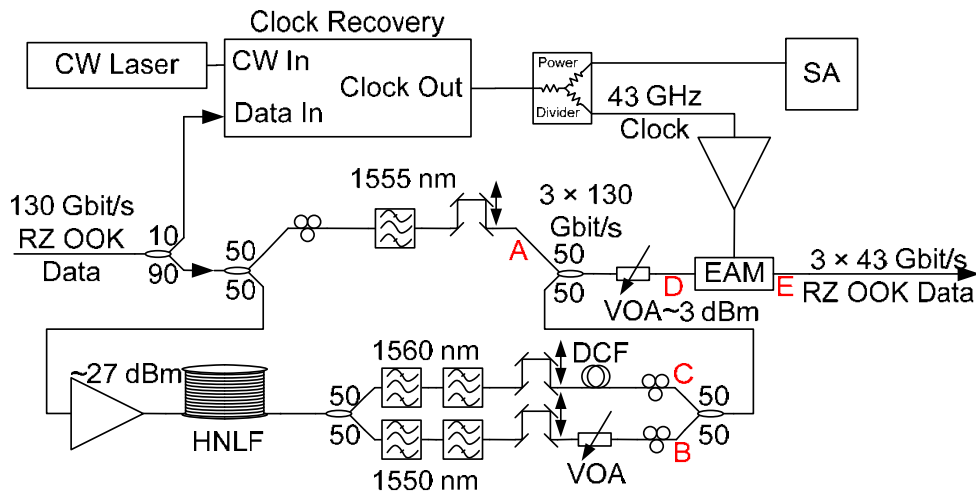


Fig. 5.2. Experimental implementation of the OTDM-to-WDM conversion. SA – spectral analyzer.

The experimental setup is shown in Fig. 5.2. As a source for the 130 Gbit/s OTDM signal, the setup explained in Section 3.4 is used at a centre wavelength of 1555.75 nm. The pulses are intensity modulated with a 43 Gbit/s $2^{31}-1$ PRBS data stream. The resulting signal is time-multiplexed to form the 130 Gbit/s OTDM signal. The optical output pulses have a full-width at half maximum (FWHM) of 2.4 ps.

When entering the setup, 10 % of the signal power is tapped off and fed into the clock recovery subsystem. Details on the clock recovery are given in Chapter 6. The signal is then divided equally into two branches: one is fed to the wavelength conversion setup while the other keeps the original signal. To perform the wavelength conversion, the OTDM signal is launched, with 27 dBm of average power, in a commercial highly non-linear fiber (HNLF) with a length of 310 m, a dispersion of $C = -0.31$ ps/nm/km, a dispersion slope of $D = 0.0031$ ps/nm²/km, a nonlinear coefficient of $\gamma = 20$ /W/km and a loss parameter of $\alpha_{dB} = 1.21$ dB/km (all values measured at 1550 nm). After spectral broadening due to SPM in the HNLF, the offset filtering is performed by two cascaded tuneable filters for each wavelength. The filters are Gaussian shaped, with 2 nm optical bandwidth, two of which are centred at 1550.92 nm and the other two at 1560.61 nm. The filters are cascaded in order to suppress crosstalk among the output WDM channels. The bypass path is also filtered using a 2 nm filter to reduce crosstalk to the other channels. In addition to this, an optical attenuator is used to reduce the power in the 1550.92 nm path. In the 1560.61 nm path, 5 m of dispersion compensating fiber (DCF) is added in the to compensate for dispersion in the HNLF, shorten-

ing the pulse before temporal gating. The two offset filtered paths are now recombined using a 3-dB coupler. Its output is then combined with the bypass path in another 3-dB coupler. The combined signal power is then attenuated to an average power of 3 dBm at the input of the temporal gate. The temporal gate is an electro-absorption modulator (EAM) with an opening window of 5 ps FWHM at 43 GHz. The EAM is driven by an RF amplifier with an integrated bias-T. The 43 GHz clock drive signal is supplied by the clock recovery. After gating, each channel of the resulting WDM signal is filtered and subsequently fed to an optical receiver (for details see Section 3.3) for BER measurements.

5.2.4 Results and Discussion

To study the performance of the wavelength conversion, the input signal was measured at point A in Fig. 5.2. The measured eye diagram and corresponding quality factor $Q^2 = 23.4$ dB are shown in Fig. 5.3(a).

The converted signals at point B and C in the setup are shown in Fig. 5.3(b) and Fig. 5.3(c), respectively. The Q-factors are degraded slightly in both cases if compared to the input Q-factor. Looking at the eye diagrams of the converted signals, it can be seen that the noise on the zero rails is reduced significantly while the noise on the top rail is increased. This is due to the spectral broadening and subsequent offset filtering necessary for the wavelength conversion. The performance of the wavelength conversion could be improved further if the filter offsets would be optimized for optimum performance. In this work the wavelengths were fixed to the grid predefined by the overall switch node layout and had to be compatible with the ITU-T standard for the WDM frequency grid (confer ITU-T recommendation G.694.1).

Fig. 5.4(a) shows the optical spectrum after recombining the wavelength-converted signals with the filtered bypass signal at measurement point D in Fig. 5.2. The three copies of the signal are now adjusted in phase and then simultaneously demultiplexed in time using a single EAM. This leads to the optical spectra shown in Fig. 5.4(b).

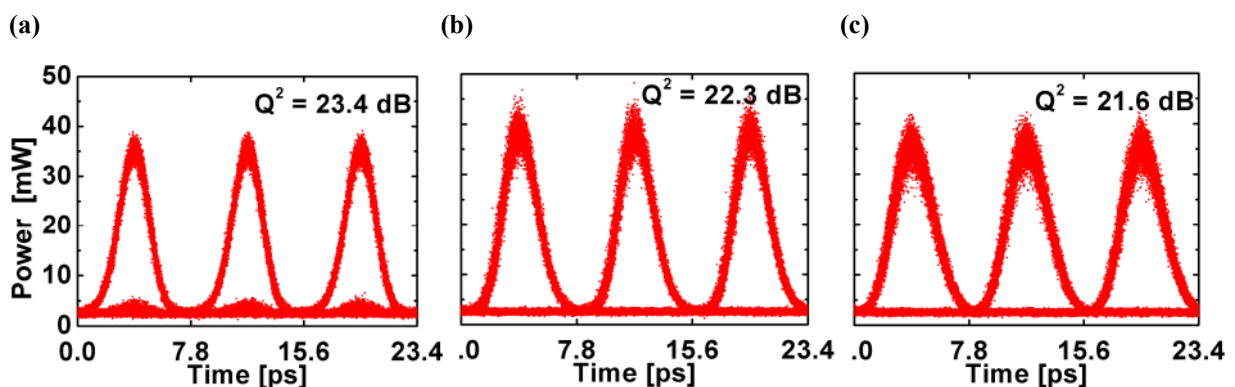


Fig. 5.3. (a) Filtered input signal at 1555.75 nm (Point A). FWHM pulse width 2.41 ps, RMS jitter 81 fs. (b) Wavelength converted signal at 1550.91 nm (Point B). FWHM pulse width 2.71 ps, RMS jitter 148 fs. (c) Wavelength converted signal at 1560.61 nm (Point C). FWHM pulse width 3.19 ps, RMS jitter 147 fs.

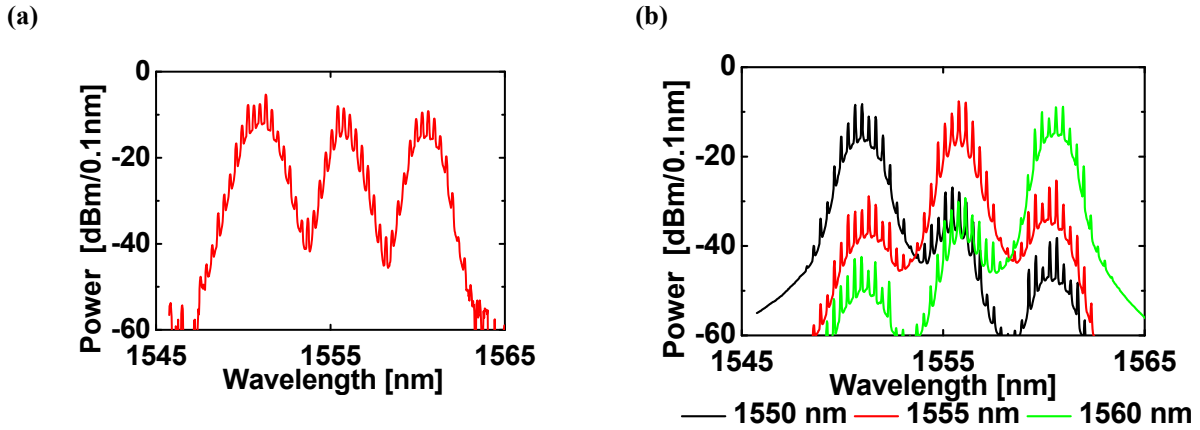


Fig. 5.4. (a) Optical spectrum in the OTDM-to-WDM subsystem right before demultiplexing (Point D). (b) Optical spectra after temporal demultiplexing with the EAM and spectral demultiplexing with a 3 nm Gaussian shaped filter.

The eye diagrams and Q factors of the demultiplexed signals at 1550.92 nm, 1555.75 nm, and 1560.61 nm are shown in Fig. 5.5(a)-(c). The shortest wavelength channel exhibits the lowest Q^2 of all three WDM channels. The non-wavelength converted signal at 1555.75 nm shows the performance that can be achieved by simply demultiplexing the OTDM input signal with the EAM (operating conditions: -1.6 V bias and 4 V_{p-p} sinusoidal drive voltage). The demultiplexed signal at 1560.61 nm exhibits the highest Q^2 , however, a significant crosstalk from neighboring timeslots is observed that can degrade the signal quality when it is detected with a low bandwidth photodiode (~ 40 GHz). This is due to the fact that the operating conditions of the EAM are optimized for a good overall performance and not separately for each wavelength. Looking at the Q factors of the eye diagrams measured with the high bandwidth optical sampling scope, the signal at 1560.61 nm would be expected to have best bit error rate performance. To study the impact of the low bandwidth photodiode and the real system performance, bit error rate curves are measured of the directly demultiplexed back to back signal as well as of the three WDM output channels.

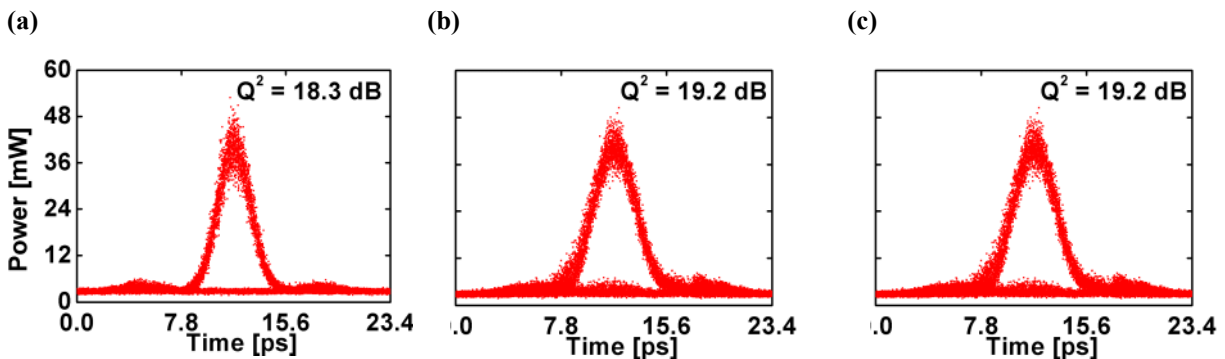


Fig. 5.5. Eye diagrams of the demultiplexed signals forming the WDM channels measured at Point E. (a) Signal at 1550.92 nm with FWHM pulse width of 2.84 ps and RMS jitter of 178 fs. (b) Signal at 1555.75 nm with FWHM pulse width 3.73 ps and RMS jitter of 219 fs. (c) Signal at 1560.61 nm with FWHM pulse width 3.44 ps and RMS jitter of 206 fs.

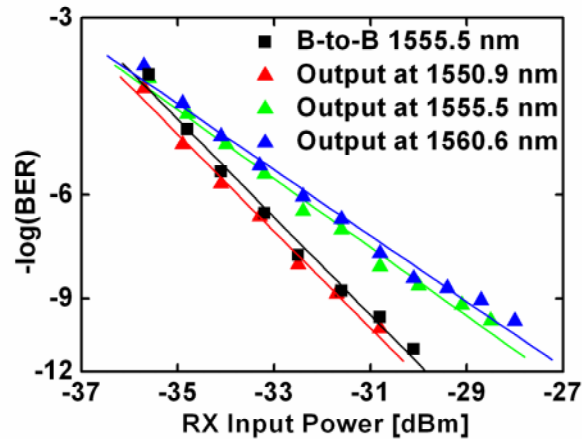


Fig. 5.6. Receiver bit error rates of the three 43 Gbit/s outputs of the OTDM-to-WDM subsystem and the 130 Gbit/s input signal to the subsystem demultiplexed with the same EAM as used in the subsystem. A small maximal penalty of 2.2 dB compared to the back-to-back (B-to-B) signal is observed for the 1560.6 nm output signal.

The bit error rate curves shown in Fig. 5.6 prove error free operation. Error free operation ($\text{BER} \leq 10^{-9}$) is achieved for all the WDM channels with power penalties (p_i) of only $p_1 \approx -0.1$ dB, $p_2 \approx 1.9$ dB, and $p_3 \approx 2.2$ dB for 1550.9 nm, 1555.5 nm, and 1560.6 nm, respectively, compared to the back-to-back signal.

We attribute the power penalties and the developing error floor for longer wavelengths to the wavelength dependent performance of the EAM. The FWHM of the EAM switching window for 1550.9 nm, 1555.5 nm and 1560.6 nm are 4.8 ps (4.7 ps), 5.5 ps (4.8 ps) and 5.9 ps (5.1 ps) for TE (TM) polarization, respectively. The wider windows with increased variations for the longer wavelength lead to increased crosstalk from neighbouring TDM bit-slots (see also the corresponding eye diagrams in Fig. 5.5(a)-(c)). The subsystem performance can be further improved by choosing an EAM with optimized performance (shorter switching windows, less wavelength dependence) in the signal wavelength range.

5.3 XPM-based OTDM-to-WDM Conversion using an NOLM

5.3.1 Operation Principle

Wavelength conversion in a NOLM is based on the cross-phase modulation (XPM) effect, which is a direct consequence of the Kerr effect: The effective refractive index seen by a weak, low-intensity optical beam in a nonlinear medium is influenced by the intensity of the other beams propagating along the same fiber. Fig. 5.7 shows the operating principle of the proposed technique [41]. The three WDM probe pulse signals ($\lambda_{1,2,3}$) are temporally aligned to different time slots of the OTDM signal and are launched to the input port of the NOLM. The input coupler splits the WDM signals equally in two, one co-propagating with the OTDM signal, the other one counter-propagating. If the OTDM pulse is absent (“0”), the two counter-propagating parts of each WDM signal acquire identical linear phase shifts as they traverse the loop and interfere constructively at the input port of the NOLM such that no signal is transmitted to the output (“0”). If the OTDM pulse is present (“1”) at another wavelength ($\lambda_{control}$), the loop is unbalanced by a nonlinear phase shift due to XPM. If this phase shift amounts to π at the optical carrier frequency, the two counter-propagating parts of each WDM signal interfere destructively at the input port of the NOLM and are therefore transmitted to the output (“1”). This switch effectively transfers coded information from a signal at one wavelength ($\lambda_{control}$) to another at different wavelengths ($\lambda_{1,2,3}$).

For multi-wavelength operation of the NOLM an accurate control of dispersion and

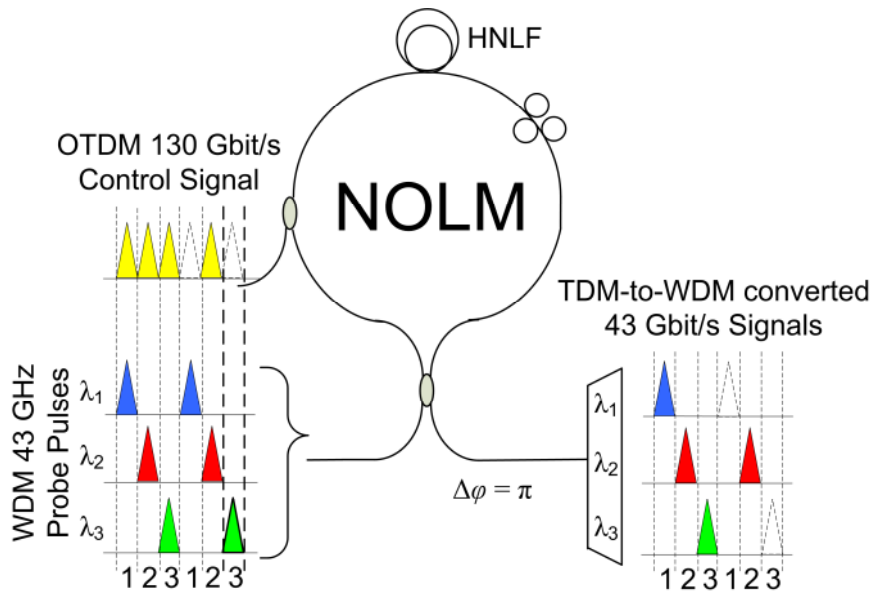


Fig. 5.7 Operation principle of the OTDM-to-WDM conversion technique. Three WDM probe signals are temporally aligned to different time slots of the TDM data signal. The presence of TDM data pulses induces a phase imbalance in the loop, leading to constructive interference of the WDM probe pulses in the output port of the NOLM. The scheme effectively transfers coded information from a signal at one wavelength ($\lambda_{control}$) to another at different wavelengths ($\lambda_1, \lambda_2, \lambda_3$).

dispersion slope of the fiber is needed for a low walk-off and an uniform switching efficiency across the whole bandwidth of the WDM channels.

Quantitatively, the transmittance of the NOLM, T_{NOLM} , amounts to [41]:

$$T_{\text{NOLM}} = \sin^2 \left(\frac{\Delta\phi}{2} \right) \quad (5.1)$$

and depends on the net phase shift difference, $\Delta\phi$, between the co- and the counter-propagating pulses inside the loop,

$$\Delta\phi = \Delta\phi_{\text{co-propagating}} - \Delta\phi_{\text{counter-propagating}} \quad (5.2)$$

Provided that all signals have the same state of polarization, the co-propagating phase shift is given by (with $z = 0$ at the fiber coupler that couples the WDM probe pulses to the NOLM)

$$\Delta\phi_{\text{co-propagating}} = 2\gamma \int_0^L P(t - Wz) dz, \quad (5.3)$$

where γ is the nonlinear coefficient of the fiber in the loop, $P(t)$ is the time dependent pump power measured in a moving time frame with reference at the centre of the probe pulse, L is the fiber length and W is the walk-off parameter defined by [42]:

$$W = \left| \frac{1}{v_{gr}(\lambda_{\text{control}})} - \frac{1}{v_{gr}(\lambda_{\text{probe}})} \right|. \quad (5.4)$$

The quantity v_{gr} denotes the group velocity calculated at the wavelength of the control and probe signals.

In contrast to that, the counter-propagating phase shift is equivalent to the XPM induced by the time-average power of the control pulses and has the following form:

$$\Delta\phi_{\text{counter-propagating}} = 2\gamma\sqrt{\pi}P_{0,\text{control}}Lf_{\text{control}}, \quad (5.5)$$

where $P_{0,\text{control}}$ is the control peak power, $T_{0,\text{control}}$ is the full width at 1/e of the control pulse intensity profile and f_{control} is the control pulse repetition rate. Note that this equation assumes the control pulse shape to be Gaussian, however similar equations can be written for different pulse shapes. In addition, note that Eqs. (5.3) and (5.5) assume that the fiber in the NOLM has no loss. For a more accurate treatment, the loss can be taken into account (see for example [42]).

As can be seen from Eq. (5.5) the counter-propagating phase shift effect is constant in time and increases when increasing the ratio between the pulse width and the repetition rate of the control signal, e.g. by increasing the duty cycle. This counter-propagation phase contribution might cause problems of maintaining an adequate extinction ratio of the switch at high bit rates (> 40 Gbit/s) or at a high duty cycle. If a non-polarization maintaining NOLM is used, a controlled amount of ‘‘optical bias’’ (i.e. phase difference) between signals propagating through the loop in opposite directions can be generated by the polarization controllers inside the loop, so that it is possible to cancel out the counter-propagation phase effect, as will be

experimentally demonstrated in subchapter 5.3.4. In this way, full-swing switching with the maximum extinction ratio is achieved.

From Eqs. (5.1), (5.3) and (5.5) it can be understood that by controlling the peak power level of the pump pulses, the NOLM either switches ($\Delta\varphi = \pi$) the probe signal in case of a “1” bit or does not switch ($\Delta\varphi = 0$) the probe signal in case of a “0” bit, respectively. In this way it is possible to transfer coded information from the control signal at one wavelength ($\lambda_{control}$) to the probe signal at a different wavelength (λ_{probe}), i.e. perform wavelength conversion of the signal.

This 1×1 wavelength conversion can easily be extended to an $1 \times N$ conversion (see Fig. 5.7) using several probe signals at different wavelengths, as required for the OTDM-to-WDM conversion needed in the switch node. The nonlinear interaction within the HNLF does not depend on electronic resonances. It is hence essentially independent of wavelength and allows for wavelength flexibility. However, for multi-wavelength operation the effects of dispersion and cross-talk on the overall performance of the NOLM have to be carefully taken into account.

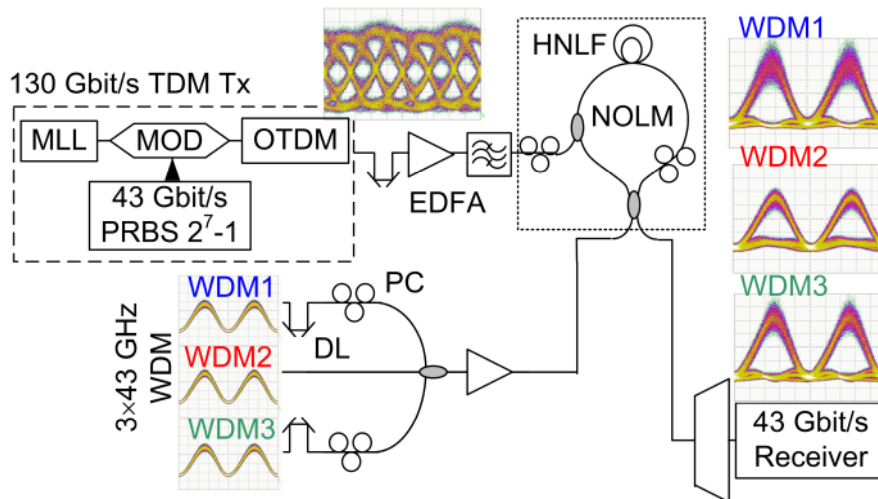
5.3.2 Scalability

In principle, this scheme is not limited to 1-to-3 conversion at 130 Gbit/s since it is based on XPM. By moving to 160 Gbit/s for the OTDM signal and increasing the input power to the HNLF accordingly, four 40 Gbit/s output WDM channels are feasible.

While this concept is in principle not limited to a single OTDM input channel, in practice, accurate control of the dispersion and dispersion slope of the HNLF over such a large bandwidth is not realistic. However, scalability of the OTDM-to-WDM subsystem is provided by adding additional wavelength-specific OTDM-to-WDM converters for each core channel that needs to be dropped.

5.3.3 Experimental Setup

(a)



(b)

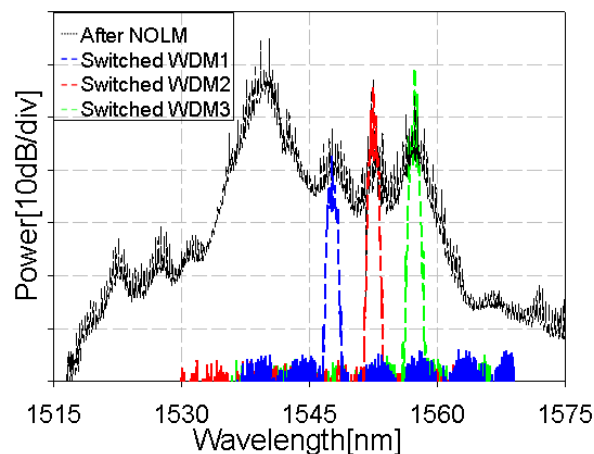


Fig. 5.8. (a) Experimental setup of the TDM-to-WDM conversion. The data pulses of the 130 Gbit/s transmitter (Tx) are switching all three WDM probe signals in the NOLM simultaneously. Inset: Eye diagrams at different positions in the system (oscilloscope bandwidth: 70 GHz). This bandwidth limitation impairs the eye diagram of the 130 Gbit/s OTDM signal. MLL – mode locked laser, PC – polarization controller. (b) Spectral traces of the demultiplexed switched signal before (solid trace) and after (dashed traces) the WDM filter.

The experimental set-up of the OTDM to WDM converter is shown in Fig. 5.8(a). The WDM signals are generated using three CW lasers at wavelengths $\lambda_1 = 1547.8$ nm, $\lambda_2 = 1552.5$ nm and $\lambda_3 = 1557.4$ nm, respectively, followed by a single commercially available EAM. Due to the wavelength dependence of the particular EAM used in this experiment and the resulting low output power levels, different pulse widths, extinction ratios, and powers are obtained for the various WDM channels (see corresponding eye-diagrams in Fig. 5.8(a)). The FWHM (Full Width at Half Maximum) of pulses in different WDM channels vary from 5.5 ps to 6.5 ps. Each WDM signal has an individual polarization controller (PC) to maximize the switching efficiency in the NOLM. The WDM signals are subsequently coupled together, amplified

up to ~ 20 dBm average optical power and launched into the NOLM. Two optical delay lines (DL) are included into two arms to temporally align the WDM pulses to the OTDM signal.

The OTDM signal is generated by a tunable mode locked laser (MLL) with a repetition rate of 43 GHz, which operates at $\lambda_0 = 1539.4$ nm and emits pulses of 2.5 ps FWHM. It is modulated by a $2^7 - 1$ pseudorandom bit sequence (PRBS) using a Lithium Niobate modulator, multiplexed up to 130 Gbit/s (see corresponding eye-diagram in Fig. 5.8(a)) and amplified up to ~ 23 dBm average optical power before entering the NOLM via a 3-dB coupler. An optical DL is included for temporal alignment with the WDM pulses, and a Gaussian shaped 5 nm filter was used after the EDFA to suppress spontaneous emission.

The specially designed HNLF (Furukawa Electric) used in the loop had a length of 310 m, a dispersion of $C = -0.31$ ps/nm/km, a dispersion slope of $D = 0.0031$ ps/nm²/km, a nonlinear coefficient of $\gamma = 20$ W/km and a loss parameter of $\alpha_{\text{dB}} = 1.21$ dB/km. These fiber characteristics gave a maximum walk-off time between the OTDM and the various WDM signals of 1.8 ps only. The WDM signals switched by the NOLM were then separated by a WDM demultiplexer filter. To demonstrate multichannel operation, different outputs of the WDM demultiplexer were individually assessed using a single receiver with optical preamplification, which comprised a variable attenuator, an Erbium doped fiber amplifier (EDFA), a ~ 1 nm filter and a 40 GHz receiver. For details on the receiver setup see Section 3.3.2.

5.3.4 Results and Discussion

Fig. 5.8 (b) shows the spectral traces at the output port of the NOLM, before (solid trace) and after (dashed traces) the WDM filter, while the insets in Fig. 5.8(a) shows the eye diagrams of the three simultaneously switched WDM channels. A high extinction ratio of the switched eye was guaranteed by a controlled amount of optical bias (i.e. phase difference) between signals propagating through the loop in opposite directions. This optical bias was generated by a polarization controller inside the NOLM [43].

Bit-error rate (BER) measurements and receiver sensitivity for each WDM channel are shown in Fig. 5.9(a) and Fig. 5.9(b) in the presence/absence of the adjacent WDM channels, respectively, to assess the crosstalk between them. Error free operation ($\text{BER} \leq 10^{-9}$) is achieved for all WDM channels with power penalties (p_i) of only $p_1 \approx 0.5$ dB, $p_2 \approx 1.7$ dB and $p_3 \approx 3.5$ dB for Channel 3, 2 and 1, respectively.

We believe that the different performance achieved for the various WDM channels, with Channel 1 being the worst, reflects the incomplete power equalization prior to entering the EDFA at the input to the NOLM. This causes the various WDM pulse probes to have different average/peak power levels as can be seen in Fig. 5.8(b), and consequently different optical signal to noise ratios. Furthermore, Channel 1 is spectrally closest to the TDM signal resulting in a further degradation of its optical signal-to-noise ratio (OSNR). For a larger received power the error ratio saturates at around 10^{-10} such that even when further increasing the power the error ratio does not improve, thus an error floor develops. This is due to the fact that the OSNR was degraded prior to entering the receiver (ref to Appendix on BER measurements). However, the power penalties can be improved by power equalization of the three WDM pulse probes prior to entering the EDFA at the input to the NOLM.

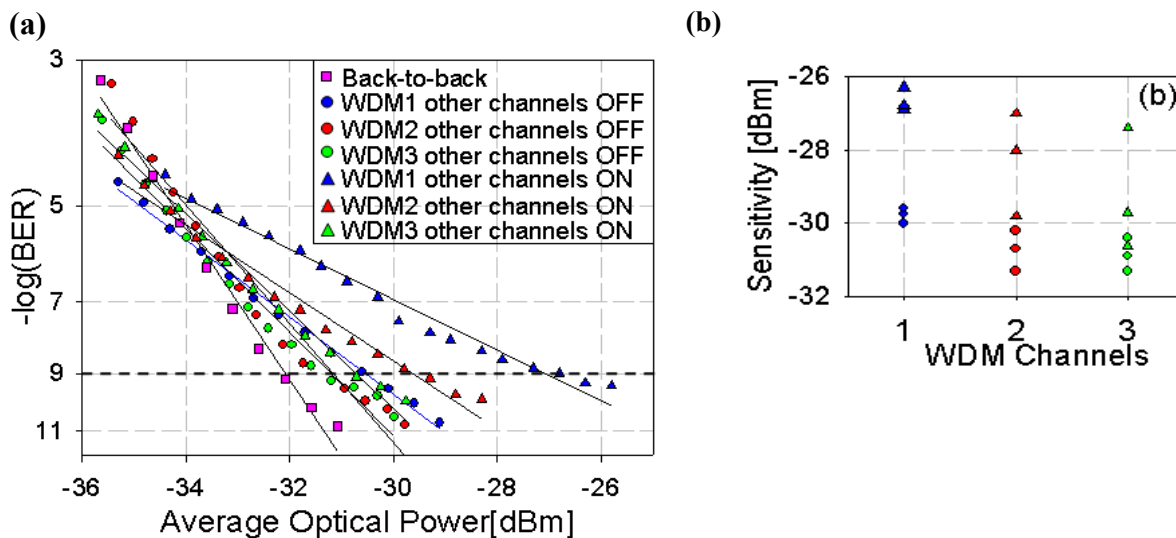


Fig. 5.9. (a) BER measurements of each WDM channel when the other WDM channels are absent (circles) and present (triangles), respectively, showing no error floor. The 43 Gbit/s back-to-back measurement is also reported (rectangles). (b) Receiver sensitivity for all the WDM channels for error free operation when the other WDM channels are switched off (circles) and on (triangles), respectively.

5.4 Conclusions

We have successfully demonstrated two all-optical techniques that convert a 130 Gbit/s OTDM signal simultaneously to a 3×43 Gbit/s WDM signal.

The first technique is based on SPM in a HNLF and subsequent offset filtering. Error free operation is achieved for all the WDM channels with a maximum power penalty of only 2.2 dB compared to the back-to-back signal.

The second scheme is based on broadband XPM in a single NOLM. Using a specially designed low dispersion and low dispersion slope HNLF as a nonlinear element, a low walk-off time among the signals and thus a broadband gate was achieved. BER measurements show error free operation for all the three WDM channels with a maximum power penalty of 3.5 dB and no error floor.

While good performance is achieved with both configurations, the two schemes present different advantages and disadvantages. The first scheme has the advantage of polarization insensitivity, but depends crucially on a short switching window in the EAM, which is used as the temporal gate in the switch. Furthermore, the scheme does not enable flexibility in the wavelength allocation. In contrast to that, the second scheme enables full flexibility in selecting the output WDM channel wavelengths and, since it exploits ultra-fast Kerr-based effects, it is characterized by a fast and temporally narrow switching window. On the other hand, this configuration is polarization sensitive, since it is based on XPM in a HNLF, and the corresponding experimental set-up is more complex than the SPM-based solution.

For the system demonstration discussed in Chapter 8, the first approach is chosen because of the simpler setup, ease of operation and better long-term stability.

6 Optical Clock Recovery

Two different OTDM-to-WDM conversion subsystems are proposed in this work, one based on SPM and subsequent optical gating and the other one based on XPM in a NOLM (see Section 5.2 and Section 5.3, respectively). Both techniques make use of electro-absorption modulators (EAMs) as fast electro-optic switches, one for pulse carving and one for optical gating. These optical switches need to be driven with a sinusoidal electrical clock signal matched to the OTDM tributary bit rate ($f_{\text{clk}} = 42.7$ GHz) and in phase with the incoming OTDM signal. It is the task of a clock recovery to extract this clock signal as a subharmonic of the 128.1 Gbit/s TDM signal. The clock recovery needs coping timing jitter and wander that are introduced during transmission. It should stay locked at all times, even during guard bands (OTDM channel hopping would lead to error bursts).

The implementation of the clock recovery used in this work is based on an opto-electronic oscillator. These oscillators have been used to implement clock recoveries of two types of injection locked frequency dividers: injection locked oscillators [44] and regenerative frequency dividers [45]. Implementations to recover a 40 GHz clock from a 160 Gbit/s RZ-OOK OTDM signal have also been shown following both principles [46][47]. In those implementations, locking was achieved only by deliberately increasing the power of one timeslot in the OTDM multiplexer and locking on the residual 40 GHz component of the OTDM signal.

The clock recovery presented in this thesis makes use of harmonics of the local clock signal generated by the nonlinear transfer function of an EAM. This implementation based on an optoelectronic oscillator does not depend on misalignment of the OTDM multiplexer. Excellent phase noise and jitter performance is achieved. Note that with this clock recovery implementation the problem of OTDM channel recognition remains. Techniques which mark one OTDM channel offer possible solutions to this problem. Ideally, this marking or additional coding of one channel should not affect the BER performance of this channel. For amplitude modulation one could think of an additional phase coding of one channel which has been proposed and realized in, e.g. [48],[49]. However, when traversing any of the all-optical OOK 2R regenerators proposed in Chapter 7, the phase coding is lost. In the framework of this thesis no channel recognition was implemented. For any measurement the consistency of all three OTDM channels was verified only relative to a randomly chosen channel.

This chapter is organized as follows: The fundamentals of optoelectronic oscillators are reviewed in Subsection 6.1. The chosen implementation based on an optoelectronic oscillator is presented in Subsection 6.2 while experimental results (loop bandwidth, jitter and long-term stability) are given in Subsection 6.3. Finally, in subsection 6.4, we compare the experimental results to data found in the literature.

6.1 Fundamentals

6.1.1 Oscillating Frequency Dividers

In recent years, optically injection locked oscillators have attracted great interest because of their possible use in future optical communication systems and opto-electronic clock recoveries [44],[47],[46]. The locking bandwidth is one of the major design parameters in these types of injection-locked oscillators. The first locking bandwidth equation for electrically injection-locked oscillators was developed by Adler [50]. This model has been used widely to calculate the locking bandwidth of optically injection-locked oscillators [51],[52].

In this section, we first briefly discuss the case of a free-running oscillator, followed by a review of the locking bandwidth equation introduced by Adler. The model and its assumptions are described. Adler's approach is then used to gain insight into the locking mechanism and in order to understand what determines the locking range.

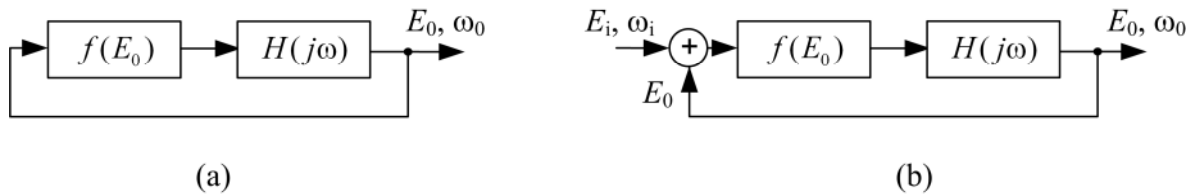


Fig. 6.1. General model of an LC oscillator as a positive feedback loop. (a) Free running oscillator with output amplitude E_0 and natural frequency ω_0 . (b) Oscillator with injected harmonic signal with amplitude E_i and frequency ω_i before locking. All nonlinearities are modelled as a nonlinear block f followed by a frequency selective block with the transfer function $H(j\omega)$.

Free-Running Oscillator

An LC oscillator can be modelled as a nonlinear block f , followed by a frequency selective block (e.g. an RLC filter) with the transfer function $H(j\omega)$, in a positive feedback loop as shown in Fig. 6.1a. Note that the signals in the oscillator propagate clockwise unidirectional. The nonlinear block models all the nonlinearities in the oscillator, including the amplitude-limiting mechanisms. All nonlinearities are assumed to be of the instantaneous type. Let us assume that the oscillator operates at a natural frequency ω_0 and that the filter suppresses frequencies far from ω_0 . Let us call the steady-state output voltage amplitude of the oscillator E_0 . To have a steady-state oscillation, the loop gain need be one. The phase condition requires that the phase shift introduced in the loop at $\omega = \omega_0$ should be an integer multiple of 2π .

Injection-Locked Oscillator: Adler's Model

With an additional external forcing signal coupled to the oscillator, the same model can be used to model an injection locked oscillator (see Fig. 6.1b).

When the coupling is strong enough and the frequencies close enough, the second oscillator can capture the frequency of the first oscillator, causing the second oscillator to have essentially identical frequency as the first. In this section we will address a simplified case of coupling: a unidirectional coupling, i.e. one system forces another. For simplicity we assume that

the injected signal can be described by a sine with the voltage amplitude E_i and frequency ω_i . This approximation works well when the influence of the second system on the forcing system is negligibly small.

Fig. 6.2a shows the circuit model used by Adler [50]. A parallel RLC resonator was used for the resonator model, where R is a resistance, giving the resonator loss. A tube transistor was used as the active device of the oscillator. E_g is the amplitude of the total voltage generated across the load after the application of the external signal.

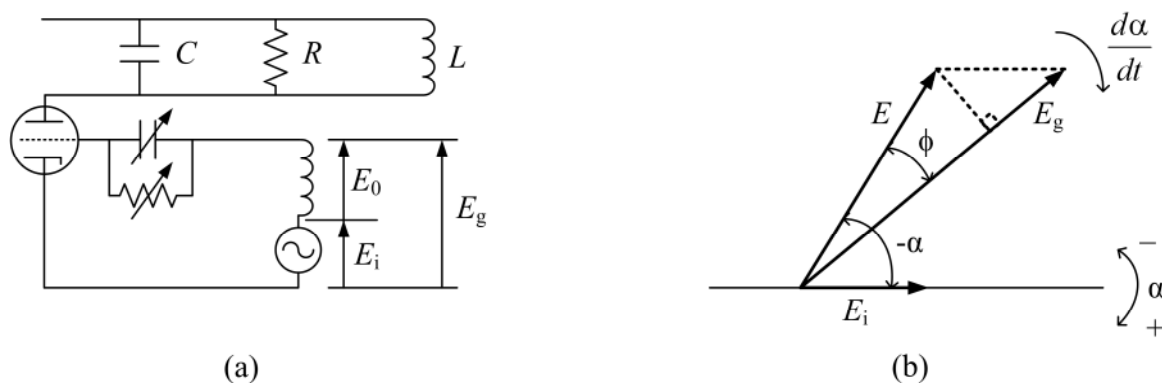


Fig. 6.2. Adler's injection-locking oscillator circuit (modified from [50]). (b) Vector diagram of injection-locked oscillator.

A vector diagram of the signals within an injection-locked oscillator was presented by Adler, see Fig. 6.2b. The oscillator instantaneous output is represented by the vector E rotating clockwise with an angular frequency of ω (the instantaneous output frequency after injection locking) while the injection signal vector of amplitude E_i , rotates clockwise with an angular frequency of ω_i (the injection signal frequency). The instantaneous phase difference between these vectors is α . The phase difference ϕ between the instantaneous output frequency and the total voltage (of amplitude E_g) generated across the load is given as [50]

$$\phi = -\frac{E_i}{E} \sin \alpha. \quad (6.1)$$

ϕ can also be written as [50]

$$\begin{aligned} \phi &= \frac{d\phi}{d\omega} (\omega - \omega_0) \\ &= \frac{d\phi}{d\omega} [(\omega - \omega_i) - (\omega_0 - \omega_i)] \\ &= \frac{d\phi}{d\omega} [\Delta\omega - \Delta\omega_0], \end{aligned} \quad (6.2)$$

where ω_0 is the oscillator free-running output frequency, $\Delta\omega = \frac{d\alpha}{dt} = \omega - \omega_i$ is the instantaneous beat frequency, and $\Delta\omega_0 = \omega_0 - \omega_i$ is the undisturbed beat frequency.

Substituting Eq. (6.2) into Eq. (6.1), we obtain [50]

$$-\frac{E_i}{E} \sin \alpha = \frac{d\phi}{d\omega} \left[\frac{d\alpha}{dt} - \Delta\omega_0 \right]. \quad (6.3)$$

For a single tuned resonator, the quality factor is [50]

$$Q = \frac{\omega_0}{2} \frac{d\phi}{d\omega}. \quad (6.4)$$

Substituting Eq. (6.4) into Eq. (6.3), we obtain [50]

$$-\frac{E_i}{E} \sin \alpha = \frac{2Q}{\omega_0} \left[\frac{d\alpha}{dt} - \Delta\omega_0 \right]. \quad (6.5)$$

Adler also recognized that Eq. (6.5) could serve as a model describing the motion of a pendulum suspended in a viscous fluid inside a rotating container, see [50].

Adler obtained injection locking behaviour and the locking range for LC oscillators based on Eq. (6.5). When the oscillator is locked, the phase difference $d\alpha/dt$ becomes constant and Eq. (6.5) gives

$$\frac{E_i}{E} \sin \alpha = \frac{2Q}{\omega_0} \Delta\omega_0. \quad (6.6)$$

And since $|\sin(x)| \leq 1$, we obtain

$$-\frac{E_i}{E} \frac{1}{2Q} \leq \frac{\Delta\omega_0}{\omega_0} \leq \frac{E_i}{E} \frac{1}{2Q}. \quad (6.7)$$

This immediately gives the locking range ω_l as

$$\omega_l = 2|\Delta\omega_0|_{\max} = \frac{\omega_0}{Q} \frac{E_i}{E}. \quad (6.8)$$

As Eq. (6.8) suggests, the locking range can be increased by either decreasing Q or increasing the incident amplitude E_i . Fig. 6.3 schematically illustrates the locking range.

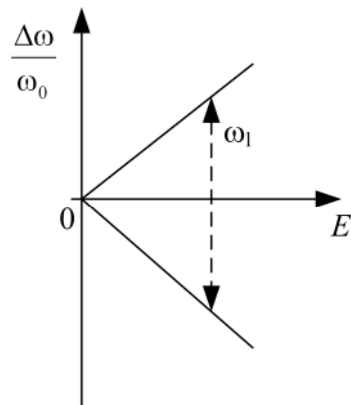


Fig. 6.3. Schematic illustration of locking range ω_l . For a fixed Q the locking range can be increased by increasing E_i .

Approximation for the Pull-In Process

Turning now to the transient solution of the differential Eq. (6.3), we examine first the case of $\Delta\omega_0 = 0$. This means that the free-running frequency equals that of the impressed signal and that locking will eventually occur for any combination of voltages and circuit constants. The equation

$$\frac{d\alpha}{dt} = -\frac{E_i}{E} \frac{d\omega}{d\phi} \sin \alpha \quad (6.9)$$

shows what happens when the external signal E_i is suddenly switched on with an initial lag α_i with respect to the phase of the free-running oscillator. Eq. (6.9) is quite similar to

$$\frac{d\alpha}{dt} = -\frac{E_i}{E} \frac{d\omega}{d\phi} \alpha \quad (6.10)$$

and can actually be approximated in this form when α is small.

Eq. (6.10) has the solution

$$\alpha = \alpha_i e^{-\frac{E_i}{E} \frac{d\omega}{d\phi} t} \quad (6.11)$$

showing that the oscillator phase decreases and converges towards the phase of the impressed signal, first approximately, and later accurately as a capacitor discharge into a resistor. The speed of this process is proportional to the ratio of impressed voltage to oscillator voltage and to the bandwidth of the tuned circuit.

If the free-running frequency is not equal to that of the impressed signal, but close enough to permit locking for a given combination of constants according to Eq. (6.8), the manner in which the steady state is reached must still resemble a capacitor discharge. Note that the final value α_∞ is always approached from one side in an aperiodic fashion.

Phase locking for other frequencies

Generally, synchronization is observed for high-order resonances $n\omega_i = m\omega_0$ (n, m being integers) as well. The synchronous regime at the rational multiple of the forcing frequency of the injected signal, $\omega = (n/m)\omega_i$, as well as phase locking $m\phi = n\omega_i t + const$. The overall picture can be shown in the (ω, E_i) -plane (as an extension in Fig. 6.3): there exists a family of triangular-shaped synchronization regions touching the ω -axis at the rationales of the free-running oscillation frequency $(m/n)\omega_0$.

We will make use of this feature of injection locked oscillators in the following sections and design and demonstrate an opto-electronic oscillator working as a clock recovery, demonstrating 43 GHz clock recovery from a 130 Gbit/s input signal.

6.1.2 The Injection Locked Oscillator as a Clock Recovery

A return-to-zero on-off-keying (RZ-OOK) signal has a main spectral component at the bitrate of the signal. By using an Adler type oscillator, the signal is mixed with the local oscillator and harmonics are generated by the nonlinearity. Due to the fact that the frequency of this spectral component is a multiple of the clock frequency that is to be recovered, the mixing

with the local oscillation will generate a spectral component at the frequency of the local oscillation. If the bandwidth of the bandpass filter in the injection locked oscillator is sufficiently narrow, it strips off the modulation from the data signal. For this, the incoming frequency or its submultiple has to be close to the center of the pass band of the oscillator [50]. In the state of synchronization, the spectrum of the oscillator converges towards the spectrum of the incoming signal within the limits imposed by the pass band of the oscillator. Within this frequency range, phase disturbances of the incoming signal are reproduced at the output of the oscillator [50]. The injection locked oscillator will therefore follow slow drifts of the incoming clock frequency as well as low-frequency jitter. High-frequency jitter will be suppressed because of the limited bandwidth of the oscillator. However, the loop bandwidth is dependent on the power of the injected signal as is the locking range of the oscillator (see [53], page 1020).

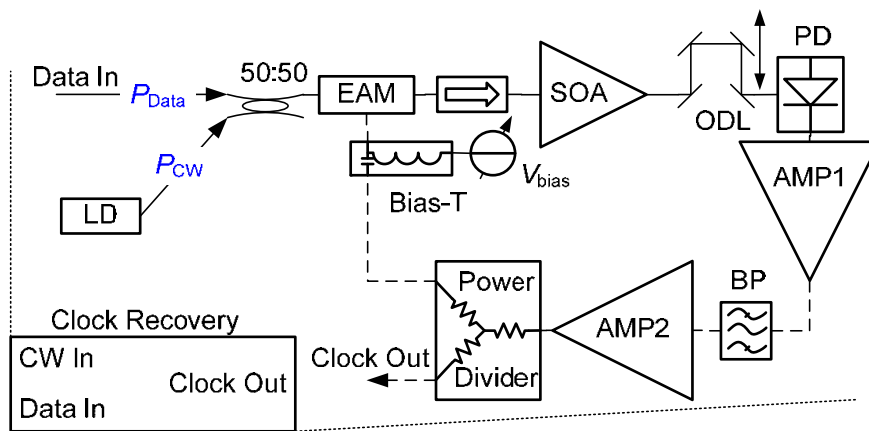


Fig. 6.4. Implementation of the optoelectronic oscillator used for the clock recovery. Data signal and a CW wavelength (LD) are input to an electro-absorption modulator (EAM). A semiconductor optical amplifier (SOA) compensates for losses in the oscillator which length can be adjusted by an optical delay line (ODL). The signal is then detected by a photodetector (PD), amplified by a high-gain amplifier (AMP1) and the fundamental mode is selected by a high Q electrical bandpass filter (BP). This fundamental mode is amplified by a limiting amplifier (AMP2) and serves as the drive signal for the EAM, closing the feedback loop. In later drawings, the clock recovery will be represented by the symbol on the lower left. P_{Data} and P_{CW} denote input power levels of the data signal and CW laser, respectively.

6.2 Implementation of the Clock Recovery

The setup of the optoelectronic oscillator is shown in Fig. 6.4. The optoelectronic oscillator comprises of a continuous-wave laser (LD), electro-absorption modulator (EAM), semiconductor optical amplifier (SOA), variable optical delay line (ODL), photodetector (PD), electrical amplifiers (AMP1, AMP2) and a high-Q electrical bandpass (BP) filter. The output light of the LD is input to the EAM via a 50:50 coupler, amplified by the SOA and converted to an electrical signal by the PD. The isolator prevents the amplified spontaneous emission (ASE) noise of the semiconductor optical amplifier (SOA) from influencing the EAM. The optical delay line (ODL) is used as a phase shifter to tune the length of the optoelectronic oscillator. The electrical signal at the PD output is then amplified in a narrow band amplifier (AMP1) and afterwards bandpass filtered to recover the spectral components that exist near the funda-

mental frequency of the optoelectronic oscillator. The signal is then amplified in a limiting amplifier (AMP2) and drives the EAM.

In the absence of injected data streams (only CW laser LD), the OEO supports self-sustained oscillation at its fundamental frequency determined by the BP filter and transit time of the feedback loop. The OEO is designed to oscillate around 42.7 GHz. The oscillation frequency can be tuned around this value by adjusting the ODL.

With data stream injection via the 50:50 coupler at the input, the signal and the CW light are sent to the EAM to multiply the incoming data signal with the local clock and its harmonics, which are generated by the nonlinear transfer function of the EAM. Recovered electrical clocks are extracted just after AMP2 using an RF power divider.

6.2.1 Choice of the Critical Components

The Electrical Bandpass Filter

The electrical bandpass filter is a crucial component in the optoelectronic oscillator. The filter is required to suppress all but the desired longitudinal mode in the ring cavity of the oscillator. It therefore defines the minimal allowed mode spacing for single mode operation. This maximum length corresponds to a limit for the length of the oscillator. The filter used in this work is a waveguide filter consisting of a half wavelength resonant cavity coupled by capacitive irises. A filter with a centre frequency of $f_C = 42.7$ GHz and a 3-dB bandwidth of $\Delta f = 40$ MHz is used. This corresponds to a $Q_{filter} = f_C / \Delta f \approx 1068$.

Electro-Absorption Modulator

To test if the selected modulator can be used for this setup, it is necessary to study the gating window of the modulator and the harmonics generated due to the transfer function. In addition, the setup is required to be polarisation insensitive. Due to this, conventional Mach-Zehnder modulators cannot be used for this implementation. Electro-absorption modulators (EAMs) are not completely polarisation insensitive but some modulation is achieved for any arbitrary polarisation.

In this implementation a sampling window generator EAM was chosen that generates short sampling windows suitable for demultiplexing. In addition to this, a short gating window also corresponds to a higher number of harmonics that are generated by the nonlinear transfer function of the EAM. It has been driven with a peak-to-peak voltage of $V_{pp} = 4.0$ V and with a reverse bias of $V_{bias} = 2.0$ V throughout the following measurements for maximum harmonics generation.

Optical Amplifier

In addition to the modulator an optical amplifier is required. This is due to the fact that the maximum average optical input power into the EAM is 10 dBm and that it has an insertion loss in excess of 20 dB if modulation is applied. Therefore, the output power of the modulator is too low to be directly detected with a 40 GHz photodiode and it is therefore necessary to amplify the signal prior to detection. Due to the length constraints of the oscillator a fibre amplifier cannot be used. It would also introduce additional vulnerability to temperature fluctua-

tions of the setup that could only be counteracted by sophisticated temperature stabilization or by constant adjustment of the loop length. For these reasons a packaged bulk semiconductor optical amplifier is used in this setup with a noise figure $F = 10$ dB, a 3 dB gain spectrum from 1480 nm to 1560 nm, and a small signal gain $G = 15$ dB.

Photodiode

The photodiode (PD) is not that critical due to the fact that a lower responsivity of the photodiode can be compensated by higher gain of the amplifiers in the loop. The PD used has 3-dB bandwidth of $BW = 45$ GHz.

First Electrical Amplifier

The first electrical amplifier is chosen such that it has a large gain at the target frequency to deliver sufficient input power to the high-Q filter. It is necessary to drive the second amplifier into saturation independently of the operating conditions of the setup. This leads to a stable clock output power as well as stable operating conditions for the EAM. The narrowband clock amplifier used in the setup has a 3-dB gain bandwidth of $BW = 4$ GHz around 42.7 GHz, a gain of $G = 38.9$ dB and a 1-dB gain compression input power of $P_{-1\text{dB}} = 29.3$ dBm.

Second Electrical Amplifier

The specifications of the second amplifier are more critical. It defines the input power to the electro absorption modulator which is quite sensitive to its operating conditions. It is advantageous if this amplifier operates in saturation (thus acting as a limiting amplifier) independently of the operating conditions of the oscillator. It is also advantageous if this amplifier delivers enough output power to simultaneously drive the EAM and the output of the clock recovery. In this case the output amplitude of the clock recovery stays constant even if the input power to the clock recovery changes. The broadband amplifier used in the setup has a 3-dB bandwidth of $BW = 46$ GHz, a gain of $G = 27$ dB, a noise figure $F = 4.5$ dB, and a saturation output power $P_{\text{sat}} = 24.1$ dBm.

6.2.2 Locking of the Optoelectronic Oscillator

For locking of the OEO, the mixing of the incoming data signal with the local oscillation and its harmonics must generate another spectral component in the pass band of the oscillator in addition to the component that is generated by the free running local oscillation alone.

For any values m or n ($m, n = 1, 2, \dots$) other than $m = 1$ and $n = 0$, locking of the oscillator can be achieved if

$$|m\omega_o \pm n\omega_l| = \omega_o. \quad (6.12)$$

In the implementation studied, the main spectral component of the data signal is 128.1 GHz and the local oscillation is at 42.7 GHz, leading to a constant factor of 3 between ω_o and ω_l ($3 \cdot \omega_o = \omega_l$).

This leads to

$$\begin{aligned}
 \omega_o &= |m\omega_o \pm n\omega_I| \stackrel{3\cdot\omega_o=\omega_I}{=} |m\omega_o \pm n\cdot 3\cdot\omega_o| \\
 &= \omega_o \cdot |m \pm 3\cdot n| \\
 &\Rightarrow |m \pm 3\cdot n| = 1
 \end{aligned} \tag{6.13}$$

Equation (6.13) is now analyzed for its different solutions leading to

$$\begin{aligned}
 |m+3\cdot n| = 1 &\xleftarrow{m+3\cdot n} |m \pm 3\cdot n| = 1 \xrightarrow{m-3\cdot n} |m-3\cdot n| = 1 \\
 m+3\cdot n > 0 \downarrow & & m-3\cdot n > 0 \downarrow & & m-3\cdot n < 0 \downarrow \\
 m+3\cdot n = 1 & & m-3\cdot n = 1 & & 3\cdot n - m = 1 \\
 \Rightarrow \underbrace{n=0, m=1}_{\text{Free running oscillator}} & & \underbrace{m=3\cdot n+1}_{\text{Injection locked oscillator}} & & \underbrace{m=3\cdot n-1}_{\text{Injection locked oscillator}}
 \end{aligned} \tag{6.14}$$

The solution consists of three possible cases. First, if both factors m and n are summed up, the absolute value will always be positive. In this case only one solution is possible: Due to the fact that n is multiplied by a factor of three there is only the solution $m = 1$ and $n = 0$. This solution corresponds to the free running oscillator. Second, if the two components are subtracted, two solutions are possible, $m = 3\cdot n + 1$ and $m = 3\cdot n - 1$ for $n = 1, 2, 3, \dots$. The first possible combinations of m and n are shown in Table 6.1.

	Possible solutions for m		$3\cdot n + 1$ th harmonic of f_o	$3\cdot n - 1$ th harmonic of f_o	n th harmonic of f_I
	$m = 3\cdot n + 1$	$m = 3\cdot n - 1$			
$n = 1$	4	2	170.8 GHz	85.4 GHz	128.1
$n = 2$	7	5	298.9 GHz	213.5 GHz	256.2
$n = 3$	10	8	427.0 GHz	341.6 GHz	384.3

Table 6.1. Combination of harmonics that can lead to injection locking in the optoelectronic oscillator in the implementation with $f_o = 42.7$ GHz and $f_I = 128.1$ GHz.

6.3 Results

In this section, stability, locking and the quality of the recovered clock of the optoelectronic oscillator will be presented. The final implementation of the optoelectronic oscillator is shown in Fig. 6.4. It was used for the measurements shown in this section if not stated otherwise.

6.3.1 Free Running Oscillator

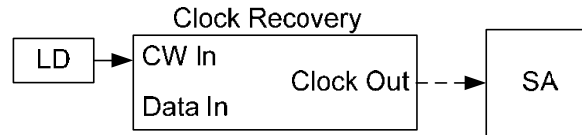


Fig. 6.5. Setup for the experimental study of the free running oscillator. It consists of a CW laser diode (LD), the clock recovery and a radio frequency spectrum analyzer (SA) to measure the electrical spectrum at the output of the clock recovery.

Fig. 6.5 shows the experimental setup used to study the free running opto-electronic oscillator. The RF spectrum of the free running oscillator is shown in Fig. 6.6(a). The main spectral component of the spectrum is one peak at 42.7 GHz. This is the oscillating mode in the loop. Next to it are the non-oscillating sidemodes. They are nearly 40 dB lower in power.

A series of measurements was taken to study the temporal stability of the optoelectronic oscillator. These measurements were taken using Erbium doped fibre amplifiers instead of the SOA used in the final setup. They involved taking measurements of the peak frequency of the optoelectronic oscillator over several hours to study the drift of the setup. The results are shown in Fig. 6.6(b).

Jitter measurements of the free running oscillator were not taken due to the lack of required equipment. The drift of the setup was too fast to measure the noise using direct sideband measurement techniques. To measure the jitter performance of the free running oscillator, an additional mixer would be required to measure this jitter in an autocorrelation setup that would compensate for the drift of the oscillator.

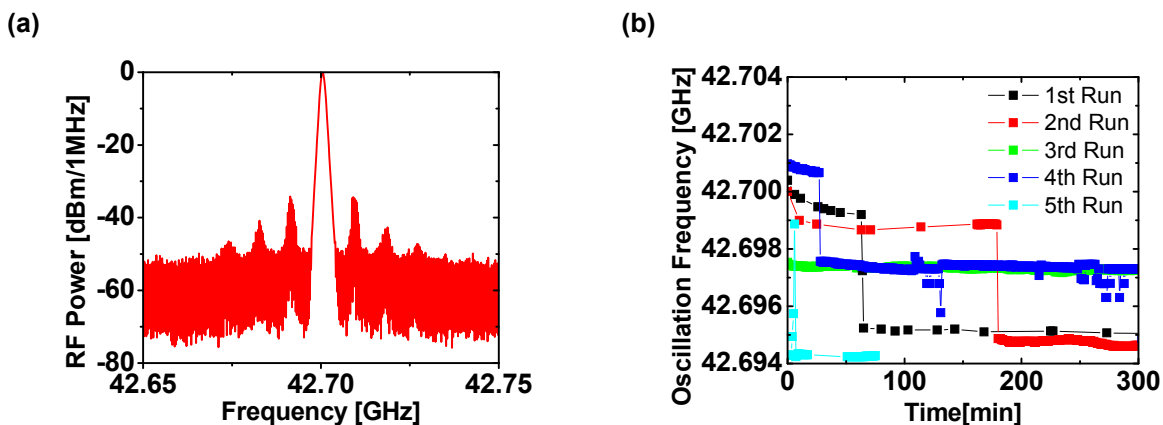


Fig. 6.6. (a) RF spectrum of the free running oscillator. (b) Five long-term stability measurements of output clock signal of the oscillator using two EDFA stages instead of the SOA.

Mode Spacing and Round Trip Time

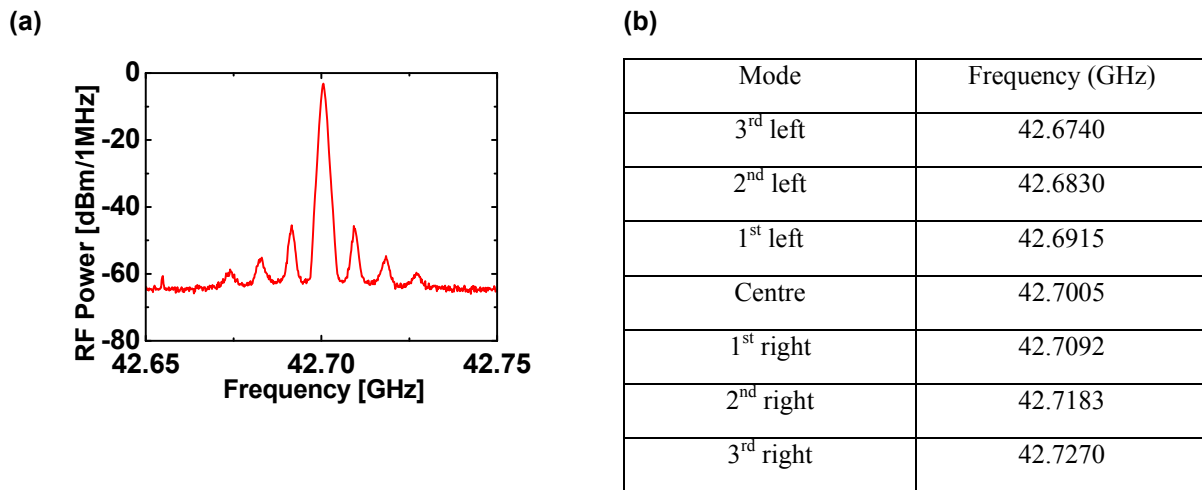


Fig. 6.7. (a) RF Spectrum of the free running oscillator output averaged over one hundred measurements. (b) Frequencies of the oscillating and non-oscillating modes in the optoelectronic oscillator extracted from (a).

The round trip time T_d of the oscillator can be calculated from the mode spacing in the optoelectronic oscillator. T_d can be derived with Δf being the spacing of neighbouring modes

$$T_d = \frac{1}{\Delta f}. \quad (6.15)$$

The mode frequencies have been read from the data plotted in Fig. 6.7(a) and are shown in the table in Fig. 6.7(b). The non-excited modes of the oscillator can be seen besides the main oscillating mode. The fundamental frequency of the loop can be calculated from any pair of values shown in Fig. 6.7(b). By averaging all calculated values the fundamental frequency of the oscillator is calculated to be $F_0 = \Delta f = 8.832$ MHz. This value is also called free spectral range. Using Eq. (6.15), the round trip time is calculated to be $T_d = 113.2$ ns. It is also possible to calculate the order of the oscillating mode M in the optoelectronic oscillator:

$$M = \frac{f_o}{F_0} = \frac{42.7005 \text{ GHz}}{8.832 \text{ MHz}} = 4835 \quad (6.16)$$

Note that for the relation $\Delta f = \frac{c}{n_g L}$ the approximate relation $\Delta f \approx \frac{c}{nL}$ is substituted, where the refractive index is assumed frequency-independent.

Bandpass Characteristics of the Optoelectronic Oscillator

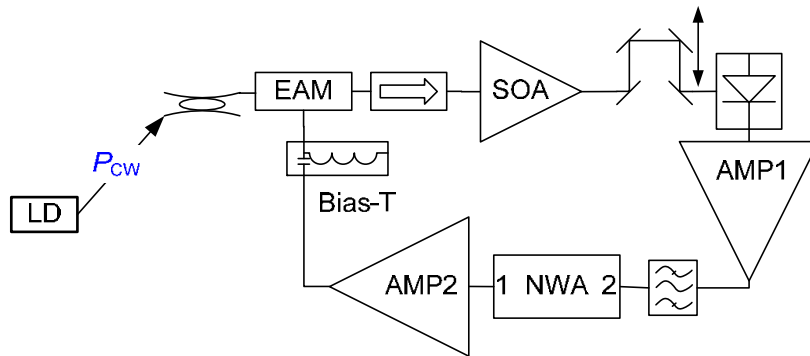


Fig. 6.8. Experimental setup to study the bandpass characteristic of the opto-electronic oscillator. The loop is opened after the bandpass filter and a network analyzer (NWA) is placed in the loop.

To measure the bandpass characteristics of the loop, the loop is opened and a network analyzer is connected to the setup as shown in Fig. 6.8. The Network analyzer is used to measure the scalar logarithmic gain, $g = 20 \log_{10} |S_{21}|$ in dB (scattering parameter S_{21} being the complex linear gain) of the loop (see Fig. 6.9(a)). It can be seen that the center frequency is not exactly at 42.70 GHz but is shifted to a slightly lower frequency. This is problematic if the mode spacing is not sufficiently large because the mode at 42.70 GHz might experience less gain in the loop than its neighbor. This can lead to mode hopping and loss of locking of the oscillator.

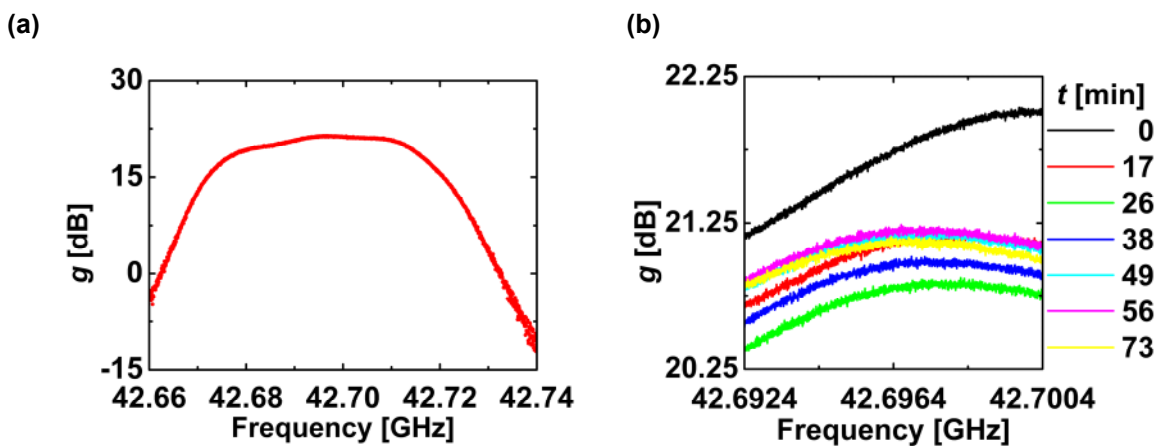


Fig. 6.9. Transmission characteristic of the opto-electronic oscillator determined by the high-Q bandpass filter as well as the frequency dependence of the other components inside the feedback loop: (a) Logarithmic gain g of the loop. (b) Zoom of (a) with g measured at different times after switching on the setup. A network analyzer is used for the measurements.

To find the reason for the offset of the peak from the centre frequency of the pass band of the electrical bandpass filter, the setup was tested again after a resting period of 15 hours. It was characterized within a span of 8 MHz centred on the peak frequency observed in the previous measurement shown in Fig. 6.9(a). Within one hour, several measurements were taken to study the changes of the peak frequency of the bandpass, see Fig. 6.9(b). The results show

that the peak frequency, after initially being at 42.70 GHz, drifts and stabilizes at a frequency about 4 MHz lower.

This behaviour can only be due to a warming up of the amplifiers or the band pass filter. However, due to the fact that the only part of the setup that has such a sharp band pass function is the band pass filter, the BPF is most likely the source of this temperature drift. This is also the limiting factor for the cavity length because the mode with the frequency that is to be recovered by the clock recovery, should be the one that is closest to the gain peak of the setup. The target frequency of the setup is 42.70 GHz. This frequency is nearly 4 MHz from the gain peak, so the mode spacing should ideally be larger than 8 MHz. Otherwise the oscillation is likely to start in a different mode, making it impossible to recover the clock at the required frequency of 42.70 GHz. This criterion is fulfilled, as the mode spacing has been calculated to be $\Delta f = 8.832$ MHz. However, the stability of the optoelectronic oscillator is likely to be improved if the mode spacing is increased by using a BPF filter with a higher Q.

6.3.2 Optoelectronic Oscillator as Clock Recovery

To study the performance of the clock recovery, a 128.1 Gbit/s data signal at a centre wavelength $\lambda_{\text{Data}} = 1555.5$ nm and with an input power $P_{\text{data}} = 5.0$ dBm together with a CW laser (LD) at $\lambda_{\text{CW}} = 1560.6$ nm and $P_{\text{CW}} = 3.0$ dBm are connected to its inputs. The 128.1 Gbit/s data signal is generated by an actively mode-locked fiber laser (MLL) with a repetition rate of 42.7 GHz. The MLL output pulses have a FWHM of 2.6 ps and are encoded by a pseudorandom bit sequence with a length of $2^7 - 1$. A two-stage fiber-optic OTDM multiplexer ensured an approximate PRBS pattern at the output (see also Section 3.4). The recovered clock signal is connected to the RF spectrum analyzer and to the trigger input of a sampling oscilloscope. The 128.1 Gbit/s data signal is detected by a 85 GHz photodiode which is connected to a 70 GHz sampling head in the DCA (Fig. 6.10).

By tuning the optical delay line in the clock recovery, the clock recovery locks to the incoming data signal. The clock is used to trigger the DCA to detect the incoming data signal. After phase locking the 128.1 Gbit/s OTDM signal can be observed on the oscilloscope. A screenshot is shown in Fig. 6.11(a).

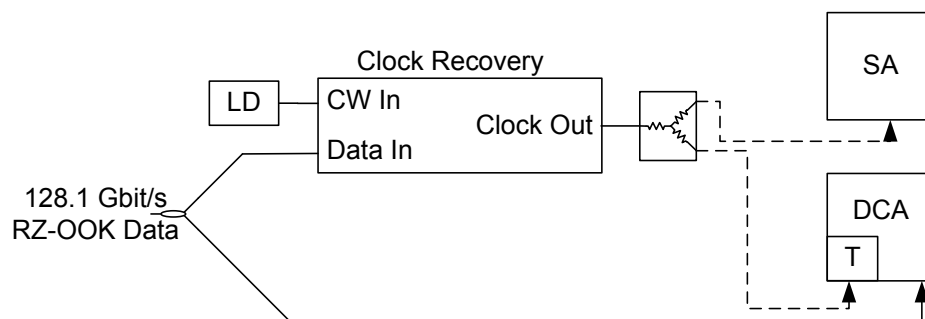


Fig. 6.10. Experimental setup for characterization of the clock recovery using a radio-frequency spectrum analyzer (SA) and a digital sampling oscilloscope (DCA). The clock recovery output is used to trigger the DCA. The 128.1 Gbit/s RZ-OOK signal is fed into an optical plug-in module of the DCA.

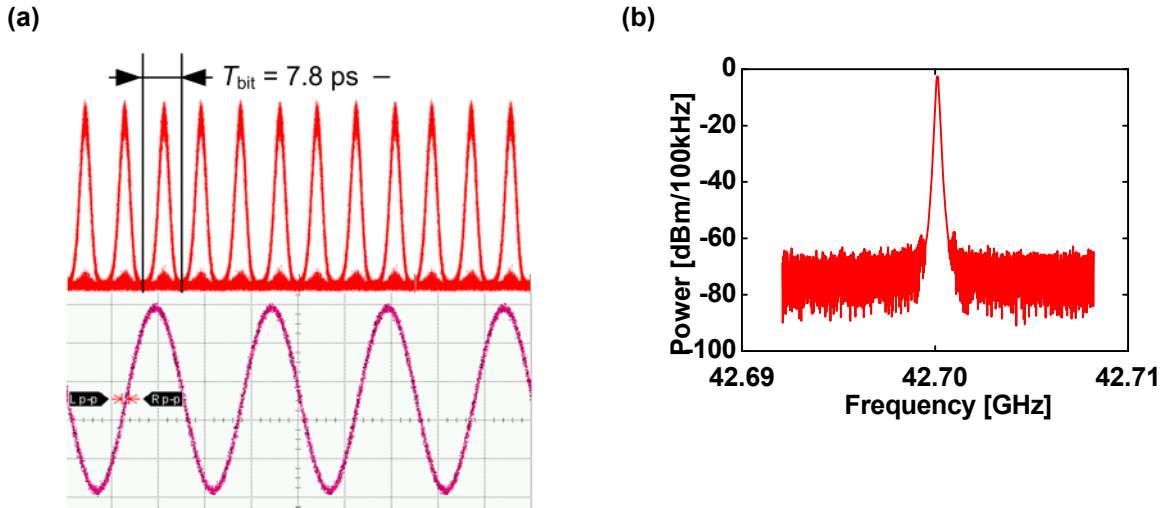


Fig. 6.11. (a) Eye diagram of a 128.1 Gbit/s 33% RZ-OOK OTDM data signal (measured with an ultra-fast optical sampling scope) and of the the recovered clock at 42.7 GHz. (b) RF spectrum of the clock recovery output when locked to the 128.1 Gbit/s data signal.

Fig. 6.11(b) shows the RF spectrum when the optoelectronic oscillator has locked to the incoming data signal. A single tone at 42.7 GHz is observed while the sidemodes that were observed for the free-running oscillator (Fig. 6.6(a) and Fig. 6.7(a)) are suppressed below the noise floor of the RF spectrum analyzer.

Jitter Performance

To study the jitter performance of the locked optoelectronic oscillator, single sideband phase noise measurements were taken. This method involves measuring the phase noise power spectral density $S_{\phi}(f)$ of one sideband of the clock tone at 42.7 GHz. The root mean square timing jitter σ_{RMS} can then be calculated by using the relationship

$$\sigma_{\text{RMS}} = \frac{1}{2\pi f_{\text{clk}}} \sqrt{\int_{f_l}^{f_h} S_{\phi}(f) df}, \quad [47] \quad (6.17)$$

where $f_{\text{clk}} = 42.7 \text{ GHz}$ represents the clock frequency and f_l and f_h denote the lower and upper limits of integration, respectively. For offsets higher than 10 MHz, the measurements were dominated by the noise floor of the instrument. In addition to the phase noise of the clock recovery output, the same measurement was taken for the output of the RF synthesizer.

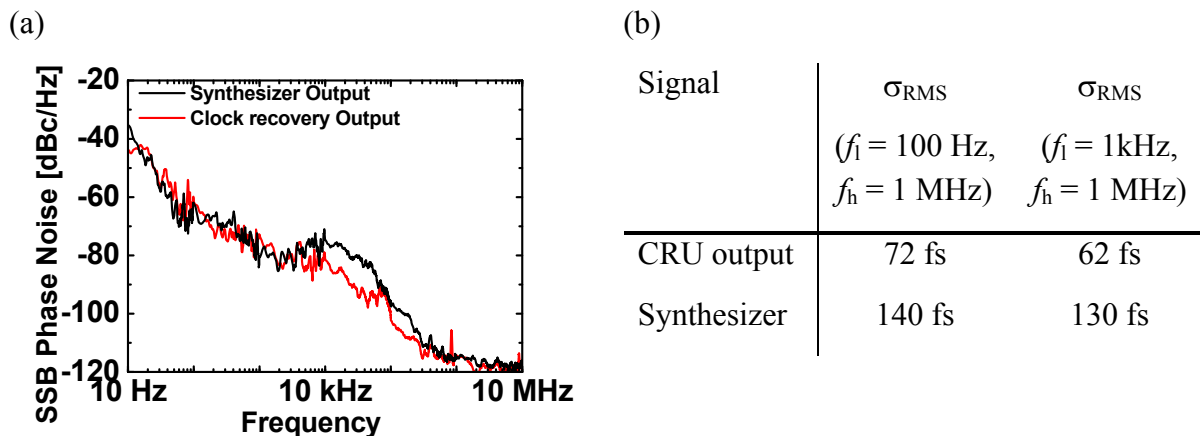


Fig. 6.12. (a) Single side band (SSB) phase noise of the synthesizer output and the locked clock recovery. (b) Jitter performance of the clock recovery unit (CRU) compared to the jitter of the synthesizer used to generate the 128.1 Gbit/s OTDM signal.

Looking at Fig. 6.12(a), it can be seen that the phase noise of the optoelectronic oscillator is lower than the noise of the synthesizer above an offset of approximately 4 kHz from the carrier. From this point on, the jitter performance of the recovered clock is dominated by the jitter performance of the free running oscillator due to its limited bandwidth [53]. This frequency is the equivalent of the loop bandwidth of a phase locked loop [53]. It is also observed that the first side mode near 10 MHz offset is suppressed by more than 110 dB. The resulting jitter values for different integration intervals are presented in the table inset in Fig. 6.12(b).

Locking Range

The locking range of the CRU can be estimated from the fact that the optical delay line in the oscillator could be turned by more than half a turn while the clock recovery stayed locked. With 24.5 turns corresponding to 100ps, half a turn corresponds to approximately 2 ps in time delay within which the phase shift introduced by the locking mechanism can compensate for the detuning of the local oscillator. By using the round trip time delay and the order of the mode that were found in section 6.3.1, the locking range can be calculated

$$\Delta f = f_{\max} - f_{\min} = \frac{m}{T_{\min}} - \frac{m}{T_{\max}} = \frac{m}{T - \frac{\Delta t}{2}} - \frac{m}{T + \frac{\Delta t}{2}} \quad (6.18)$$

This calculation leads to an approximate locking range of $\Delta f = 780$ kHz. However, remember that the locking range of the oscillator depends both on the amplitude of free running oscillator and the amplitude of the injected signal [53].

Characteristic Parameters

Table 6.2 shows the measured characteristic parameters of the clock recovery.

Parameter	Symbol	Value
Free spectral range	F_0	8.832 MHz
Mode order	M	4835
Round trip time (including filter)	T_d	113.2ns
Free Running Side Mode Suppression		> 40 dB
Locked Side Mode Suppression		> 100 dB
Estimated Loop Bandwidth		< 4 kHz
RMS Jitter (100 Hz - 1 MHz)	σ_{RMS}	72 fs
RMS Jitter (1 kHz - 1 MHz)	σ_{RMS}	62 fs
Locking Range ($P_{\text{data}} = 5 \text{ dBm}$)	Δf	780 kHz

Table 6.2. Characteristic parameters of the clock recovery.

The input wavelength range spans approximately from 1545 nm to 1565 nm. However, for different input wavelength the operating point of the EAM has to be optimized. The signal input power dynamic range is approximately $P_{\text{data}} = 5 \text{ dBm} \dots 10 \text{ dBm}$. We optimized the data input power for best operation for each experiment.

6.3.3 Scalability

The clock recovery has been demonstrated to work at 128.1 Gbit/s input bit rate. However, it will potentially also work at 42.7 Gbit/s and 170.8 Gbit/s. The clock recovery does not work for phase encoded input signals.

6.4 Comparison with Results from Literature

The jitter values are now compared to the values previously published. To compare different clock recovery setups with different incoming bitrates, a figure of merit is needed that takes into account that the same amount of timing jitter or phase noise of the recovered clock has a different impact depending on the signal bitrate. In this case the input-bitrate referred phase noise (IBRPN) is the figure of merit of choice, defined as

$$\text{IBRPN} = 360^\circ \cdot \text{Bitrate}_{\text{IN}} \cdot \sigma_{\text{RMS, OUT}} \quad (6.19)$$

The IBRPN takes into account that the timing jitter requirements of the clock recovery are inversely proportional to the bitrate of the incoming signal. The comparison is presented in Table 6.3. Comparing the jitter of the implementations that generate a 40 GHz clock, it can be seen that this implementation outperforms the other implementations of the optoelectronic oscillator. It has similar jitter performance compared to the 640 GHz to 40 GHz SOA based clock recovery and its IBRPN is significantly lower and therefore better than for any of the

other 40 GHz clock recoveries compared. The 40 GHz to 10 GHz clock recovery, however, outperforms the implementation presented in this work by far if only jitter is considered. Compared to the other implementations, this clock recovery is based on cross absorption modulation in the EAM. This leads to a significantly reduced influence of the injected power. In addition, a much longer loop length of 3000 m is used, leading to a much narrower locking range of ~ 5 kHz [44] and also a much smaller loop bandwidth of the setup [53]. This reduces the timing jitter of the recovered clock significantly. This leads to the conclusion that a trade off has to be made between locking range, loop bandwidth and jitter performance when designing a clock recovery.

Publication	[47]	[46]	[54]	[44]
Principle	OEO	OEO	SOA with MLL	OEO
Frequencies	160GHz / 40GHz	160GHz / 40GHz	640GHz / 40GHz	40GHz / 10GHz
Integration range	10Hz ... 40MHz	10Hz ... 18.6MHz	100Hz ... 10MHz	100Hz ... 1MHz
σ_{RMS} [fs] (Cited/Own)	221 / 140	283 / 140	73 / 75	42 / 73
IBRPN [$^{\circ}$] (Cited /Own)	12.7 / 6.46	16.3 / 6.46	16.8 / 3.46	0.60 / 3.37

Table 6.3. σ_{RMS} and input bitrate referred phase noise (IBRPN) of the optoelectronic oscillator implementation presented in this thesis compared to values found in the literature for different clock recovery circuits. The “own” values are extrapolated values based on own experimental results.

6.5 Summary

42.7 GHz subharmonic optical clock recovery from 128.1 Gbit/s data streams was demonstrated using an injection-locked opto-electronic oscillator. The RMS timing jitter of the recovered clock was as low as $\sigma_{\text{RMS}} = 72$ fs (100 Hz – 1 MHz). The minimum average optical power of the data input signal required for stable injection locking was $P_{\text{data}} = 5.0$ dBm with a dynamic range of 5 dB. An RF reference signal is not required.

7 All-Optical Signal Regenerators

All-optical regeneration is a desirable and potentially critical function within future optical communication systems and becomes progressively more attractive as transmission speeds increase. With the rapid emergence of 100 Gbit/s Ethernet (100GbE) as a natural progression from the current 10GbE systems there is a pressing need to establish regeneration approaches capable of operating at such speeds. All-optical signal regenerators are compact, cost-effective and highly efficient solutions for regenerating signals [55].

As a central part of the optical switching node proposed in this work, the 2R-regenerator subsystem must be able to provide regeneration of multiple 130 Gbit/s wavelength channels by one single device. The feature of high-speed multi-wavelength regeneration is very important in the proposed system in terms of cost as well as energy efficiency. It provides simultaneous regeneration of an intensity modulated on-off keying (OOK) WDM signal incorporating a number of individual wavelength channels. Therefore, it will eliminate the requirement of demultiplexing WDM signals to individual wavelength channels, and the use of a single regenerative device per wavelength followed by subsequent multiplexing.

Recently, differential phase shift keying (DPSK) has gained interest for use in high-speed transmission systems. The main advantage of DPSK over OOK comes from the 3-dB improved tolerance to optical noise (equal to less OSNR requirement), provided that balanced detection is employed [5]. Consequently, all-optical regenerators and wavelength converters for phase-sensitive communication formats are of high interest because they potentially increase link-lengths, regenerate degraded signals in point-to-point and next-generation meshed transparent networks, or simply overcome wavelength blocking in cross-connects and routers at low cost [5],[56].

In this chapter, we first review the fundamentals of fiber-based multi-wavelength regeneration (Note that a brief discussion of the fundamental characteristics of SPM and XPM is presented in Appendix A 2.). We then discuss the extension of this approach to multi-channel operation, which is significantly complicated by the inter-channel cross-talk induced through cross-phase modulation (XPM) and four-wave mixing (FWM) among the various channels. As a first solution, we extend the well-known Mamyshev approach for single-wavelength operation and propose a 43 Gbit/s multi-wavelength scheme for regenerating up to three 33% duty-cycle RZ-OOK channels. This technique is based on co-propagation of the channels in the fiber with a carefully designed dispersion map for reducing the inter-channel cross-talk. As a second solution, a bi-directional scheme is exploited to demonstrate the simultaneous regeneration of two 130 Gbit/s channels. This represents the highest speed dual-channel regenerator ever reported in a single fiber and is made possible by a very careful choice of the HNLF parameters. Excellent performance with negligible cross talk is obtained for both implementations. The last section is dedicated to a SOA-based Mach-Zehnder interferometer for DPSK

wavelength conversion and regeneration. We show experimentally the feasibility, and we predict the limits of the reamplifying, retiming and reshaping (3R) SOA-based MZI all-optical DPSK wavelength converter. We further discuss how these devices can be cascaded an arbitrary number of times.

7.1 Fiber-Based Multi-Wavelength Regenerators

7.1.1 Fundamentals

All-optical regeneration relying on self-phase modulation (SPM)-induced spectral broadening and subsequent off-center filtering has attracted particular interest due to its simplicity and ability to suppress both power variations and noise of marks and spaces of return-to-zero (RZ) amplitude modulated signals. This 2R (reshaping and reamplification) regeneration technique was originally reported by Mamyshev [4] and is schematically illustrated in the block diagram of Fig. 7.1. The degraded optical pulse streams are first fed into an optical amplifier which is used to boost the power to a suitable level at the input of the highly nonlinear fiber (HNLF). The amplified pulses then propagate in the HNLF where they experience spectral broadening due to Kerr-induced SPM. A narrow-band filter is used to carve the broadened spectrum at the output of the HNLF discriminating high from low input peak power pulses and thus providing a pulse reshaping operation, as shown in Fig. 7.1. This produces a step-like (close to binary) optical transfer function (TF) and offers reshaping

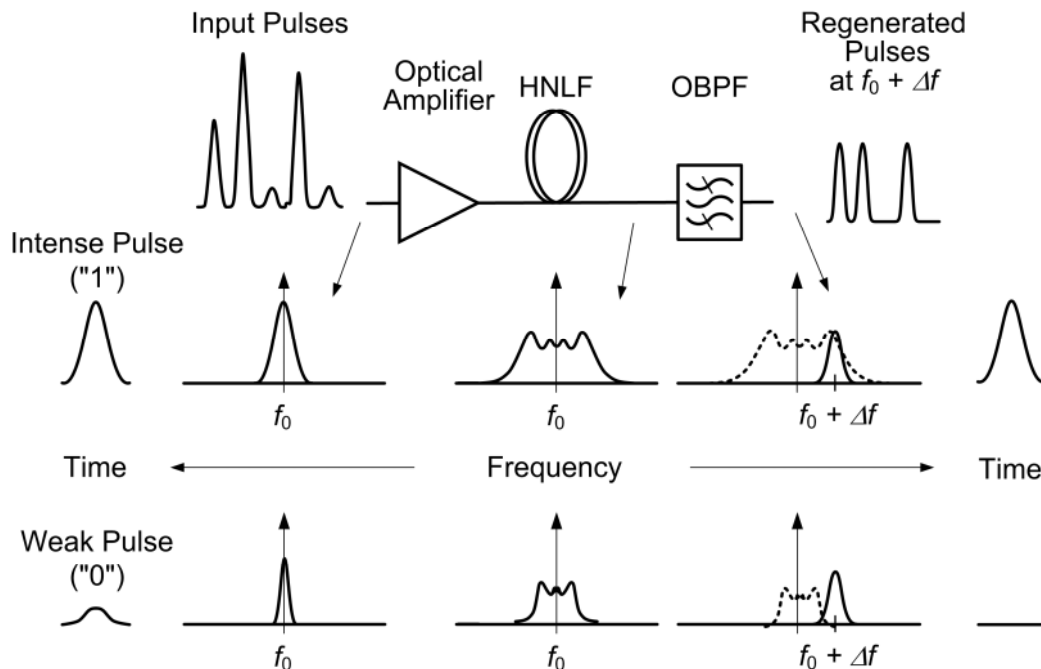


Fig. 7.1. Schematic of an optical regenerator based on SPM and offset filtering. Only high peak power pulses experience sufficient spectral broadening in the HNLF such that a portion of the spectrum passes the offset filter and forms the output pulse.

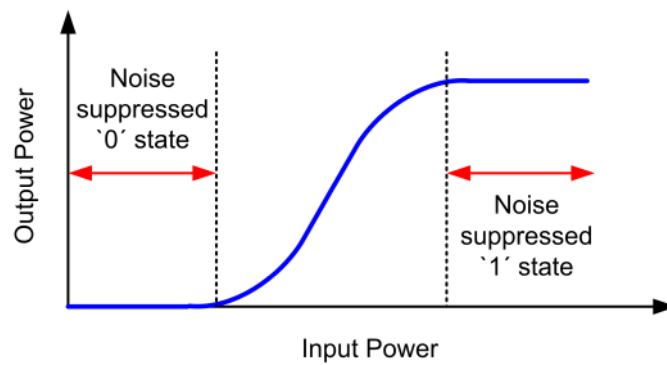


Fig. 7.2. Schematic illustration of optical power transfer function. Due to the plateau regions for low (“0”) and high (“1”) power input signals, noise of the output signal is reduced.

of the optical pulses through suppression of the noise on the zeros and the amplitude fluctuations of the ones. In this work, the TF is simply defined as the output peak pulse power as a function of the input peak pulse power (see also Fig. 7.2). However, this definition should not be mistaken for the transfer function $H(j\omega)$ of linear, time-invariant (LTI) systems.

For the experimental results presented in this chapter, the TFs were determined measuring the average output signal power as a function of the average input signal power using optical power meters. However, it is always possible to go from this type of TF to the one based on pulse peak powers as soon as the actual signal pulse shape and the mark/space ratio of the pseudo random bit sequence (PRBS) used are known. It should be noted that as the filtering takes place at a frequency shifted compared to the carrier frequency of the input signal, wavelength conversion is also introduced. If this wavelength conversion of the input signal is undesirable, then two stages of regeneration can be cascaded with the second stage canceling the wavelength shift introduced by the first one. Furthermore, if the fiber parameters are carefully chosen, this technique can support very high bit rates.

Extension to Multi-Wavelength Operation

Unfortunately, the single-wavelength Mamyshev concept requires an expensive amplifier and a nonlinear fiber for each channel. To reduce the cost related with the nonlinear element, it is desirable to share the nonlinear fiber by simultaneously processing two or more signals. The extension of the scheme to a multi-channel environment is significantly complicated by the inter-channel cross-talk arising both from XPM and four-wave mixing. The cross-talk manifests itself by the introduction of asymmetries of varying strength of the broadened spectrum due to partial interactions between co-propagating pulses of adjacent channels. This crosstalk can be minimized by ensuring 1) that pulses at different wavelengths always propagate at different speeds in the fibre, in which case XPM adds a constant phase shift across the full duration of the pulse, and 2) that the interaction distance between pulses of adjacent channels is minimized, which ensures that the phase-matching condition for FWM is cancelled [57].

Two approaches have been adopted that satisfy both conditions. The first solution presented here is based on management of the chromatic dispersion (CD) along the device [58] which allows for effective control of the inter-channel cross-talk interactions. The second solution is

a bi-directional geometry [57], such that each bit of a given channel undergoes complete ‘head-on’ collisions with a large number of counter-propagating bits from the second channel. In this instance the effects of XPM average out to provide a constant and tolerable level of crosstalk.

In the following, experimental results for both multi-wavelength regeneration approaches mentioned above are presented. First, 43 Gbit/s multi-wavelength 2R regeneration in a single dispersion-managed fiber is demonstrated, based on SPM-induced spectral broadening and subsequent offset filtering. Second, the counter-propagation scheme is used to demonstrate the simultaneous regeneration of two 130 Gbit/s channels, thus achieving substantial cost benefits as compared to two single-channel systems.

7.1.2 Dispersion-Managed Multi-Wavelength Regeneration of 43 Gbit/s WDM Channels

Introduction

Recently, simulations have indicated that the Mamyshev technique should be compatible with true multi-wavelength regeneration by sharing a single amplifier and a properly designed dispersion managed fiber assembly with several co-propagating signals [58],[59]. Indeed, a proof-of-principle experiment with one 10 Gbit/s channel based on alternating sections of nonlinear fiber and periodic group-delay devices (PGDD) has indicated its feasibility. In this approach the PGDDs were used in order to ensure unidirectional walk-off between the pulses of adjacent channels [58],[60]. In another approach alternating sections of dispersion compensating fibers (DCF) and standard single mode fibers (SMF) have been used to demonstrate regeneration with 4×10 Gbit/s, utilizing, however, low-duty cycle RZ pulses ($\sim 8.3\%$) [61].

The key to the multi-wavelength capability is management of the chromatic dispersion (CD) along the device which allows for effective control of the inter-channel cross-talk interactions. In an analogous manner to dispersion managed optical transmission, the scheme eliminates nonlinear interchannel cross-talk (cross-phase modulation (XPM), four-wave mixing (FWM)) by allowing a rapid walk-off between adjacent channel (due to locally high values of CD) without compromising the SPM-induced spectral broadening. This is achieved by maintaining a low path-average CD value over the regenerator length. The proposed regenerator comprises several fiber spans (or cells), made of a section of nonlinear fiber, for example dispersion compensating fiber (DCF), and followed by a periodic group delay device (PGDD) that compensates for the accumulated dispersion. This allows the channels to travel at different speeds and therefore reduces the effects of interchannel FWM and XPM. In [59] it has been shown numerically that the scheme can still provide regenerative capabilities in a multi-channel environment when the PGDDs are replaced by standard single mode fiber (SMF), and the dispersion map is made asymmetric. Fig. 7.3 shows a schematic of the proposed setup. In the following section, 43 Gbit/s multi-wavelength regeneration using the simplified approach based on alternating sections of DCF with SMF for regenerating three 33% duty-cycle RZ channels is demonstrated. The performance of the design proposed in [59] is validated,

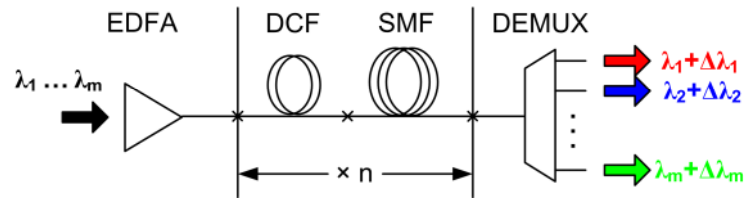


Fig. 7.3. Schematic of the dispersion-managed regenerator.

employing a dispersion map that provides a maximum excursion of ~ 75 ps differential group delay (DGD) for channels separated by 600 GHz within each cell (i.e. 3 bit-slots duration for a 43 Gbit/s signal).

Parts of this subchapter have been published previously in [62] and [63].

Experimental Setup

To demonstrate multi-wavelength regeneration with two and three 43 Gbit/s channels, respectively, we built the setup shown in Fig. 7.4. It comprises a 43 Gbit/s three channel transmitter, a signal decorrelation stage, the regenerator and a receiver. The transmitter consists of three distributed feedback (DFB) lasers on a 600 GHz grid, an arrayed-waveguide grating (AWG) and two modulators acting as a pulse carver (PC) and data encoder (DE), respectively.

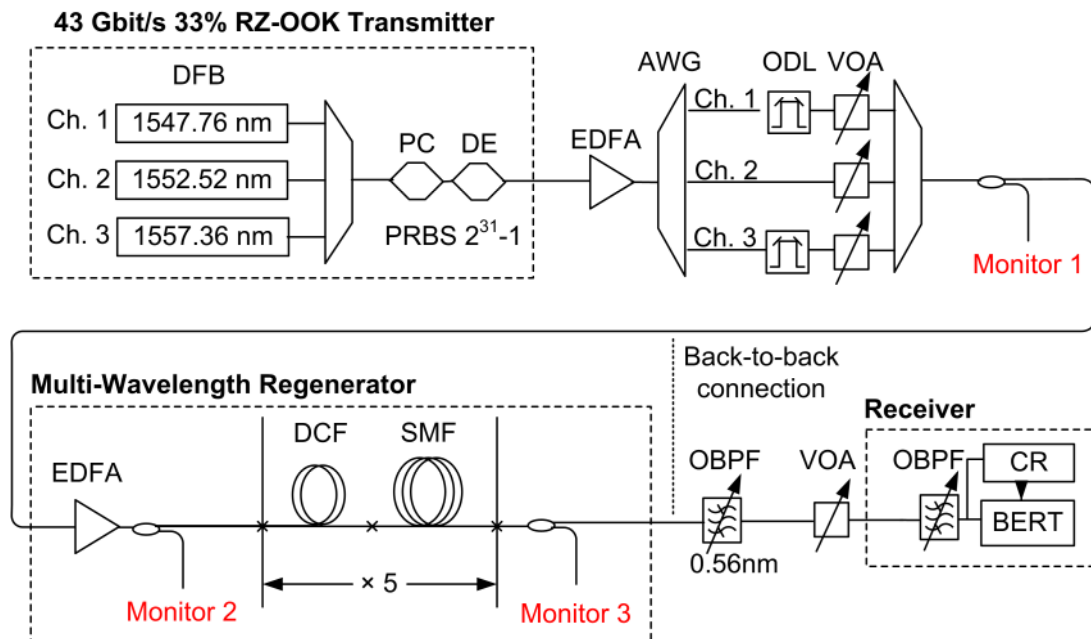


Fig. 7.4. Experimental setup of the 2R regeneration experiment. Three 43 Gbit/s signals modulated by the same PRBS are decorrelated using optical delay lines (ODLs) and launched into the multi-wavelength regenerator. The regenerator comprises an erbium-doped fiber amplifier and five identical fiber cells. The regenerated output signals are characterized by using a receiver with optical preamplification. PC – pulse carver; DE – data encoder; AWG – arrayed waveguide grating; VOA – variable optical attenuator; CR – clock recovery; OBPF – optical band pass filter. Monitor1 ... Monitor3 denote different points in the setup where optical spectra are measured.

The lasers are amplitude modulated by a $2^{31}-1$ long PRBS. In the subsequent stage, the optical delay lines (ODL) provide some pattern decorrelation and adjustment of the relative time delays between the channels on a bit basis, while the variable optical attenuators (VOA) provide channel power equalization and allow for single-, dual and three-channel operation by attenuating appropriately each one of the WDM channels. Frequency resolved electro-absorption gating (FREAG)-based characterization of the optical pulses at the output of this stage revealed negligible chirp and pulse widths of ~ 8 ps for all three channels. The subsequent regenerator consists of a high-power optical amplifier (EDFA), the fiber assembly and a tunable optical band-pass filter (OBPF) that allowed for the individual selection of channels. The filter was detuned by -0.6 nm from the center wavelength and closely resembles the response of a 1st order Gaussian filter with 0.57 nm 3 dB bandwidth. The 5970 m long fiber assembly contained five identical pairs of DCF and SMF with the parameters given in Fig. 7.5. The walk-off inside each DCF piece between two channels with 600 (1200) GHz channel spacing approximately equals the duration of 3 (6) bit slots at 43 Gbit/s, while the length of the SMF pieces adjusts the average dispersion to nearly $+1$ ps/nm/km.

The total insertion loss of the device was measured to be 9 dB, due mainly to the splicing losses between DCF and SMF (~ 1 dB per splice). The use of the optimized dispersion map facilitates high local dispersion, which minimizes the inter-channel nonlinear effects (FWM and XPM), and low average dispersion, which retains the integrity of the pulses and the potential for SPM-induced spectral broadening of each channel.

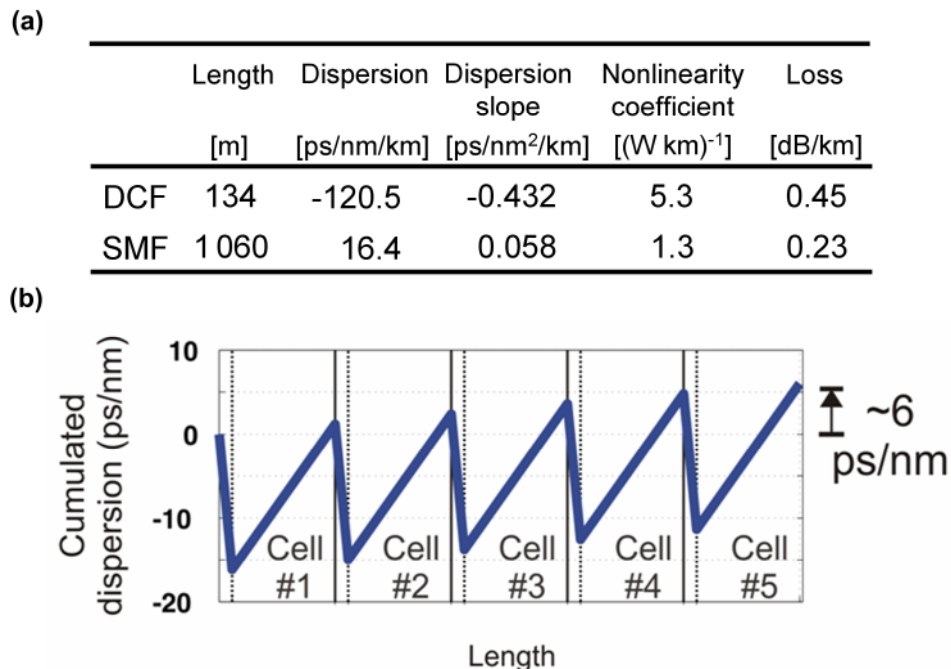


Fig. 7.5. (a) Fiber parameters of one of the five identical cells and (b) chromatic dispersion map of the whole fiber assembly used in the experiments. The length of the SMF was selected to offer a total residual dispersion of 6 ps/nm. All data are specified at 1550 nm.

Results and Discussion

The input-output average-power transfer functions (TFs) were extracted for each channel separately, using mark pulses at a repetition rate of 42.7 GHz and an optimized offset of the OBF, equal to -0.6 nm with respect to the initial carrier wavelength for all the channels. The experimentally retrieved TFs are illustrated in Fig. 7.6. The low variation among the three TFs is explained by the close resemblance of the input pulses and the low wavelength dependence of the dispersion map. The regenerator performance was first evaluated considering two channel operation with Ch.1 (1547.76 nm) and Ch.3 (1557.36 nm) only (1200 GHz spacing). The input signals were deterministically degraded by choosing a non-optimum DE modulator bias voltage, resulting in peak power variation and limited extinction ratio (ER) for both channels. The power per channel entering the fiber assembly was optimized to

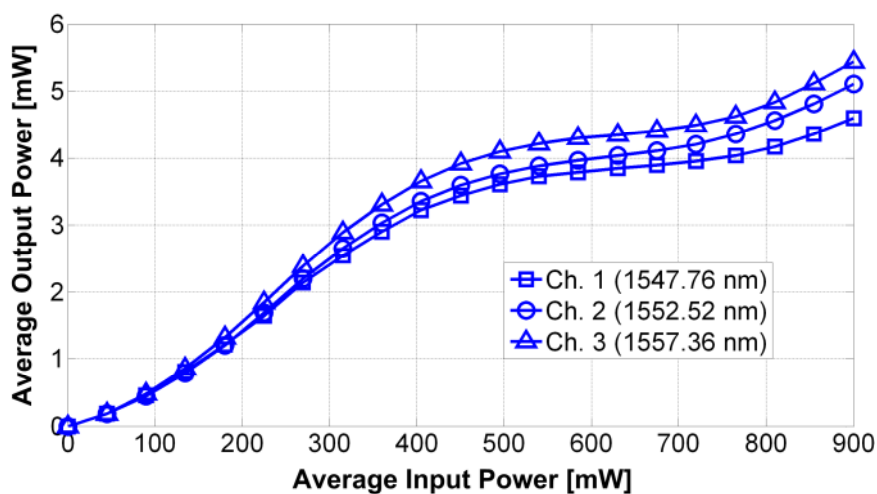


Fig. 7.6. Experimental average-power TFs, measured for each channel while the others were turned off.

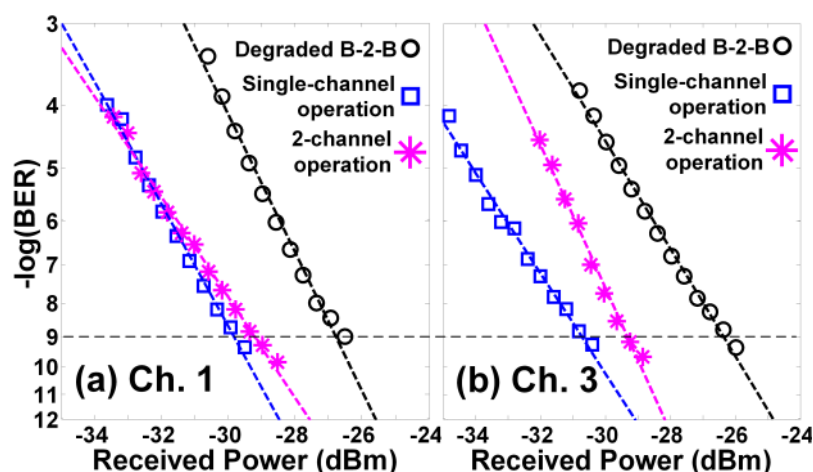


Fig. 7.7. BER measurements in single- and dual-channel operation (1200 GHz spacing) with degraded input signals: (a) Ch. 1 and (b) Ch. 3.

~360 mW, while in dual-channel operation the worst case for the relative delays was selected by adjusting the two ODLs “on the fly”. In Fig. 7.7(a)-(b), the bit-error-ratio (BER) curves are presented for each channel, each one related to the input, the regenerator output in single-channel operation and the output in dual-channel operation (presence of interfering channel), respectively. Actually, regeneration and a limited degree of residual nonlinear crosstalk can be identified in Fig. 7.7, with the smallest sensitivity penalty improvement at the level of $\text{BER} = 10^{-9}$ being 2.5 dB for Ch.1 in dual-channel operation. For both channels, the BER curves for single-channel operation and for a degraded input signal are almost shifted in parallel, respectively. Such an effect is typical for a reduced extinction ratio of the modulation. However, the BER curves for single-channel operation compared to the ones for 2-channel operation have different gradients. Such behavior indicates different noise distributions in the signal under test (see also Appendix A 1.1).

In order to identify the performance limitations of the current regenerator design, a third channel, allocated at 1552.52 nm, was added in-between the two channels, allowing for a three-channel operation study with 600 GHz channel spacing. For the same degraded input signal as before an error-floor was observed for Ch.2 and Ch.3 in 3-channel operation (although no additional penalty was induced by the regenerator when undegraded input signals

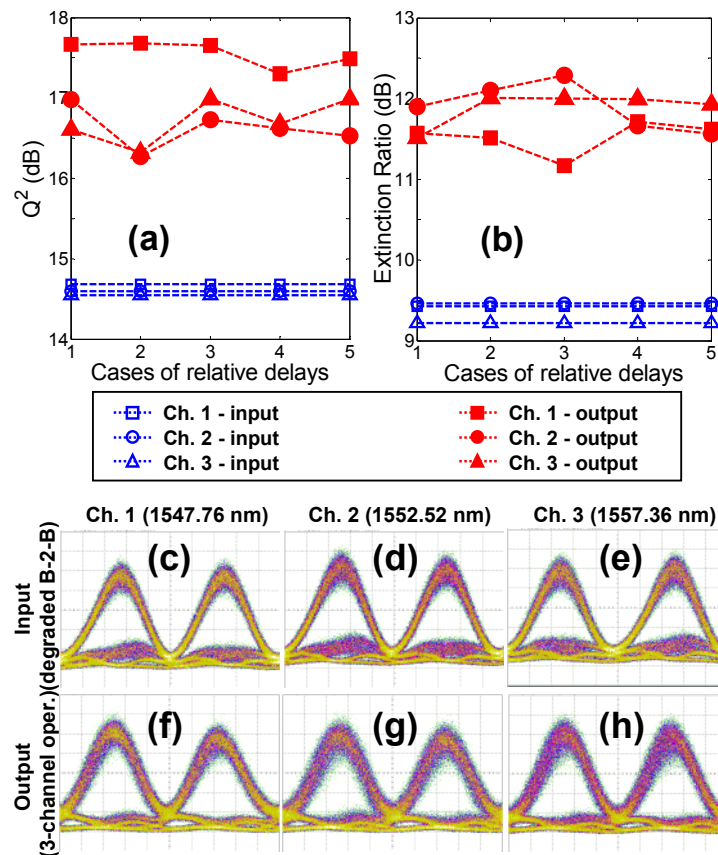


Fig. 7.8. (a) Q-factor and (b) ER measurements in three-channel operation (600 GHz channel spacing), (f)-(h) output eye diagrams in three-channel operation with degraded input signals (c)-(e). Clearly, the input pulse width is preserved after regeneration.

were used). In order to identify the origin of this behavior, eye diagram-based Q-factor, extinction ratio (ER) and timing jitter measurements were made on the input and output signals. Five randomly chosen combinations of relative time delays were considered, and the results in Fig. 7.8(a)-(b) reveal $(Q\text{-factor})^2$ and ER improvement ranging from 1.7 to 2.8 dB and 1.6 to 2.1 dB, respectively. Nevertheless, the eye diagrams of Fig. 7.8(f)-(h), corresponding to the worst-case delay for each channel with respect to output Q-factor, indicate that the XPM-induced timing jitter of the outputs is the main reason for the performance deterioration at 600 GHz channel spacing.

7.1.3 2R Regeneration of Two Counterpropagating 130 Gbit/s Channels

The interplay between nonlinear and dispersive effects makes operation of co-propagation schemes at ultrahigh repetition rates very challenging. To date, most research has focused on single channel operation, since direct extension to the multi-channel regime is generally restricted by inter-channel nonlinearities that compete directly with SPM. These effects result in distortions of the broadened spectra which manifest themselves as large signal power fluctuations after the output filter. Recent work has shown that these effects can be reduced to tolerable levels by ensuring complete and rapid “walk-through” of the data pulses – either by exploiting some form of specific chromatic dispersion management (see section 7.1.2) within complex fiber assemblies [64],[65],[62], by using dispersion decreasing fiber [66], or by using bi-directional propagation [57].

In this section, the bi-directional scheme proposed in [57] is exploited to demonstrate the simultaneous regeneration of two 130 Gbit/s channels, thus achieving substantive cost benefits as compared to two single-channel systems. This represents the highest speed dual-channel regenerator ever reported in a single fiber and is made possible by a very careful choice of the HNLF parameters [67]. Excellent performance with negligible cross talk is obtained for both channels.

Fig. 7.9 schematically illustrates the implementation of the bidirectional scheme. As already pointed out, the major benefit of this solution lies in the extremely high relative walk-off

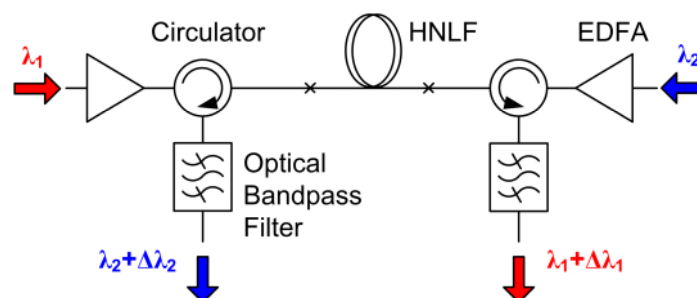


Fig. 7.9. Schematic of the bi-directional regenerator. Two different wavelengths λ_1 and λ_2 counter-propagate in a single highly nonlinear fiber (HNLF) and are subsequently offset filtered at $\lambda_1 + \Delta\lambda_1$ and $\lambda_2 + \Delta\lambda_2$, respectively. EDFA – erbium doped fiber amplifier.

between the two counter-propagating channels. The immediate result of a high walk-off is that the nonlinear phase induced by XPM manifests itself as a constant phase shift across the whole pulse train. It follows that no additional frequencies are generated from this XPM contribution, reducing the distortion induced on the SPM-broadened spectrum. Similarly, because of the relatively high walk-off, there is no FWM phase-matching condition between the two counter-propagating pulses. Last but not least, the general operating principles relating to the single channel regenerator are preserved and can be applied directly to the bi-directional configuration.

Despite the reduction in the XPM crosstalk, the proposed bi-directional architecture introduces a new source of crosstalk resulting from the reflections of the counter-propagating signal as it propagates along the HNLF. Since these reflections co-propagate with the second signal, they may give rise to some performance degradation and therefore their contribution was thoroughly investigated in the experiment.

Parts of this subchapter have been published in [32] and [68].

Experimental Setup and Results

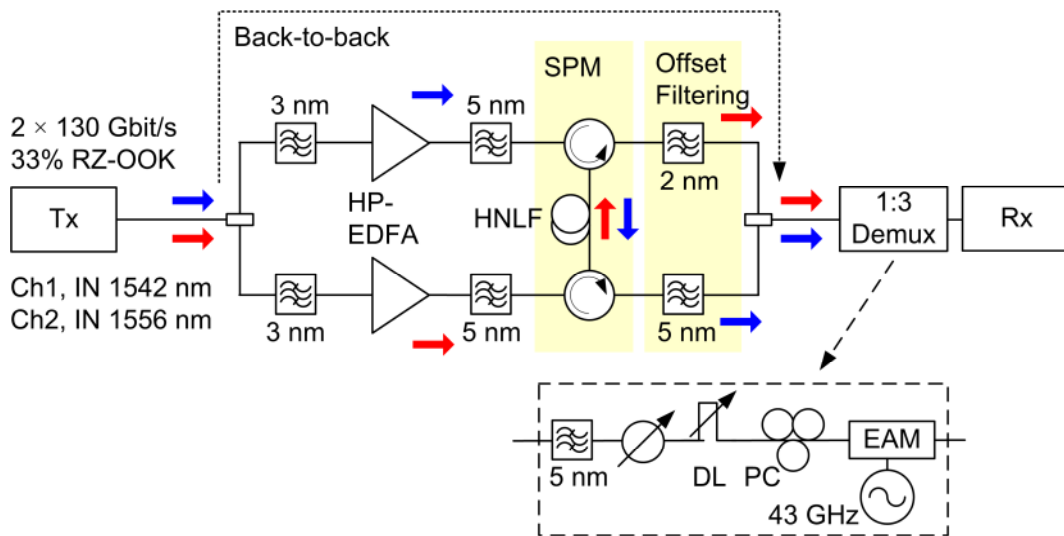


Fig. 7.10. Experimental setup for counter-propagation scheme. RZ-OOK - return-to-zero on-off keying, EDFA - Erbium-doped fiber amplifier, DL - delay line, PC - polarization controller, TX - transmitter.

Two 40 GHz mode locked fiber lasers operating at 1542 nm (Channel 1) and 1556 nm (Channel 2) are used to generate ~ 2 ps pulses. The two signals are amplitude modulated by a 2^7-1 pseudorandom bit sequence (PRBS), temporally multiplexed to 130 Gbit/s and combined together before entering the 2R regenerator depicted in Fig. 7.10. In the regenerator the data streams are split with optical filters (3nm bandwidth) to allow the signals to be fed into a single HNLF in counter-propagating directions (two HNLF ports). Each optical signal is then separately amplified to meet the input power requirements and fed to the HNLF. Two optical circulators are used to separate incoming from outgoing signals at the two fiber input/output ports. The 310 m-long HNLF has a chromatic dispersion of $C = -0.31$ ps/nm/km, a dispersion slope of $D = 0.0031$ ps/nm²/km, a nonlinear coefficient of $\gamma = 22$ (Wkm)⁻¹ and an attenuation

of 1.21 dB/km (all data are specified at 1550 nm). Note that the fiber properties were carefully selected taking into consideration the design maps outlined in [8], with the low dispersion slope being the key to high-performance dual-channel operation. The outgoing signals were filtered at an offset of ~ 3 nm with respect to the incoming carrier wavelengths (filter bandwidth at -3 dB is 2 nm), in order to preserve the initial channel separation. Finally, the signals were demultiplexed to 40 Gbit/s, using an electro-absorption modulator (EAM) to allow proper characterization of the system, see inset of Fig. 7.10. back-scattering of the counter propagating channel [57]. Furthermore, due to the very low dispersion slope of the HNLFF, the two channels (spaced by ~ 14 nm) exhibit quite similar TFs. Spectral traces of the two channels, measured at different points of the system, are shown in Fig. 7.11(c). The broadened spectra after the HNLFF of each channel clearly illustrate the Rayleigh back-scattering contribution of the counter-propagating channel as discussed already. Its main consequence is to reduce the output extinction ratio of the measured TFs.

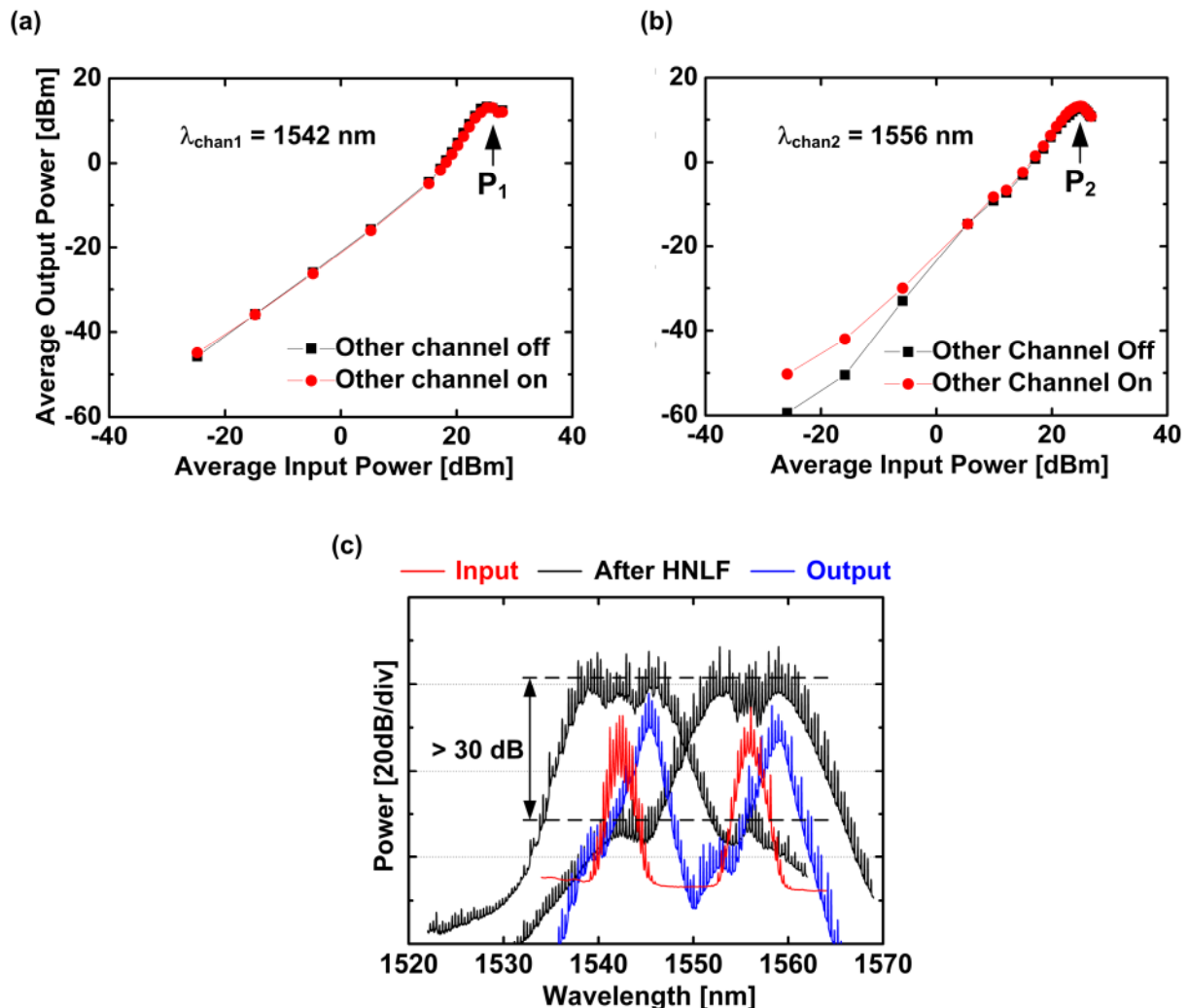


Fig. 7.11. Average power transfer functions of (a) Channel 1 and (b) Channel 2 in the presence (other channel on), or absence (other channel off), of the second signal. (c) Optical spectra of the two channels measured at different points within in the regenerator. The back-scattering level is > 30 dB below the corresponding broadened spectrum (after HNLFF), and the cross talk between the two channels is therefore negligible.

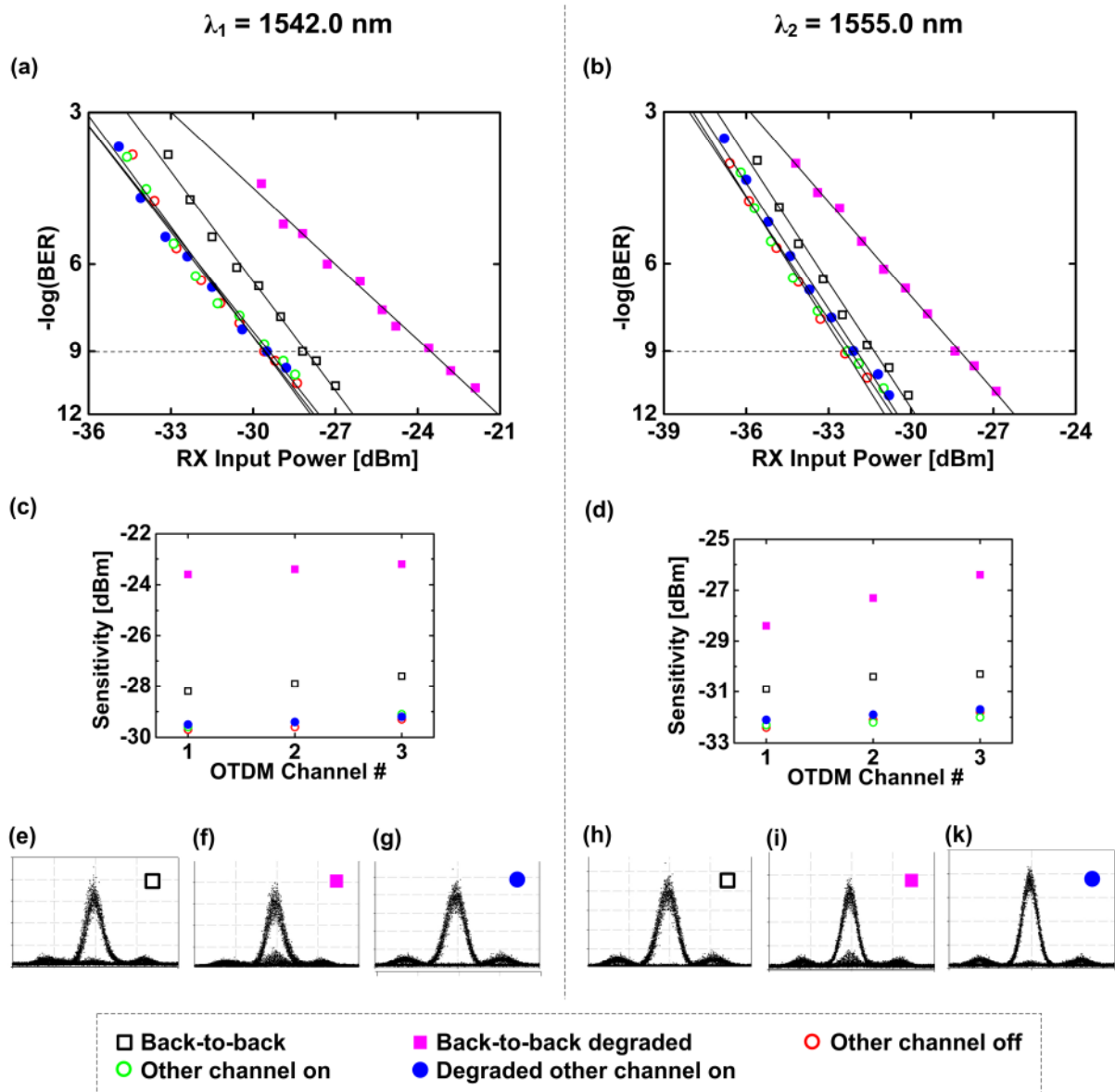


Fig. 7.12. BER curves for the undistorted (empty symbols) and distorted (filled symbols) back-to-back signals (rectangular symbols), and for the corresponding regenerated (circles) signals for (a) Channel 1 and (b) Channel 2, respectively, in the absence or presence of the interfering channel. Insets: Corresponding receiver sensitivities for the two channels ($\text{BER} = 10^{-9}$). Demultiplexed eye diagrams of the ((c) and (f)) undistorted and ((d) and (g)) distorted input channels to the regenerator. ((e) and (h)) Corresponding eye diagrams of the channels after the regenerator in presence of the interfering channel when the input signals are degraded. The eye diagrams were measured with an optical sampling oscilloscope.

However, this back-scattering level is found to be more than 30dB below the corresponding transmitted broadened spectrum, and the cross talk between the two channels is therefore negligible. We next performed bit-error-rate (BER) measurements on the two channels for both single- and dual-channel operation (see Fig. 7.12(a) and Fig. 7.12(b)). The performance of the regeneration system is very similar for both cases, highlighting the absence of any kind of cross-talk between the two channels. Note that the apparent BER improvement compared to the back-to-back curves is due to a non-optimal transmitter (see eye diagrams of the demultiplexed back-to-back signals in Fig. 7.12(e) and Fig. 7.12(h)), and the wavelength dependence of the EAM used in the demultiplexer, which exhibits better performance at longer wave-

lengths. We next artificially degraded the extinction ratio of the input signal to the regenerator by selecting a non-optimum bias voltage setting of the Mach-Zehnder-type data modulator. The corresponding demultiplexed eye diagrams for the two channels are shown in Fig. 7.12(f) and Fig. 7.12(i). After the regenerator, the corresponding BER measurements confirm that complete compensation of the ~ 4 dB power penalty (at $\text{BER}=10^{-9}$) introduced by the signal degradation is achieved at the regenerator output for both channels in the presence of the interfering channel. The corresponding regenerated demultiplexed signals are shown in Fig. 7.12(g) and Fig. 7.12(h) when both signals are on.

7.2 SOA-MZI based Regenerator for DPSK Signals

7.2.1 Introduction

In this subchapter, a novel all-optical differential phase-shift keying wavelength converter based on semiconductor optical amplifier nonlinearities is demonstrated in the 25- to 40-Gbit/s range with pseudorandom binary sequence of length $2^7 - 1$, and its regenerative properties as well as the cascadability are discussed.

Currently, differential phase-shift keying (DPSK) – because of its lower optical signal-to-noise ratio requirement and robustness towards nonlinear impairments [5] – seems to be the most promising phase-modulation format. In view of the significance of the DPSK format for next-generation systems, it would be highly desirable to have small-footprint, low power-consuming all-optical DPSK regenerators and wavelength converters. Solutions exploiting fiber-nonlinearity [69],[70] or four-wave mixing in semiconductor optical amplifiers (SOAs) have been tested [71]. Unfortunately, all of these solutions only offer a restricted wavelength conversion range and require high input powers. Recently, Sagnac [72] and Mach-Zehnder interferometer (MZI) devices [73] exploiting the more efficient SOA-based cross-phase modulation effect have been demonstrated and their regenerative potential has been shown. Yet, none of the MZI-based solutions also showed retiming regeneration, nor was the cascadability or the origin of the regenerative characteristics clarified. This is important, since DPSK is most likely to be used in systems at bit-rates of 40 Gbit/s and above, where retiming is an issue.

In this work, we show experimentally the feasibility and predict the limits of a retiming and reshaping SOA-based MZI all-optical DPSK wavelength converter. We further discuss how these devices can be cascaded an arbitrary number of times.

The results in this subchapter have been published partly in [74] and [75].

7.2.2 DPSK Wavelength Conversion Scheme and Experiment

The experimental setup and the all-optical DPSK wavelength converter are depicted in Fig. 7.13. The setup comprises a push-pull DPSK transmitter, an all-optical wavelength converter, and a balanced receiver with a differential encoder.

Operation Principle

The operation principle of the all-optical wavelength converter is as follows. An incoming DPSK signal is first converted into on-off keying (OOK) and inverted OOK signals in the delay interferometer (DI) stage. These on-off signals are then used for controlling the SOAs. They are injected with exact time correlation into the two control inputs of an MZI with SOAs [76]. The relative phase in the SOA arms is then controlled by a high level bit either in the OOK or in the inverse OOK arm, very similar to the push-pull operation of electrically controlled MZI modulators in DPSK transmitters [5]. An optical clock, derived from the

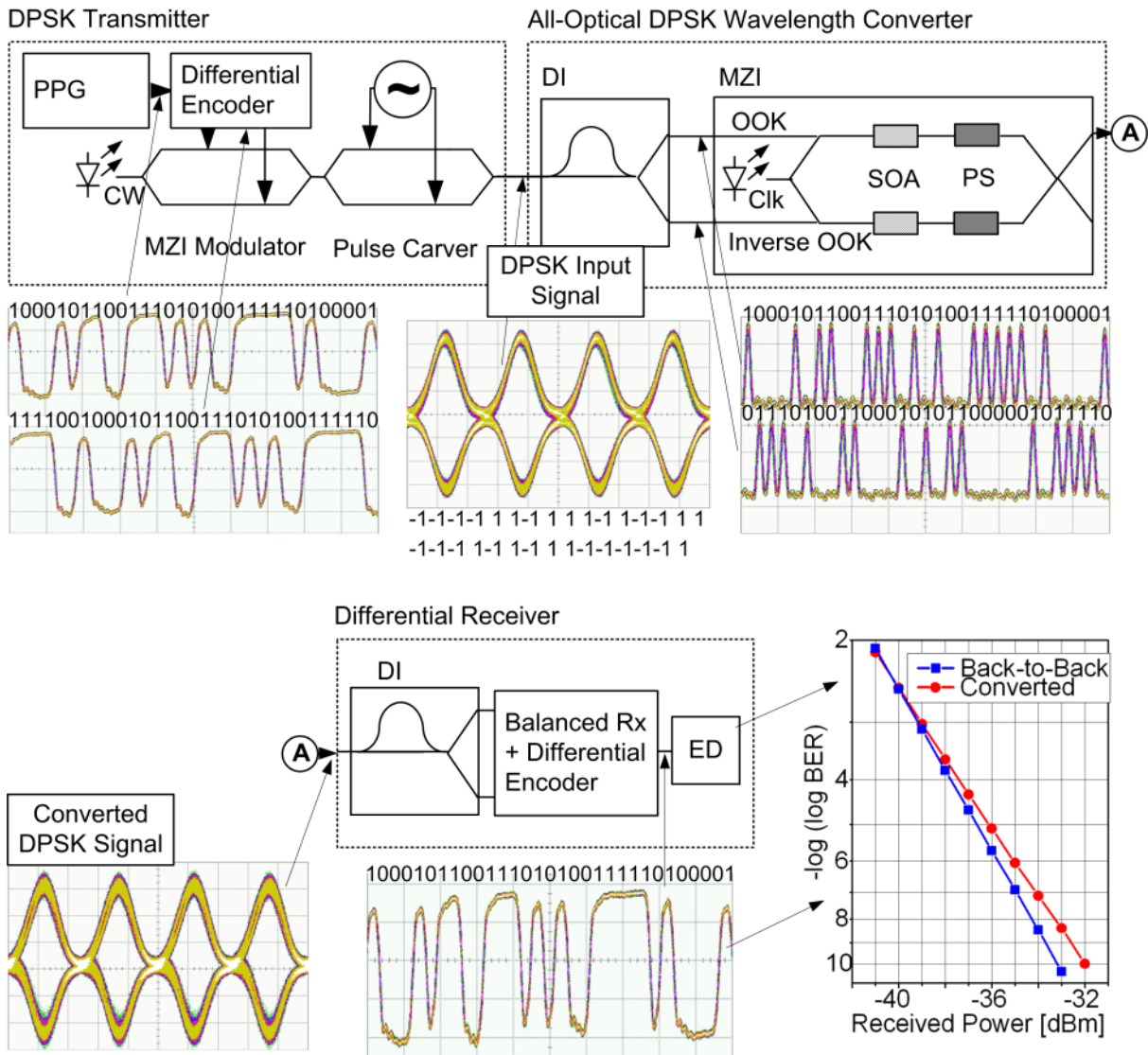


Fig. 7.13. Setup with DPSK transmitter, all-optical wavelength converter, and differential receiver with encoder. The two eye diagrams show DPSK signal entering and leaving the all-optical wavelength converter. For the demonstration, we reduced the bit rate to 31 Gbit/s because of pattern dependence at 40 Gbit/s. PPG – pulse pattern generator; DI – delay interferometer; MZI – Mach-Zehnder interferometer; Clk – clock; SOA - semiconductor optical amplifier; PS – phase shifter; ED – error detector.

input signal, is then introduced at the centre arm of the interferometer. The clock may be set to any wavelength within the SOA gain spectrum. This clock signal then picks up the phase information when travelling through the SOA arms and becomes the new phase encoded signal at the output. For the experiment we used an integrated DI followed by a monolithically integrated MZI SOA. A 3-dBm input signal at $\lambda = 1545$ nm with a pseudorandom binary sequence (PRBS) of length $2^7 - 1$ was used. The two fibers between the DI and MZI had the same length. The clock signal was taken from the transmitter and modulated a continuous-wave source at $\lambda = 1563$ nm with 12.5 dBm. We manually adjusted the temporal position of the data pulses to the optical clock pulses. In a practical implementation a clock recovery would be needed [77]. All powers were measured in the fiber before the SOA MZI.

A 31-bit sequence and the eye diagrams at the various stages of the setup are shown in Fig. 7.13. The eye diagrams of the DPSK signal before and behind the all-optical wavelength con-

verter are clear and open. The converted signal shows some pattern dependent noise due to the limited recovery time of the SOAs. This pattern dependence limited the operation to 40 Gbit/s. While at 40-Gbit/s error-free performance was possible, the pattern dependence decreased when reducing the bit rate to 31 Gbit/s and disappeared for 25 Gbit/s. The bit-error rate versus received signal power is plotted in the lower right side of Fig. 7.13. A small penalty of 1 dB for DPSK wavelength conversion is found at 31 Gbit/s. No error floor was observed.

The eye pattern and the bit sequences in Fig. 7.13 show how the input pattern undergoes various transitions. The nonreturn-to-zero input-pattern is plotted on the upper left side. It is then differentially encoded in order to produce the 33% return-to-zero (RZ)-DPSK signal at the output of the transmitter stage. In the wavelength converter, the signal is first guided into the DI, which produces an OOK and an inverse OOK pattern at the outputs. The new phase-encoded and wavelength-converted signal is then formed in the MZI stage. The phase and amplitude information – as annotated at the bottom of the eye diagrams before and after the converter – shows that the all-optical wavelength converter changes the coding scheme. In this experiment, the implementation of the differential encoder was not needed since a PRBS sequence was used, which is not sensitive to differential format changes.

7.2.3 Cascadability

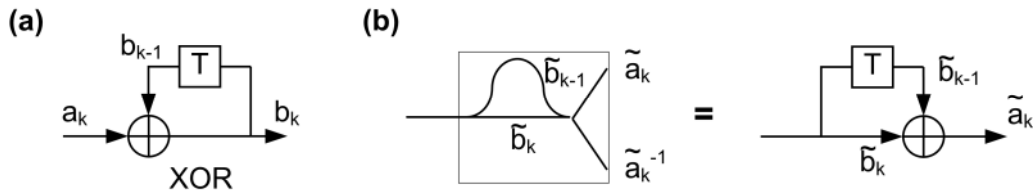


Fig. 7.14. (a) Logic operation performed by the differential encoder (typically an electronic device built into the receiver or transmitter); (b) operation performed by optical DI and its logic analogue.

Due to the various bit-pattern transformations, it is not obvious if cascading the all-optical DPSK wavelength converter signal is at all possible. Here we show that an arbitrary number of all-optical wavelength converters can be cascaded. The DI performs the inverse operation of the (electronic) differential encoder. The logic operation performed by the two devices is depicted in Fig. 7.14(a) and (b). For recovering the original data, an identical number of differential encoders (a) and DI stages (b) is needed. The two elements, however, can be arranged in any order. The minimum arrangement is one encoder/decoder pair “ab”, but a sequence “aaabbbab” would also be possible. To prove this statement, we note that encoder and DI perform the following modulo-2 operations:

$$b_k = b_{k-1} + a_k \quad (7.1)$$

$$\tilde{a}_k = \tilde{b}_k + \tilde{b}_{k-1} \quad (7.2)$$

and with $a_k, b_k, \tilde{a}_k, \tilde{b}_k \in \{0,1\}$, i.e.,

$$0+1=1+0=1 \quad \text{and} \quad 0+0=1+1=0. \quad (7.3)$$

By substitution, one shows that the output of a differential encoder followed by a DI returns identity if b_k is identical to \tilde{b}_k

$$\tilde{a}_k = \tilde{b}_k + \tilde{b}_{k-1} = b_{k-1} + a_k \tilde{b}_{k-1} = a_k \quad (7.4)$$

The same is true for the inverse arrangement. The original signal in a transmission link may now be recovered by forming pairs of encoders and DIs that cancel each other's operation. This is always possible if there are the same number of differential encoders and DIs in the link.

7.2.4 Regenerative Properties

In this section, we quantify the phase and amplitude regenerative properties of the all-optical wavelength converter.

The retiming capabilities of the suggested scheme are inherent for schemes with clocked sources [77]. Phase regeneration has been observed as well – both by us but also quantified by others [73]. However, the amplitude regeneration or a combination of the two effects has not yet been discussed. In order to quantify the regenerative properties, we generate a series of ideal and identical DPSK signals and then distort the phase and amplitude of a single central bit. We then send this sequence into the wavelength converter and quantify how this distortion affects phase and power of the phase-encoded and converted output signal with respect to undistorted reference bits. The analysis is performed with a transfer matrix model for the DI [78] and MZI [79] and employs an SOA model based on experimental results similar to [78]. The SOA parameters used were 10 dB single pass gain and an alpha factor of 8.

The effect of a phase deviation in the range $[-\pi, +\pi]$ for one DPSK input bit with respect to an ideal neighbouring reference bit is plotted in Fig. 7.15(a). It can be seen that phase variations

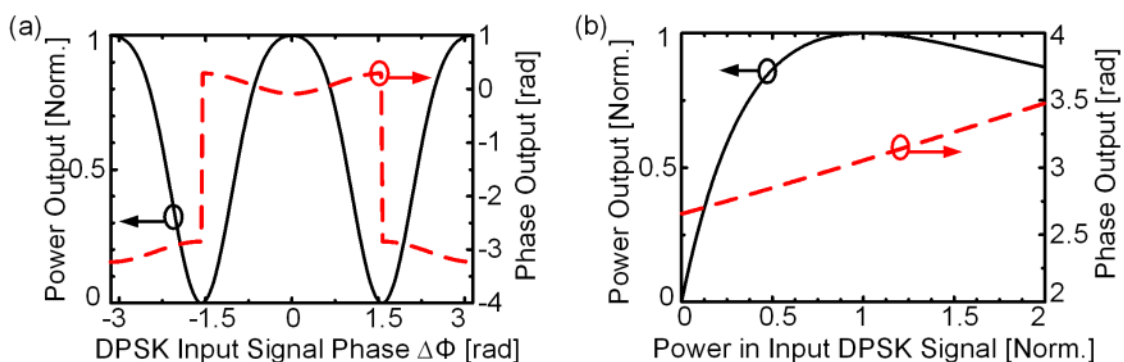


Fig. 7.15. Effect on DPSK output power and output phase if a distorted bit is introduced into an all-optical DPSK wavelength converter. Input signal distortions are given with respect to (a) phase offsets (ideal signal has “0” offset) and (b) power offsets (ideal signal has power “1”).

are suppressed as long as they do not exceed $\pm\pi/2$. The output power will make a transition from the amplitude “1” to a signal with amplitude “-1” when varying the phase of the distorted bit by $\pm\pi$ with respect to its reference bit. This behaviour agrees with that one expected from the transfer function behaviour of an ideal push-pull DPSK modulator – except for one difference. The power transfer function plotted in Fig. 7.15(a) is very flat around the ideal “1” (DPSK input phase zero) and “-1” positions (DPSK input phase $\pm\pi$). This is due to the nonlinear saturation of the SOA when a signal is injected resulting in very favourable and symmetric regeneration behaviour around the two DPSK states. Most interesting is also the shape of the output power and output phase for distorted DPSK input signal powers (Fig. 7.15(b)). When changing the power of a DPSK input bit between zero and twice the power of a reference bit, we find that the output phase is affected only a little. Likewise, the output power shows an extremely flat region around the ideal DPSK state and thus will be very tolerant to power fluctuations. This flat region is partly due to the distribution of power on neighbouring signals, i.e., during detection of a signal with the DI, the power is split into two parts and recombined with the power in the two neighbour pulses. This leads not only to identical differential errors in neighbours but also reduces the total error. Additionally, for signals with high input power levels, the SOA saturation characteristic further limits the power into the output.

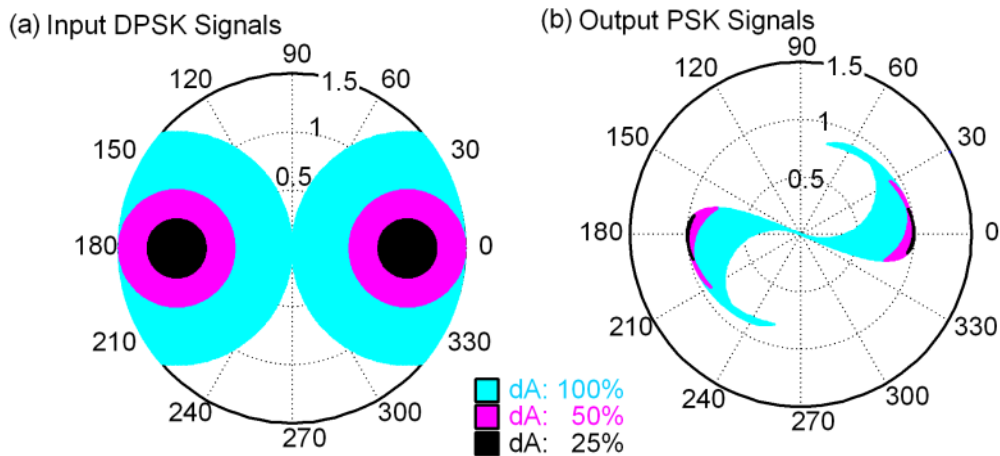


Fig. 7.16. Constellation diagrams of (a) DPSK input signals and (b) phase-encoded output signals. Areas of same shade are mapped onto the respective constellation space in the output. The shaded areas span the input space $dAe^{j\phi}$, with $dA = 25\%$, 50% , or 100% of the ideal amplitude around “1” and “-1”, and $\Delta\phi$ varied in $[0, 2\pi)$.

The constellation diagrams in Fig. 7.16 visualize how a signal with a particular phase and amplitude (Fig. 7.16(a)) is mapped on a new signal within the respective constellation space (Fig. 7.16(b)). The plots indicate how a shaded area is converted to a new area lying much closer to the ideal “1” and the “-1” DPSK states. The plots indicate considerable regeneration. Noteworthy is the strong amplitude regeneration.

To further support our findings, we performed simulations with noise loaded PRBS sequences of $2^{12} - 1$ over four laps of all-optical DPSK wavelength converters at 40 Gbit/s. All simulations were performed with OptSim from RSoft using our own SOA model. The SOA was

modelled to show a realistic 7 dB noise figure. Fiber-based nonlinear effects were neglected. The input eye diagram and histogram of the power distribution for an input signal with a quality factor of 16 dB is shown in the upper left corner of Fig. 7.17. When introducing this signal into our first wavelength converter stage, we find that a redistribution of signal power first leads to an initial degradation. Yet, the signal significantly improves when being sent into subsequent converter stages. Such behaviour is known from RZ all-optical wavelength converters [80].

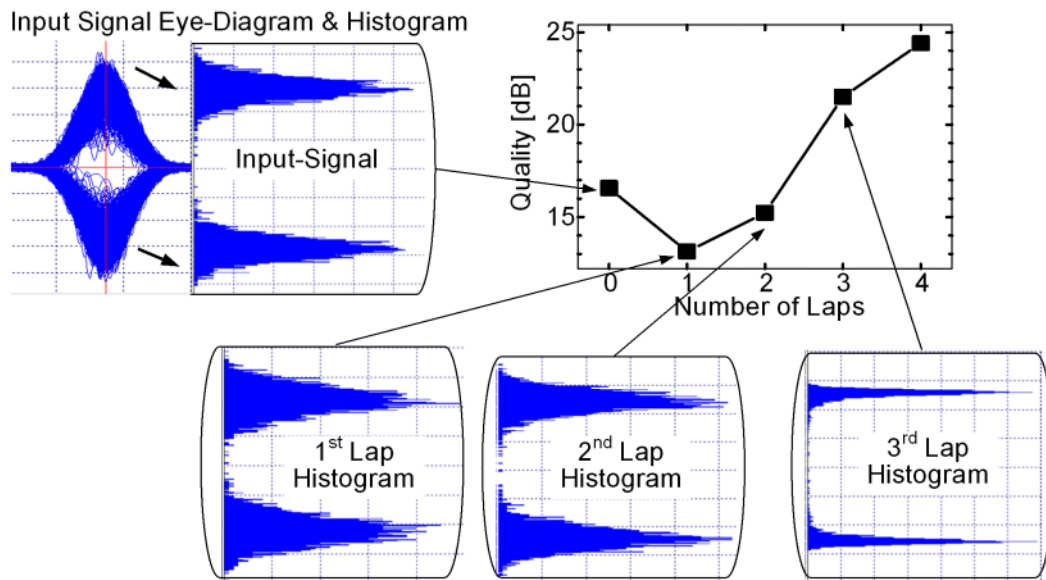


Fig. 7.17. Evolution of signal quality with increasing number of all-optical DPSK wavelength converter laps. The histograms indicate the power distributions of the DPSK signals after respective lap of conversion.

7.3 Summary

In this chapter, first experimental investigation at 43 Gb/s of a fiber based dispersion-managed 2R regenerator was presented utilizing pulses of 33% duty-cycle. Dual-channel regeneration at 1200 GHz channel spacing was reported, with sensitivity penalty improvement over 2.5 dB for degraded input signals.

We then experimentally demonstrated an extension of the Mamyshev regenerator scheme to the dual-channel case at a data rate of 130 Gbit/s by adopting a bidirectional scheme in a single fiber based device. BER measurements showed that no degradation exists as compared to the single channel case and demonstrate the excellent regenerative properties of the device for significantly degraded input signals.

Finally, a novel DPSK all-optical wavelength converter based on SOA technology had been presented. We have further shown analytically that these devices can be cascaded, and presented numerical results indicating their favourable regenerative properties.

8 Switch Node Demonstration

8.1 Introduction

In this work we introduce a novel optical switch concept that offers transparent optical grooming of 43 Gbit/s traffic in an access network to a metro core ring network operated at 130 Gbit/s. Key functionalities of the switch are traffic grooming with time-slot interchange (TSI), the OTDM-to-WDM conversion of the high-speed channel into lower bit-rate tributaries as well as multi-wavelength all-optical 2R regeneration of several high-speed signals. A MEMS switch in combination with all-optical wavelength conversion guarantees non-blocking space and wavelength switching functionality for any tributary.

The various subsystems of the switch node have been introduced and experimentally characterized in previous chapters of this work. The challenge now is to bring all the different optical technologies onto a common wavelength grid, assemble the optical switch with its functionalities and perform testing at bit-rates of 43 Gbit/s and 130 Gbit/s.

This chapter reports the results of the full node demonstration with multiplexing in frequency and time. The excellent performance of the proposed solution will be verified by studying a multiple of switching scenarios, showing dynamic bandwidth allocation for time-varying traffic demands. In addition, the scalability of the proposed switch node in terms of channel bit-rates and port-count as well as its cascadability will be discussed. As it will become apparent, the port scalability of this architecture, in terms of both OTDM and WDM channels, is restricted only by the port count of the space switch.

This chapter is organized as follows: In Section 8.2 we present the testbed implementation of the lab trial. Section 8.3 presents the results demonstrating the functionality and excellent performance of the switching node. Then, Section 8.4 discusses the scalability and cascadability of the concept. Finally, Section 8.5 summarizes our findings and discusses limitations and applicability of our approach.

Parts of this chapter have been published in [20] and [21].

8.2 Testbed Implementation

This section gives a detailed account of the testbed facility, its layout and main parameters. We discuss the design choices, as well as the challenges that were encountered, and the solutions developed. Fig. 8.1 depicts a functional diagram of the testbed. Note that optical attenuators, amplifiers and polarization controllers are not shown for clarity.

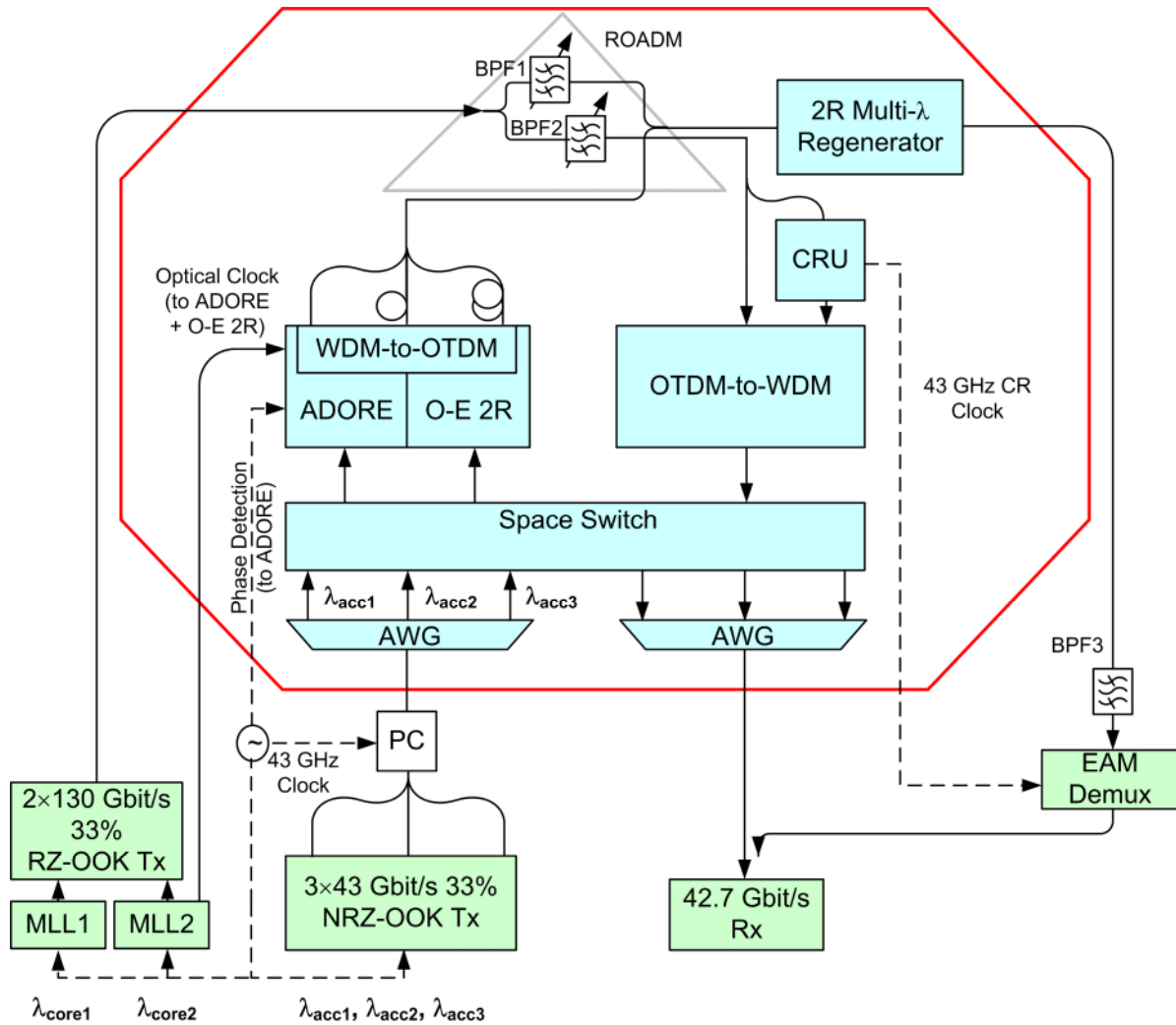


Fig. 8.1. Functional diagram of the testbed. BPF1 ... BPF3 – band pass filters; PC – pulse carver; MLL1, MLL2 – mode locked laser; CR – clock recovery; ROADM – reconfigurable optical add-drop multiplexer. $\lambda_{acc1} = 1551$ nm, $\lambda_{acc2} = 1556$ nm, $\lambda_{acc3} = 1561$ nm, $\lambda_{core1} = 1542$ nm, $\lambda_{core2} = 1556$ nm.

The switch itself comprises a ROADM, a space switch, the OTDM-to-WDM unit, a WDM-to-OTDM unit and a 2R multi-wavelength signal regenerator. The subsystems of the switch node have been introduced and experimentally characterized in previous chapters of this work. The implementation of the OTDM-to-WDM unit is based on self phase modulation (SPM) in a highly nonlinear fiber and subsequent temporal gating, see Section 5.2. The clock recovery unit, required for supplying a synchronous clock signal to the OTDM-to-WDM subsystem, is an opto-electronic oscillator (see Chapter 6). The WDM-to-OTDM unit is based on the asynchronous digital optical regeneration (ADORE) concept described in Chapter 4. Note that only one ADORE was built for this work, and two of the three input 43 Gbit/s channels

are processed by a simple O-E 2R regenerator. Therefore, retiming capability was only achieved for one input channel of the WDM-to-OTDM subsystem. Finally, the multi-wavelength regenerator is based on self-phase modulation and subsequent offset filtering of two counter-propagating channels (see Section 7.1.3). Reconfigurable add-drop multiplexing at the core ring is implemented with a set of two tunable band-pass filters with 5 nm 3-dB bandwidth. The space switch is based on an 8×8 MEMS switch fabric, with a reconfiguration time in the order of 1 ms and an insertion loss of around 3.5 dB for any switch configuration. All 43 Gbit/s channels, whether originating in the OTDM domain or the WDM domain, are input to the MEMS space switch, which provides non-blocking circuit connectivity.

In all, five wavelengths were generated to perform the demonstration. Three of those wavelengths, $\lambda_{\text{acc1}} = 1551$ nm, $\lambda_{\text{acc2}} = 1556$ nm, $\lambda_{\text{acc3}} = 1561$ nm, were 33% RZ-OOK modulated at 43 Gbit/s. These test signal sources were implemented using commercially available 43 Gbit/s NRZ-OOK transmitters in combination with a Mach-Zehnder type pulse carver (PC) for RZ pulse carving. Two other wavelengths, $\lambda_{\text{core1}} = 1542$ nm, $\lambda_{\text{core2}} = 1556$ nm, came from two mode-locked laser (MLL1, MLL2) sources that were also OOK modulated. The pulses from MLL2 were also used to provide an optical clock to the ADORE and the O-E 2R. The data rate of the MLL-based 43 Gbit/s signals were taken to be 130 Gbit/s with the use of optical multiplexers (for details see Section 3.4). The three 43 Gbit/s signals represent the traffic coming from the metro rings while the two 130 Gbit/s signals represent the traffic on the core ring. At the receiver (Rx), the error performance of the 43 Gbit/s signals was analyzed, whereas the 130 Gbit/s signals were first demultiplexed down to 43 Gbit/s (EAM Demux). Fig. 8.1 also shows the clock distribution. The synthesizer (43 GHz clock) was used for the Tx signals, as well as for the WDM-to-OTDM subsystem. The output of the clock recovery (43 GHz CR clock) was used for the OTDM-to-WDM subsystem and demultiplexing at the receiver.

The pulse widths of the 130 Gbit/s signals changed during propagation in the setup due to chromatic dispersion in the fiber patch cords and the EDFAs used. Precise pulse width adjustment to $\tau = 2.6$ ps FWHM (corresponding to 33% duty cycle) at the inputs of the self-phase modulation based subsystems (multi-wavelength regenerator and OTDM-to-WDM converter) was achieved by inserting different lengths of SMF and DCF. The correct input pulse width was critical since the performance of these subsystems has been designed for the 33% RZ-OOK format and strongly depends on the input pulse shape.

8.3 Results and Discussion

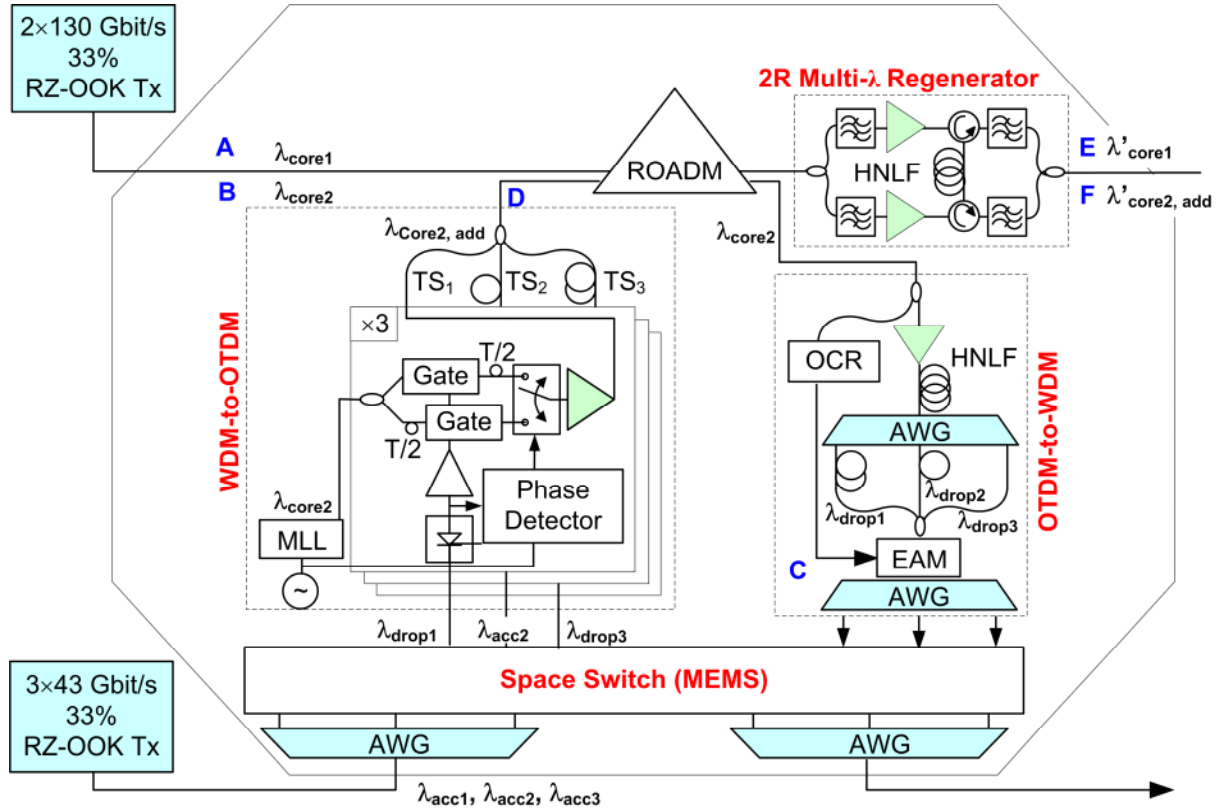


Fig. 8.2. Node architecture for switching scenario 1: λ_{core1} is switched through, see E. λ_{core2} is dropped and mapped to different tributaries (λ_{drop1} , λ_{drop2} , λ_{drop3}), see C. λ_{drop1} and λ_{drop3} are looped back together with the added λ_{access2} , see D, while λ_{drop2} is switched to the metro / access ring. The multi-wavelength core signal is finally regenerated, see E and F.

The switch interconnects two access rings, each carrying 3×43 Gbit/s WDM signals, with a core ring carrying 2×130 Gbit/s signals generated with mode-locked lasers.

To demonstrate the functionality of the grooming switch we show partial Add, Drop and TSI functionality by means of the following switching scenario (Fig. 8.2). In Fig. 8.2, capital blue letters are marking reference points in the setup where BER and Q-factor measurements have been performed. The core path supports two 130 Gbit/s signals (λ_{core1} , λ_{core2}) with Q-factors of 18.7 dB and 20.0 dB, respectively. Each one of them consists of 43 Gbit/s tributaries TS_1 , TS_2 , and TS_3 . In a first network scenario we drop TS_2 from λ_{core2} to λ_{drop2} and add access channel λ_{acc2} instead. This is implemented as follows: λ_{core2} is dropped to the OTDM-to-WDM unit where its tributaries are simultaneously extracted by choosing the appropriate time delays in a single nonlinear optical time gate (here an EAM). The time slot to wavelength mapping is determined by arranging the delays. Here, λ_{core2} is split up and mapped as follows: $TS_1 \rightarrow \lambda_{\text{drop1}}$, $TS_2 \rightarrow \lambda_{\text{drop2}}$, $TS_3 \rightarrow \lambda_{\text{drop3}}$.

The qualities of the corresponding drop channels are 18.3 dB, 19.2 dB, and 19.8 dB, respectively (Fig. 8.3(a), point C). Channels λ_{drop1} and λ_{drop3} are subsequently mapped along with the wavelength λ_{acc2} to the WDM-to-TDM unit. It comprises three ADORE units, each unit converting one WDM channel to an OTDM tributary, by performing asynchronous retiming and pulse-width adaptation. Fixed delay lines at the output stages of the WDM-to-OTDM subsystem interleave the tributaries to form the OTDM channel, thus associating each ADORE with a certain tributary (e.g. $\lambda_{\text{drop1}} \rightarrow \text{TS}_1$, $\lambda_{\text{acc2}} \rightarrow \text{TS}_2$, $\lambda_{\text{drop3}} \rightarrow \text{TS}_3$), see Fig. 8.3(b), point D.

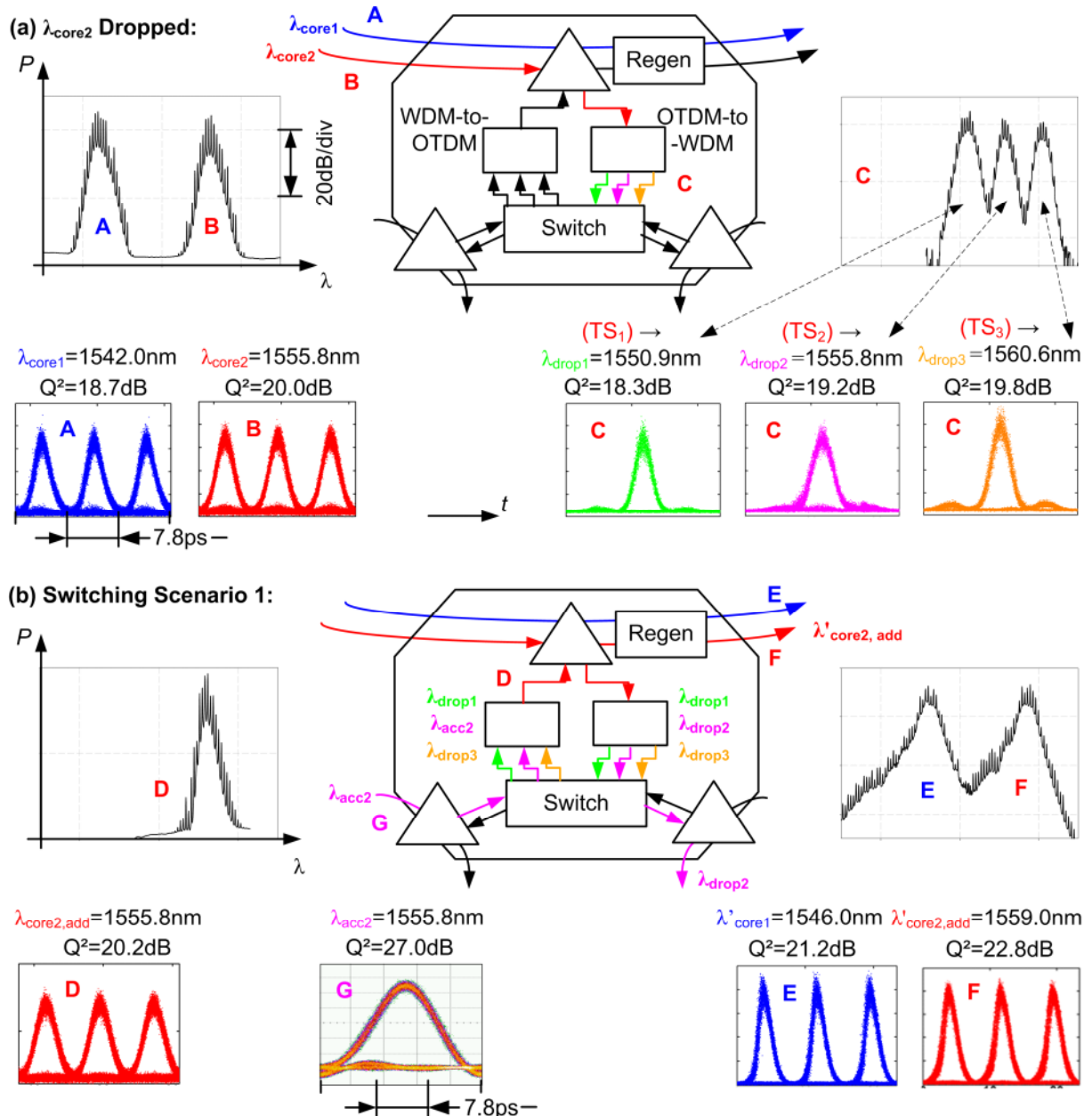


Fig. 8.3. Optical spectra, eye diagrams and Q-factors at various reference points of the setup: (a) 130 Gbit/s input signals and OTDM-to-WDM converted signal when λ_{core2} is dropped. (b) Switching scenario 1 (see also Fig. 8.2).

By reordering the WDM channel connections to the ADORE units through the MEMS switch, also TSI functionality has been obtained. The switching scenarios 2 and 3 in Fig. 8.4 show such a TSI experiment. The difference of the two scenarios is that the content of TS_1 and TS_2 is interchanged (λ_{drop2} from TS_1 to TS_2 and λ_{acc2} from TS_2 to TS_1) while TS_3 is left unchanged. This is achieved by reconfiguration of the MEMS switch. The newly formed OTDM channel $\lambda_{core2, add}$ generated by the WDM-to-OTDM subsystem has a quality of $Q^2 = 20.2$ dB for scenario 1 (Fig. 8.3(b), point D). Finally, the WSS maps both the through λ_{core1} and $\lambda_{core2, add}$ channel to the multi-wavelength regenerator subsystem. After regeneration, λ'_{core1} and $\lambda'_{core2, add}$ exhibit a Q^2 improvement of 2.5 dB and 2.6 dB, respectively, compared to their inputs A and D. The Q -factor improvement compared to the input signals is attributed mainly to the non-optimum extinction ratio of the input signals (see also eye diagrams in reference point A and D as compared to E and F in Fig. 8.3(b)).

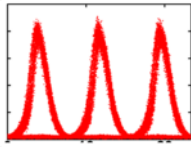
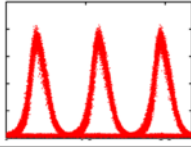
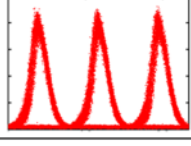
Switching Scenario	$\lambda'_{core2, add}$ Tributaries			$\lambda'_{core2, add}$ Result at F	
	TS_1	TS_2	TS_3	Q^2 [dB]	Eye Diagram
1	λ_{drop1}	λ_{acc2}	λ_{drop3}	22.8	
2	λ_{drop2}	λ_{acc2}	λ_{acc3}	22.9	
3	λ_{acc2}	λ_{drop2}	λ_{acc3}	21.4	

Fig. 8.4. Table with three switching scenarios giving time slot constellations and excellent Q -factors for the added core signal $\lambda_{core2, add}$. Note that in scenario 2 and 3, time-slots TS_1 and TS_2 are interchanged.

Significant polarization dependence was not observed, and therefore the polarization was not adjusted to optimum operation points throughout the setup. All Q -factor measurements were performed using an all-optical sampling scope (Picosolve®). Many more switching scenarios have been tested where we found similar results.

BER measurements (Fig. 8.5) support the excellent Q -values measured. For the switching scenario shown in Fig. 8.3(b) we measured the performance of the 130 Gbit/s transmitters and the corresponding outputs of the regenerator. For λ'_{core2} , both timeslots carrying the looped back $TS_1 = \lambda_{drop1}$ and the added $\lambda_{acc2} = TS_2$ showed penalties of only 2.15 dB and 2.1 dB, respectively. Comparing the BER curve slopes of λ_{core2} to $\lambda'_{core2}(\lambda_{access})$ and $\lambda'_{core2}(\lambda_{drop1})$ one can observe less steep slopes for $\lambda'_{core2}(\lambda_{access})$ and $\lambda'_{core2}(\lambda_{drop1})$. Note that both $\lambda'_{core2}(\lambda_{access})$ and $\lambda'_{core2}(\lambda_{drop1})$ traverse the WDM-to-OTDM subsystem. Similar slopes

can be found when looking at the BER curves of the WDM-to-OTDM setup in Fig. 4.5. We therefore attribute the reduced slopes of the BER curves of $\lambda'_{\text{core2}}(\lambda_{\text{access}})$ and $\lambda'_{\text{core2}}(\lambda_{\text{drop1}})$ to this penalty. Even passing through the all-optical 2R regenerator does not correct for the bit errors that occurred during the digital WDM-to-OTDM conversion. All measurements were done with a PRBS of length $2^{31}-1$.

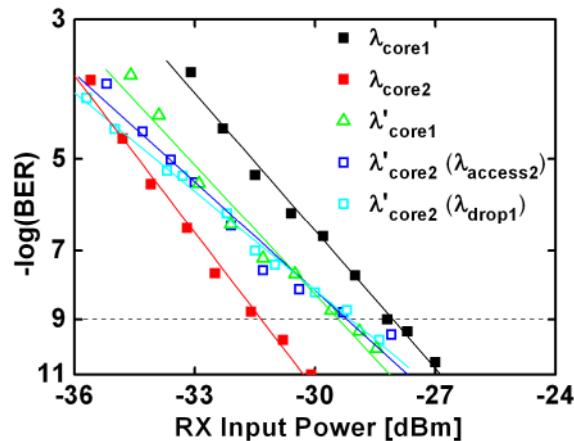


Fig. 8.5. BER measurements for switching scenario 1. All measurements were taken using an EAM performing temporal demultiplexing from 130 Gbit/s to 43 Gbit/s.

8.4 Switch Node Scalability and Cascadability

While the scalability of the various subsystems has been discussed in the respective chapters, this section discusses the scalability of the switch node in terms of channel bit-rates and port-count as well as its cascadability.

Although we presented experimental results at 130 Gbit/s, our concept is scalable to much higher bit-rates. This is because, first, the ADORE operates on tributaries. Second, the OTDM-to-WDM can be implemented with a different technique, including pulsed sources as in [81]. And third, the 2R regenerator is all-optical. Regarding the latter, we have numerically studied in [82] the scalability limit of the 2R regenerator system as the repetition rate increases. Carefully selecting the fiber and input signal parameters from the design map reported in [67] in order to achieve the same regenerative properties, it is possible to increase the repetition rate up to 640 Gbit/s without any extra degradation due to undesired cross-talk with the Rayleigh backscattered signal.

In addition, our concept provides a port-scalable solution, since it is limited only by the dimension of the MEMS switch fabric.

For example, consider a network scenario where the switch interconnects two access rings with a core ring carrying 4×130 Gbit/s signals, see Fig. 8.6. This illustrates the capability of the chosen architecture to adapt to growing capacity demands, showing that the proposed node architecture is a fully scalable node design. When upgrading to higher capacities, only bigger space switches and different DEMUX filters are needed at the OTDM-to-WDM and

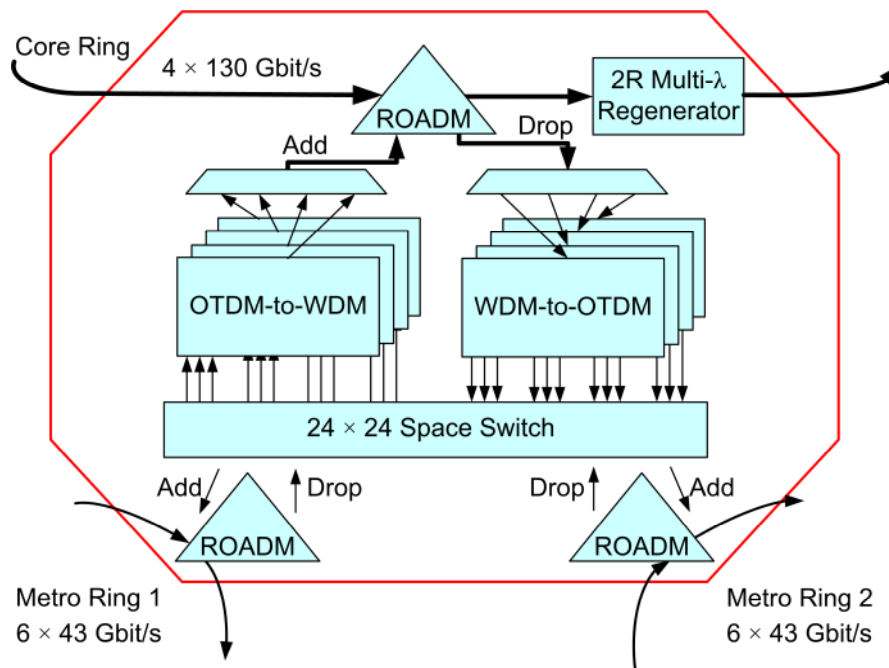


Fig. 8.6. Node architecture for a capacity scenario where the core ring carries four 130 Gbit/s OTDM channels and the metro rings carry six 43 Gbit/s channels each. The space switch with a dimension of 24×24 provides full connectivity between the core and metro rings.

WDM-to-OTDM subsystems. No performance degradation is expected due to higher channel counts.

Bursty traffic on a per-tributary basis [22] could also be supported by the conversion technologies (OTDM-to-WDM and vice-versa) presented. In this case, the MEMS switch should be replaced by a much faster switch, suitable for routing bursts. However, fast switch fabrics have limited port scalability.

In terms of cascadability of the switch node, the high speed core signals could traverse an infinite number of nodes if there is no degradation. The tributaries that are dropped and looped back undergo true 3R regeneration, the channels that are passed through are 2R regenerated and might be limited by timing jitter for long transmission distances. Note that the 2R regenerator includes offset filtering, i.e. wavelength conversion. Therefore, one needs another wavelength converter / regenerator to convert the signals back to their initial wavelengths if keeping the same signal wavelengths throughout the network is required. As a matter of fact, based on the switch node proposed in this work, a successful field trial has been presented recently [83]. Therefore, the design is likely to be realizable even for very large distances. However, studies on the statistics of jitter accumulation over ultra-long haul links would need to be done to confirm the above.

8.5 Summary

A novel optical switching node with sub-wavelength traffic grooming and multi-wavelength regenerative capabilities has been successfully demonstrated. It provides interconnection of a high bit-rate 130 Gbit/s core ring with lower bit-rate 43 Gbit/s metro rings. By using the asynchronous retiming scheme, we achieved error-free buffer-less data grooming with time-slot interchange capability for OTDM networking.

In detail, we realized the following types of connections using the space switch:

- An individual WDM channel from the OTDM-to-WDM subsystem outputs was connected to a metro ring.
- An individual WDM channel from the OTDM-to-WDM subsystem outputs was connected to an input port of the WDM-to-OTDM subsystem (loop-back). This type of connection is necessary in case that only part of the original 130 Gbit/s OTDM channel needs to be dropped to a metro ring, as the rest of it will have to be looped back.
- A metro ring channel connected to the WDM-to-OTDM subsystem (The trivial case of a metro ring channel connected directly to the other metro ring has not been presented here.).

The functionality and associated performance of the switch node that was studied include:

- Multi-wavelength regeneration at 130 Gbit/s (However, for an in-depth investigation of the regenerative capabilities of the multi-wavelength regenerator, see Section 7.1.3.).
- Time-slot interchange by rearranging the inputs of the WDM-to-OTDM subsystem.
- OTDM-to-WDM conversion of core ring channels (130 Gbit/s to 3×43 Gbit/s) and switching to the metro rings.
- Partial add/drop of one 130 Gbit/s channel: drop of one 43 Gbit/s channel from a 130 Gbit/s OTDM core channel to a metro ring. Loop back of the two remaining 43 Gbit/s channels and aggregation with one 43 Gbit/s channel from a metro ring to form, again, a 130 Gbit/s OTDM channel to be added to the core ring.

We achieved excellent Q-factor values for all switching scenarios. BER measurements with a maximum sensitivity penalty of 2.15 dB support these results. Although the demonstration was carried out at 130 Gbit/s core data rate in a back-to-back configuration, the novel switch concept is scalable to even higher bit-rates and has the potential to support networks that extend over large distances.

9 Achievements and Outlook

In this thesis, a novel optical switch node with individual OTDM channel grooming and multi-wavelength regenerative capabilities has been successfully demonstrated. It provides interconnection of high bit-rate 130 Gbit/s core rings with lower bit-rate 43 Gbit/s metro rings. Recent advances in long haul transmission and switching technology have shifted the operational and bandwidth bottleneck from the core to the metro part of the network. In Chapter 1 we have reviewed the existing metro network implementations and the key requirements for future metropolitan area networks.

The novel switch node architecture has been defined in Chapter 2. In addition, it has been discussed how this approach will potentially boost the progress in the metro networks and will match the technological leaps that have already been carried out at the backbone and the access parts of the network. Our approach does not only offer broadband access for every user but also interoperability with existing infrastructures providing a smooth migration path from existing to future infrastructures and supporting a variety of new services and applications. Innovative node subsystems were developed enabling the required node functionalities, including: all-optical multi-wavelength regenerators, all-optical OTDM-to-WDM converters with clock recovery, and opto-electronic WDM-to-OTDM converters. The proposed switch node and its subsystems were experimentally implemented and their functionality and feasibility was demonstrated – see Chapter 3 for a detailed description of the test setups.

In the following, we shortly summarize the main achievements of this thesis and develop suggestions for future research.

Opto-Electronic WDM-to-OTDM Conversion: The switch node proposed in this thesis requires retiming of multiple WDM channels and subsequent WDM-to-OTDM conversion for interconnecting 43 Gbit/s and 130 Gbit/s network rings. In Chapter 4, we successfully demonstrated for the first time asynchronous retiming in a 3×43 Gbit/s to 130 Gbit/s buffer-less WDM-to-OTDM traffic grooming experiment.

All-Optical TDM-to-WDM Conversion: Another key functionality of the switch node is mapping of an OTDM signal to different WDM channels. A practical solution requires simultaneous demultiplexing of all OTDM channels with a single device. In Chapter 5, we proposed and experimentally demonstrated two different OTDM-to-WDM conversion schemes based on highly-nonlinear fiber, which convert a 130 Gbit/s OTDM signal into three 43 Gbit/s WDM signals. Although both schemes present different advantages depending on the particular application, the approach with the simpler setup, easier operation and better long-term stability was chosen for the full switch node demonstration.

Opto-Electronic Clock Recovery: Both OTDM-to-WDM solutions require optical time gating at the tributary bit rate. Therefore we designed and demonstrated in Chapter 6 a 43 GHz

sub-harmonic optical clock recovery from 130 Gbit/s data streams, which is based on an injection-locked opto-electronic oscillator. The excellent jitter performance of the clock recovery was verified by using it in combination with the OTDM-to-WDM subsystem.

All-Optical Regeneration: In Chapter 7, we proposed three different methods for high-speed all-optical regeneration. As a first solution, we proposed a 43 Gbit/s multi-wavelength scheme for regenerating up to three 43 Gbit/s intensity-modulated channels. This technique is based on co-propagation of the channels in the fiber with a carefully designed dispersion map for reducing the nonlinear inter-channel cross-talk.

As a second solution, a bi-directional scheme was exploited to demonstrate the simultaneous regeneration of two 130 Gbit/s intensity-modulated channels. This represents the highest speed dual-channel regenerator ever reported in a single fiber and was made possible by a very careful choice of the HNLF parameters.

Offering improved sensitivity and robustness to nonlinear impairments as compared to pure intensity modulation, differential phase shift keying is becoming another modulation format of choice for future networks. Therefore, in the last section of the chapter we proposed and successfully demonstrated a novel semiconductor optical amplifier-based interferometric wavelength converter and regenerator for differentially phase-modulated signals.

Switch Node System Demonstration: After introducing and experimentally characterizing all switch node subsystems, the challenge was to bring all the different optical technologies onto a common wavelength grid, assemble the optical switch node with its functionalities and perform testing at bit-rates of 43 Gbit/s and 130 Gbit/s. Chapter 8 reported the results of the back-to-back (without fiber transmission) lab demonstration with multiplexing in frequency and time. The excellent performance of the proposed solution is verified by studying a multiple of switching scenarios, showing dynamic bandwidth allocation for time-varying traffic demands. However, further challenges of optical transmission of ultra-high bit-rate signals in dynamic networks will require thoughtful consideration. Recently, a field trial of the novel switch node recently demonstrated its feasibility (C35).

The high number of components required in the demonstrator makes photonic integration essential for commercial viability. One key to the success of this demonstration was the exploitation of nonlinearities in HNLF. An alternative approach could be the use of short silicon-organic hybrid slot waveguides with a record nonlinearity coefficient of $\gamma \approx 1 \times 10^5 W^{-1} km^{-1}$ (J7, C28, C26, C18). In view of the potential for improving fiber-chip coupling and waveguide loss, this technology could be key for offering higher bandwidth and less power consuming subsystems in the future.

This work was supported by the European projects TRIUMPH (grant IST-027638 STP) and in part by Euro-Fos (NoE 224402) and the Science Foundation Ireland (grant 06/IN/1969).

Appendix

A 1 Methods for System Performance Characterization

In this chapter, we discuss the methods for system performance characterization that are used in this thesis.

A 1.1 Bit-Error Ratio Measurements

For a standard bit-error ratio (*BER*) measurement, the signal at the receiver input is additionally degraded by adding various amounts of noise. Normally, the error ratio is plotted as a function of total average received power. This measurement technique is widely used in this work.

The principle gradient of an ideal receiver (quantum limited: no thermal noise, no dark current, and 100 % quantum efficiency) is given by an exponential dependence. The temporal photon distribution of a laser obeys a Poisson-distribution [26]. The probability of detecting n photons is given by

$$p_n(N) = \frac{N^n}{n!} \exp(-N) \quad (\text{A.1})$$

with an average number of photons N in each “1” bit, which are proportional to the received power P_{rec} . In case of an ideal receiver, an error is made only if a “1” bit fails to produce even a single electron-hole pair. The BER is then given by the probability $p_0(N) = \exp(-N)$.

With $BER \sim p_n(N)$ and $P_{\text{rec}} \sim N$, we obtain a theoretical gradient

$$BER \sim \exp(-N). \quad (\text{A.2})$$

When plotting the error ratio on a logarithmic scale as a function of the received power ($\log(BER)$ over P_{rec} in mW) a straight line is expected. If in addition the logarithm of the power is taken (in dBm), also the y-axis has to be logarithmized for still obtaining a straight line. In Fig. A.1 (taken from [27]), the respective left hand side curves illustrate such theoretical characteristic. In case of more realistic assumptions (in an experiment) one

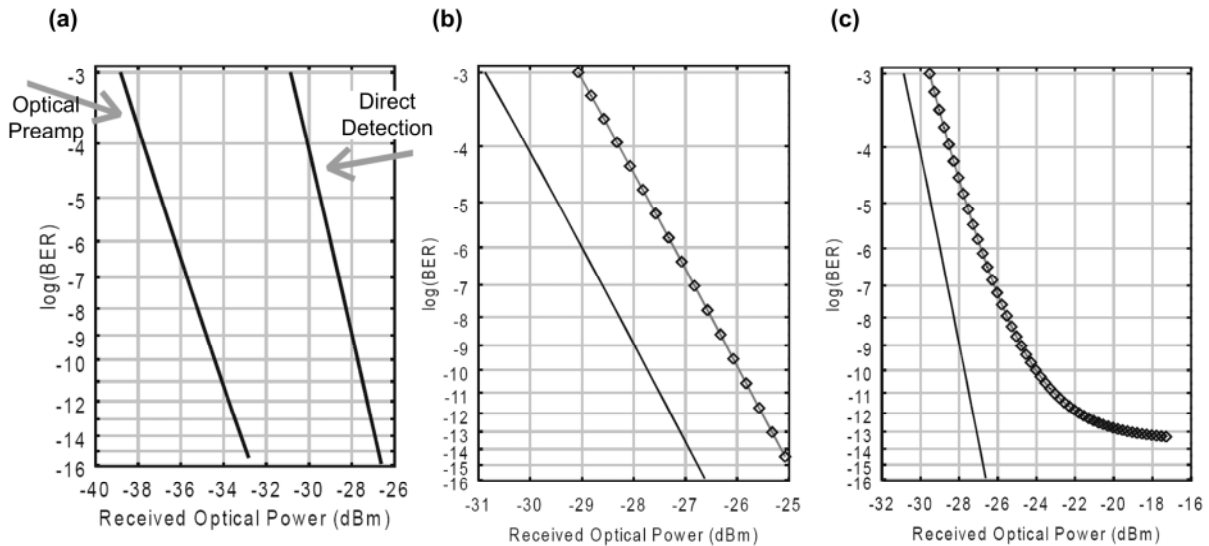


Fig. A.1. Possible differences when comparing two bit error ratio curves (simulated curves taken from [27]). (a) Different noise distributions, (b) additional power without information, (c) additive noise prior to the receiver.

finds a deviation from this theoretical characteristic, see respective right hand side curves in Fig. A.1.

Fig. A.1(a) shows BER curves with different gradients. Such behavior points towards different noise distributions. The left hand side curve shows an optically preamplified receiver with non-Gaussian distributed noise [84]. The right hand side curve shows the non-preamplified direct detection with Gaussian distributed noise.

Fig. A.1(b) shows two BER curves that are shifted in parallel (the difference in power is called receiver penalty or sensitivity penalty). Such an effect is due to additional measured power that does not contribute to the BER. Typical examples are a reduced extinction ratio (of the modulator in case of OOK, or of the optical switch for demultiplexing, also called DEMUX penalty) or ASE noise that is measured.

Finally, Fig. A.1(c) shows the case where the signal is degraded due to additive noise before reaching the receiver (a signal with reduced OSNR). For low received power, one finds a parallel shift, since the power of the additive noise is measured as part of the received power. For higher received power the error ratio saturates such that even when further increasing the power the error ratio does not improve. This is due to the fact that the OSNR was degraded prior to entering the receiver. Consequently, the power can be increased to arbitrary values without improving the OSNR. Such a base error ratio is called “error floor”.

A 1.2 Q-Factor Measurements

The quality factor, or Q -factor, is a parameter that is closely related to the quality of the transmitted optical signal in terms of signal-to-noise ratio (SNR) and BER . For intensity modulated signals it is defined as the ratio of the difference, after observing a large number of 1/0 symbols, of mean values for 1 and for 0 symbols ($\mu_1 - \mu_0$) and the difference of standard deviations for 1 and for 0 symbols ($\sigma_1 - \sigma_0$):

$$Q = (|\mu_1 - \mu_0|) / (|\sigma_1 - \sigma_0|). \quad (\text{A.3})$$

Then, the BER can be calculated

$$BER = \frac{1}{2} \operatorname{erfc}(Q/\sqrt{2}) \quad (\text{A.4})$$

where the function erfc is the complementary error function.

However, note that the relationship of Q -factor and BER only holds for additive Gaussian noise, equal probabilities for both 1 and 0 symbols being send, and that the receiver decision threshold is set to the optimum value. A detailed discussion of the relation between Q -factor, SNR and BER can be found in [26], [28].

In this context note that all-optical regenerators change the probability density functions of the noise of the regenerated signals.

Therefore, in the experiments where optical regenerators are involved, it is not possible to directly relate Q -factor values and BER values and Eq. (A.4) does not hold. However, even though Q -factor values may not be directly related to the BER , their evolution before and after a regeneration scheme gives an idea of the performance of the scheme.

For example, a bit error ratio of $BER = 10^{-9}$ corresponds to a linear Q -factor of $Q|_{lin} = 6.0$ and accordingly to $Q^2|_{dB} = 15.6dB$ with

$$Q^2|_{dB} = 20 \cdot \log Q|_{lin}. \quad (\text{A.5})$$

In modern optical networks, data communication with a $BER < 10^{-9}$ is considered “error free”.

Measurement Technique

One standard way of measuring the Q -factor of a signal is by measuring the standard deviations and mean values of the logic 1 bits and 0 bits in the eye diagram. The “eye diagram” is the superposition of bit periods on an oscilloscope. This method is used for Q -factor measurements in this thesis. For a detailed discussion of the method refer for example to [28].

A 2 Fiber Nonlinearities

Nonlinear effects in fiber can be both harmful and beneficial depending on the application. For example, on one hand, optical transmission fibers need to have low nonlinearity to suppress waveform distortion and channel crosstalk, while, on the other hand, optical fibers for signal processing are required to have high nonlinearity to realize effective nonlinear functionalities. Self-phase modulation (SPM) and cross-phase modulation (XPM) effects can limit the performance of a generic WDM system, but, at the same time, they are used for applications such as 2R regeneration in Mamyshev-type schemes and OTDM-to-WDM conversion.

In this section, we briefly discuss the physical origin of fiber nonlinearity and introduce the nonlinear phenomena known as SPM and XPM. The discussion in this section is based on [85], pp. 64-65.

A 2.1 Nonlinear Phase Modulation

The nonlinear behaviour of optical fibers at high intensities stems from the power dependence of their refractive index. The physical origin of this effect lies in the anharmonic response of electrons to optical fields, resulting in a nonlinear susceptibility. To model nonlinear refraction, we write the core and cladding indices of silica fiber as [85]

$$n'_j = n_j + \bar{n}_2 \left(P / A_{\text{eff}} \right), \quad j = 1, 2, \quad (\text{A.6})$$

where \bar{n}_2 is the nonlinear-index coefficient, P is the optical power, and A_{eff} is the effective mode area of the fiber.

A 2.2 Self-Phase Modulation

Using first-order perturbation theory to see how fiber modes are affected by the nonlinear term in Eq. (A.6), we find that the mode shape does not change but the propagation constant β becomes power dependent. It can be written as [85]

$$\beta' = \beta + k_0 \bar{n}_2 P / A_{\text{eff}} \equiv \beta + \gamma P, \quad (\text{A.7})$$

where $\gamma = 2\pi \bar{n}_2 / (A_{\text{eff}} \lambda)$ is an important nonlinear parameter and k_0 the free-space wave-number. Knowing that the optical phase increases linearly with propagation in z -direction, the γ term produces an additional nonlinear phase shift given by [85]:

$$\phi_{NL} = \int_0^L (\beta' - \beta) dz = \int_0^L \gamma P(z) dz = \gamma P_{\text{in}} L_{\text{eff}}, \quad (\text{A.8})$$

where $P(z) = P_{\text{in}} \exp(-\alpha z)$ accounts for the fiber loss (with α representing the fiber loss) and L_{eff} is defined as

$$L_{eff} = [1 - \exp(-\alpha L)] / \alpha . \quad (\text{A.9})$$

Since this nonlinear phase modulation is self-induced, the non-linear phenomenon responsible for it is called self-phase modulation.

A 2.3 Cross-Phase Modulation

The intensity dependence of the refractive index in Eq. (A.6) can also lead to another nonlinear phenomenon known as cross-phase modulation. It occurs when two or more optical channels are transmitted simultaneously inside an optical fiber using WDM. In that case, the nonlinear phase shift for a specific channel depends not only on the power of that channel but also on the power of all other channels. The phase shift for the j th channel becomes [85]

$$\phi_j^{NL} = \gamma L_{eff} \left(P_j + 2 \sum_{m \neq j} P_m \right), \quad (\text{A.10})$$

where the sum extends over the number of channels. It is clear that the total phase shift depends on the powers in all channels and varies from bit to bit depending on the bit pattern of the other channels. The factor of 2 in Eq. (A.10) has its origin in the form of the nonlinear susceptibility [42] and indicates that XPM is twice as effective as SPM for the same amount of power.

Glossary

Acronyms

2R	reamplification and reshaping
3R	reamplification, reshaping, and retiming
ADM	add-drop multiplexer
ADORE	asynchronous optical regenerator
AMP	RF amplifier
ASE	amplified spontaneous emission
ASK	amplitude shift keying
ATT	attenuator
AWG	arrayed waveguide grating
B-to-B	back-to-back
BER	bit-error ratio
BP	band-pass filter
CO	central office
C-band	centre wavelength band
CLK	clock
CRU	clock recovery unit
CW	continuous wave
CS	carrier suppressed
DC	direct current
DCA	digital communication analyzer
DCF	dispersion compensating fiber
DEMUX	demultiplexer
DFB	distributed feedback laser
DI	delay interferometer
DL	delay line
DPSK	differential phase shift keying
DSL	digital subscriber line
DXC	digital cross-connect
EAM	electro-absorption modulator
ED	error detector
EDFA	Erbium-doped fiber amplifier
FITL	fiber in the loop
FREAG	frequency resolved electro-absorption gating
FTTx	fiber to the „x“ (h - home, b- building, etc.)
FWHM	full width at half maximum

FWM	four-wave mixing
GbE	1 Gbit/s Ethernet
HNLF	highly-nonlinear fiber
HP	high power
IPTV	internet protocol television
LAN	local area network
LD	laser diode
MAN	metropolitan area network
MEMS	micro-electro-mechanical system
MLL	mode-locked laser
MOD	modulator
MUX	multiplexer
MZI	Mach-Zehnder interferometer
MZM	Mach-Zehnder modulator
NOLM	nonlinear optical loop mirror
NWA	network analyzer
OADM	optical add-drop multiplexer
OBPS	optical band-pass filter
ODL	optical delay line
OEO	opto-electronic-optical
OOK	on-off keying
OPEX	operational expenditure
OSA	optical spectrum analyzer
OTDM	optical time-division multiplexing
OUT	optical transport unit
OXC	optical cross-connect
PC	polarization controller
PDL	polarization dependent loss
PMD	polarization mode dispersion
RMS	root-mean-square
ROADM	reconfigurable optical add-drop multiplexer
POL	polarizer
RZ	return-to-zero
PD	photo diode
PGDD	periodic-group-delay devices
PM	power monitor
PPG	pulse pattern generator
PRBS	pseudo-random bit sequence
PS	phase shifter
RF	radio frequency
RX	receiver
SA	spectrum analyzer
SDH	synchronous digital hierarchy

SMF	single-mode fiber
SOA	semiconductor optical amplifier
SONET	synchronous optical networking
SPM	self-phase modulation
TDM	time-division multiplexing
TE	transverse electric
TF	transfer function
TM	transverse magnetic
TP	twisted pair
TS(I)	time slot (interchange)
TX	transmitter
ULH	ultra-long haul
UNI	user/network interface
VOA	variable optical attenuator
VoIP	voice over IP
WAN	wide area network
WDM	wavelength division multiplexing
XC	cross connect
XPM	cross-phase modulation

Symbols

Greek Symbols

α	power attenuation coefficient, unit m^{-1}
β	propagation constant, unit m^{-1} , Eq. (8.7)
γ	nonlinear parameter, unit $1/(\text{W km})$, Eq. (8.7)
$\Delta\phi$	optical phase shift in MZI, Eq. (3.2)
λ	wavelength, unit m
λ_L	local optical oscillator wavelength, unit m
ϕ_{NL}	nonlinear phase shift, Eq. (8.8)
μ_1, μ_2	mean value of noise distribution, Eq. (8.3)
ν_I	injected signal into oscillator, Eq. (6.1)
ν_0	steady state output of oscillator, Eq. (6.1)
σ_1, σ_2	standard deviation of noise distribution, Eq. (8.3)
σ_{RMS}	root-mean-square timing jitter, unit s
τ	FWHM pulse width, unit s
ν_A, ν_B	signals at different positions of the oscillator
ϕ	optical phase
ω_N	natural oscillator frequency, unit Hz
ω_N	incoming frequency at the oscillator input, unit Hz
ω	angular frequency, $\omega = 2\pi f$, unit $1 / \text{s}$

Latin Symbols

A_{eff}	effective mode area of fiber, unit m^2 , Eq. (8.6)
BW	bandwidth, unit Hz
C	first order dispersion, unit $\text{ps} / (\text{km nm})$, Eq. (3.1)
c_0	vacuum light speed, $c_0 = 2.99792 \times 10^8 \text{ m} / \text{s}$
C_λ	chromatic dispersion factor, Eq. (3.1)
C_m	gain of $f(\nu_0)$, Eq. (6.12)
D	second order dispersion (dispersion slope), unit $\text{ps} / (\text{km nm}^2)$, Eq. (3.1)
\mathbf{E}	electrical field vector, unit V / m
f_c	centre frequency, unit Hz
f_{clk}	clock frequency, unit Hz
f_L	local clock frequency, unit Hz
f_{control}	control pulse repetition rate, unit Hz, Eq. (5.5)
F	noise figure
F_0	fundamental oscillator frequency (free spectral range), unit Hz

g	switching granularity, Eq. (1.1)
G	gain
$H(j\omega)$	transfer function, Eq. (6.1)
$IBRPN$	input bit-rate referred phase noise, Eq. (6.23)
k_0	free-space wave-number, unit m^{-1} , Eq. (8.7)
L_{eff}	effective interaction length, unit m, Eq. (8.9)
L	length, unit m
M	order of oscillation mode, Eq. (6.20)
N	average number of photons, Eq. (8.1)
n_g	group refractive index, Eq. (3.7)
\bar{n}_2	nonlinear-index coefficient, Eq. (8.6)
n'_j	nonlinear refractive index, Eq. (8.6)
P	optical power, unit W
$P_{0, \text{control}}$	control peak power, unit W, Eq. (5.5)
$P_{-1\text{dB}}$	1dB gain compression input power, unit W
P_{CW}	optical CW power, unit W
P_{data}	average optical data power, unit W
P_{in}	average optical input power, unit W, Eq. (3.4)
p_n	propability of detecting n photons, Eq. (8.1)
P_{out}	average optical output power, unit W, Eq. (3.4)
P_{rec}	received power, unit W, Eq. (8.2)
P_{sat}	saturation output power, unit W
P_{sens}	minimum required receiver input power for a BER = 10^{-9}
Q	signal quality parameter, Eq. (8.3)
Q_{filter}	filter quality factor
V_{MZM}	total drive voltage of MZM, unit V, Eq. (3.2)
V_{bias}	static part of drive voltage of MZM, unit V, Eq. (3.2)
$S_\phi(f)$	phase noise power spectral density, unit W / Hz, Eq. (6.21)
SSG	small signal gain
T	bit period, unit s
T_d	time delay, unit s
T_{MZM}	transfer function of MZM, Eq. (3.6)
T_{NOLM}	transmittance of NOLM, Eq. (5.1)
V_π	voltage needed for a phase swing of π in MZM arm, unit V
V_{gr}	group velocity, unit m / s, Eq. (3.7)
V_{NRZ}	dynamic part of MZM drive voltage (electrical NRZ sequence), unit V, Eq. (3.2)
V_O	output amplitude of the oscillator, Eq. (6.9)
$V_{\text{p-p}}$	peak-to-peak voltage, unit V
W	walk-off parameter, unit s / m, Eq. (5.4)

Bibliography

- [1] I. P. Kaminow and T. Li, eds., *Optical Fiber Telecommunications IV: B. Systems and Impairments*. Academic Press, 2002.
- [2] R. Dutta, A. Kamal, and G. Rouskas, *Traffic Grooming for Optical Networks*. Springer, 2008.
- [3] A. A. M. Saleh and J. M. Simmons, “Evolution toward the next-generation core optical network,” *J. Lightw. Technol.*, vol. 24, pp. 3303–3321, 2006.
- [4] P. V. Mamyshev, “All-optical data regeneration based on self-phase modulation effect,” in *Proc. ECOC 1998*, vol. 1, pp. 475–476, 1998.
- [5] A. H. Gnauck, G. Raybon, S. Chandrasekhar, J. Leuthold, C. Doerr, L. Stulz, A. Agarwal, S. Banerjee, D. Grosz, S. Hunsche, A. Kung, A. Marhelyuk, D. Maywar, M. Movassaghi, X. Liu, C. Xu, X. Wei, and D. M. Gill, “2.5 Tb/s (64×42.7 Gb/s) transmission over 40×100 km NZDSF using RZ-DPSK format and all-Raman-amplified spans,” in *Proc. OFC 2002*, postdeadline paper FC2, 2002.
- [6] M. Sexton and A. Reid, *Transmission Networking: SONET and the Synchronous Digital Hierarchy*. Artech House, Boston, 1992.
- [7] J. Leuthold, *Optische Kommunikations-Systeme*. Institute of Photonics and Quantum Electronics, Karlsruhe, Germany, 2009. Lecture notes.
- [8] S. Kartalopoulos, *DWDM Networks, Devices and Technology*. Wiley Interscience, 2003.
- [9] J. Livas, “Optical transmission evolution: From digital to analog to? network tradeoffs between optical transparency and reduced regeneration cost,” *J. Lightw. Technol.*, vol. 23, no. 1, pp. 219–224, 2005.
- [10] O. Leclerc, “Towards transparent optical networks: still some challenges ahead,” in *Proc. Annual Meeting LEOS 2005*, pp. 418–419, 2005.
- [11] M. Zirngibl, *Optical Fiber Telecommunications IVA, Components*. Academic Press, 2002.
- [12] I. Redpath, D. Cooperson, and R. Kline, “Metro WDM networks develop an edge,” in *Proc. OFC 2006*, paper NThC1, 2006.
- [13] G. Finnie, “European FTTH forecast, 2008-2013,” in *Proc. FTTH Council Conference*, 2009.

- [14] J. Baliga, R. Ayre, K. Hinton, and R. S. Tucker, "Photonic switching and the energy bottleneck," in *Proc. Photonics in Switching*, pp. 125–126, 2007.
- [15] S. Namiki, T. Hasama, M. Mori, M. Watanabe, and H. Ishikawa, "Dynamic optical path switching for ultra-low energy consumption and its enabling device technologies," in *Proc. International Symposium on Applications and the Internet SAINT 2008*, pp. 393–396, 2008.
- [16] A. Gladisch, R. P. Braun, D. Breuer, A. Ehrhardt, H. M. Foisel, M. Jaeger, R. Leppla, M. Schneiders, S. Vorbeck, W. Weiershausen, and F. J. Westphal, "Evolution of terrestrial optical system and core network architecture," in *Proc. of the IEEE*, vol. 94, pp. 869–891, 2006.
- [17] S. J. B. Yoo, "Optical packet and burst switching technologies for the future photonic internet," *J. Lightw. Technol.*, vol. 24, pp. 4468–4492, 2006.
- [18] A. Shacham, B. Small, O. Liboiron-Ladouceur, and K. Bergman, "A fully implemented 12×12 data vortex optical packet switching interconnection network," *J. Lightw. Technol.*, vol. 23, pp. 3066–3075, 2005.
- [19] F. Arecco, F. Casella, E. Iannone, A. Mariconda, S. Merli, F. Pozzi, and F. Veghini, "A transparent, all-optical, metropolitan network experiment in a field environment: the "PROMETEO" self-healing ring," *J. Lightw. Technol.*, vol. 15, pp. 2206–2213, 1997.
- [20] P. Vorreau, D. Hillerkuss, F. Parmigiani, S. Sygletos, R. Bonk, P. Petropoulos, D. Richardson, G. Zarris, D. Simeonidou, D. Klionidis, I. Tomkos, R. Weerasuriya, S. Ibrahim, A. Ellis, R. Morais, P. Monteiro, S. Ben Ezra, S. Tsadka, W. Freude, and J. Leuthold, "2R/3R optical grooming switch with time-slot interchange," in *Proc. ECOC 2008*, paper Th.3.F.4, 2008.
- [21] J. Leuthold, W. Freude, S. Sygletos, P. Vorreau, R. Bonk, D. Hillerkuss, I. Tomkos, A. Tzanakaki, C. Kouloumentas, D. J. Richardson, P. Petropoulos, F. Parmigiani, A. Ellis, D. Cotter, S. Ibrahim, and R. Weerasuriya, "An all-optical grooming switch to interconnect access and metro ring networks," in *Proc. ICTON 2008*, paper We.C3.4, 2008.
- [22] A. D. Ellis, D. Cotter, S. Ibrahim, R. Weerasuriya, C. W. Chow, J. Leuthold, W. Freude, S. Sygletos, P. Vorreau, R. Bonk, D. Hillerkuss, I. Tomkos, A. Tzanakaki, C. Kouloumentas, D. J. Richardson, P. Petropoulos, F. Parmigiani, G. Zarris, and D. Simeonidou, "Optical interconnection of core and metro networks [invited]," *J. Opt. Netw.*, vol. 7, pp. 928–935, 2008.
- [23] A. Ellis, T. Widdowson, I. Phillips, and W. Pender, "High speed OTDM networks employing electro-optic modulators," *IEICE Transactions on Electronics*, vol. E81-C, pp. 1301–1308, 1998.
- [24] D. Cotter and A. D. Ellis, "Asynchronous digital optical regeneration and networks," *J. Lightw. Technol.*, vol. 16, pp. 2068–2080, 1998.

- [25] B. Mukherjee, C. Ou, H. Zhu, K. Zhu, N. Singhal, and S. Yao, "Traffic grooming in mesh optical networks," in *Proc. OFC 2004*, paper ThG1, 2004.
- [26] W. Freude, *Optische Empfänger und Fehlerwahrscheinlichkeit*. Institute of Photonics and Quantum Electronics, Karlsruhe, Germany, 2009. Lecture notes.
- [27] M. Summerfield, "Minding your BER's and Q's." Seminar Slides/ Internet, 1999. <http://www.ee.unimelb.edu.au/staff/kaic/PRL-TS/sm1-bnq.pdf>
- [28] S. Kartalopoulos, *Optical Bit Error Rate*. Wiley-IEEE Press, 2004.
- [29] S. K. Ibrahim, R. Weerasuriya, D. Hillerkuss, G. Zarris, D. Simeonidou, J. Leuthold, D. Cotter, and A. Ellis, "Experimental demonstration of 42.6 gbit/s asynchronous digital optical regenerators," in *Proc. ICTON 2008*, paper We.C3.3, pp. 203–206, 2008 (invited).
- [30] S. K. Ibrahim, D. Hillerkuss, R. Weerasuriya, G. Zarris, D. Simeonidou, J. Leuthold, and A. D. Ellis, "Novel 42.65 gbit/s dual gate asynchronous digital optical regenerator using a single mzm," in *Proc. ECOC 2008*, paper Tu4.D.3, 2008.
- [31] G. Zarris, P. Vorreau, D. Hillerkuss, S. K. Ibrahim, R. Weerasuriya, A. D. Ellis, J. Leuthold, and D. Simeonidou, "Wdm-to-otdm traffic grooming by means of asynchronous retiming," in *Proc. OFC 2009*, paper OThJ6, 2009.
- [32] P. Vorreau, S. Sygletos, F. Parmigiani, D. Hillerkuss, R. Bonk, P. Petropoulos, D. J. Richardson, G. Zarris, D. Simeonidou, D. Klonidis, I. Tomkos, R. Weerasuriya, S. Ibrahim, A. D. Ellis, D. Cotter, R. Morais, P. Monteiro, S. B. Ezra, S. Tsadka, W. Freude, and J. Leuthold, "Optical grooming switch with regenerative functionality for transparent interconnection of networks," *Optics Express*, vol. 17, pp. 15173–15185, 2009.
- [33] J. F. DeNatale, R. L. Borwick, C. Tsai, P. A. Stupar, Y. Lin, R. A. Newgard, R. W. Berquist, and M. Zhu, "Compact, low-power chip-scale atomic clock," in *Proc. IEEE/ION Position, Location and Navigation Symposium*, pp. 67–70, 2008.
- [34] F. K. Y. Awaji, T. Miyazaki, "160/4x40Gb/s OTDM/WDM Conversion Using FWM Fibre," in *Proc. ECOC 2004*, paper We1.5.6, 2004.
- [35] H. Sotobayashi and W. Chujo, "Photonic gateway: TDM-to-WDM-to-TDM conversion and reconversion at 40 Gbit/s (4 channels x 10 Gbits/s)," *Opt. Soc. Am. B*, vol. 19, pp. 2810–2816, 2002.
- [36] T. M. S. K. K. Uchiyama, H. Takara and M. Saruwatari, "100Gbit/s multiple-channel output all-optical demultiplexing based on TDM-WDM optical demultiplexing based on TDM-WDM conversion in a nonlinear optical loop mirror," *Electron. Lett.*, vol. 32, pp. 1989–1991, 1996.
- [37] S. K. K. Uchiyama and M. Saruwatari, "Multiple-channel output all-optical OTDM demultiplexer using XPM-induced chirp compensation (MONIX)," *Electron. Lett.*, vol. 34, pp. 575–576, 1998.

- [38] P. J. Almeida, P. Petropoulos, F. Parmigiani, M. Ibsen, and D. J. Richardson, "OTDM add-drop multiplexer based on time-frequency signal processing," *J. Lightw. Technol.*, vol. 24, pp. 2720–2732, 2006.
- [39] P. Vorreau, F. Parmigiani, K. Mukasa, M. Ibsen, P. Petropoulos, D. J. Richardson, A. Ellis, W. Freude, and J. Leuthold, "TDM-to-WDM conversion from 130 Gbit/s to 3×43 Gbit/s using XPM in a NOLM switch," in *Proc. ICTON 2008*, PDP Th.PD.1, 2008.
- [40] R. Morais, R. Meleiro, P. Monteiro, and P. Marques, "OTDM-to-WDM Conversion based on Wavelength Conversion and Time Gating in a Single Optical Gate," in *Proc. OFC 2008*, paper OTuD5, 2008.
- [41] N. J. Doran and D. Wood, "Nonlinear-optical loop mirror," *Opt. Lett.*, vol. 13, pp. 56–58, 1988.
- [42] G. P. Agrawal, *Nonlinear Fiber Optics*. Academic Press, 2001.
- [43] A. Bogoni, M. Scaffardi, P. Ghelfi, and L. Poti, "Nonlinear optical loop mirrors: investigation solution and experimental validation for undesirable counterpropagating effects in all-optical signal processing," *J. Sel. Top. in Quantum Electron.*, vol. 10, pp. 1115–1123, 2004.
- [44] J. Lasri, P. Devgan, R. Tang, and P. Kumar, "Ultralow timing jitter 40-Gb/s clock recovery using a self-starting optoelectronic oscillator," *Photon. Technol. Lett.*, vol. 16, pp. 263–265, 2004.
- [45] F. Cisternino and R. Girardi, "A novel approach to pre-scaled clock recovery in OTDM systems," in *Proc. ECOC 1998*, vol. 1, pp. 477–478, 1998.
- [46] H. Tsuchida and M. Suzuki, "40-Gb/s optical clock recovery using an injection-locked optoelectronic oscillator," *Photon. Technol. Lett., IEEE*, vol. 17, pp. 211–213, 2005.
- [47] H. Tsuchida, "40-GHz subharmonic optical clock recovery using an injection-locked optoelectronic oscillator," *IEICE Electron. Express*, vol. 3, pp. 373–378, 2006.
- [48] K. Fujii, "Development of an Ultra High-Speed Optical Signal Processing Technology," OKI Technical Review, vol. 72, pp. 70-75, 2005.
- [49] M. Kagawa, H. Murai, H. Tsuji, and K. Fujii, "160 Gbit/s OTDM channel identification using optical phase index with 40 Gbit/s clock recovery circuit," in *Proc. ECOC 2005*, paper We3.2.4, 2005.
- [50] R. Adler, "A study of locking phenomena in oscillators," in *Proc. IRE*, vol. 34, pp. 351–357, 1946.
- [51] D. Sommer and N. Gomes, "Wide-locking bandwidth optically injection-locked oscillators: S-parameter design and modulation effects," *IEEE Trans. Microw. Theory Tech.*, vol. 43, pp. 1424–1434, 1995.
- [52] X. Wang and N. Gomes, "Locking bandwidth equations for electrically and optically injection-locked oscillators," *IEE Optoelectronics*, vol. 151, pp. 476–481, 2004.

- [53] S. Verma, H. Rategh, and T. Lee, "A unified model for injection-locked frequency dividers," *Solid-State Circuits, IEEE Journal of*, vol. 38, pp. 1015–1027, June 2003.
- [54] H. Mulvad, E. Tangdiongga, O. Raz, J. Herrera, H. de Waardt, and H. Dorren, "640 Gbit/s OTDM lab-transmission and 320 Gbit/s field-transmission with SOA-based clock recovery," in *Proc. OFC 2008*, paper OWS2, 2008.
- [55] J. Leuthold, J. Wang, T. Vallaitis, C. Koos, R. Bonk, A. Marculescu, P. Vorreau, S. Sygletos, and W. Freude, "New approaches to perform all-optical signal regeneration," in *Proc. ICTON 2007*, paper We.D2.1, 2007.
- [56] C. Nuzman, J. Leuthold, R. Ryf, S. Chandrasekhar, C. R. Giles, and D. T. Neilson, "Design and implementation of wavelength-flexible network nodes," *J. Lightw. Technol.* vol. 21, pp. 648–663, 2003.
- [57] L. Provost, F. Parmigiani, P. Petropoulos, and D. Richardson, "Investigation of simultaneous 2R regeneration of two 40-Gb/s channels in a single optical fiber," *Photon. Technol. Lett.*, vol. 20, pp. 270–272, 2008.
- [58] M. Vasilyev and T. I. Lakoba, "All-optical multichannel 2R regeneration in a fiber-based device," *Opt. Lett.*, vol. 30, pp. 1458–1460, 2005.
- [59] I. Tomkos, C. Kouloumentas, and S. Tsolakidis, "Performance studies of multi-wavelength all-optical 2R regeneration subsystems based on highly non-linear fibers," in *Proc. ICTON 2007*, paper Tu.C1.1, 2007.
- [60] M. Vasilyev, T. Lakoba, and P. Patki, "Multi-wavelength all-optical regeneration," in *Proc. OFC 2008*, paper OWK3, 2008.
- [61] L. Provost, C. Kouloumentas, F. Parmigiani, S. Tsolakidis, I. Tomkos, P. Petropoulos, and D. Richardson, "Experimental investigation of a dispersion-managed multi-channel 2R optical regenerator," in *Proc. OFC 2008*, paper OThJ3, 2008.
- [62] P. Vorreau, C. Kouloumentas, L. Provost, I. Tomkos, W. Freude, and J. Leuthold, "Simultaneous processing of 43 Gb/s WDM channels by a fiber-based dispersion-managed 2R regenerator," in *Proc. ECOC 2008*, paper Th.1.B.3, 2008.
- [63] C. Kouloumentas, P. Vorreau, L. Provost, P. Petropoulos, W. Freude, J. Leuthold, and I. Tomkos, "All-fiberized dispersion-managed multichannel regeneration at 43 Gb/s," *Photon. Technol. Lett.*, vol. 20, pp. 1854–1856, 2008.
- [64] T. Ohara, H. Takara, S. Kawanishi, T. Yamada, and M. M. Fejer, "160-Gb/s all-optical limiter based on spectrally filtered optical solitons," in *Proc. OFC 2004*, paper WN3, 2004.
- [65] T. I. Lakoba and M. Vasilyev, "A new robust regime for a dispersion-managed multichannel 2R regenerator," *Opt. Express*, vol. 15, pp. 10061–10074, 2007.
- [66] D. V. Kuksenkov, S. Li, M. Sauer, and D. A. Nolan, "Nonlinear fibre devices operating on multiple WDM channels," in *Proc. ECOC 2005*, paper Mo3.5.1, 2005.

- [67] L. A. Provost, C. Finot, P. Petropoulos, K. Mukasa, and D. J. Richardson, "Design scaling rules for 2R-optical self-phase modulation-based regenerators," *Opt. Express*, vol. 15, pp. 5100–5113, 2007.
- [68] F. Parmigiani, P. Vorreau, L. A. Provost, K. Mukasa, M. Takahashi, M. Tadakuma, P. Petropoulos, D. J. Richardson, W. Freude, and J. Leuthold, "2R regeneration of two 130 Gbit/s channels within a single fiber," in *Proc. OFC 2009*, paper JThA56, 2009.
- [69] P. A. Andersen, T. Tokle, Y. Geng, C. Peucheret, and P. Jeppesen, "Wavelength conversion of a 40-Gb/s RZ-DPSK signal using four-wave mixing in a dispersion-flattened highly nonlinear photonic crystal fiber," *Photon. Technol. Lett.*, vol. 17, pp. 1908–1910, 2005.
- [70] K. Croussore, C. Kim, and G. Li, "All-optical regeneration of differential phase-shift keying signals based on phase-sensitive amplification," *Opt. Lett.*, vol. 29, pp. 2357–2359, 2004.
- [71] Z. Li, Y. Dong, J. Mo, Y. Wang, and C. Lu, "Cascaded all-optical wavelength conversion for RZ-DPSK signal based on four-wave mixing in semiconductor optical amplifier," *Photon. Technol. Lett.*, vol. 16, pp. 1685–1687, 2004.
- [72] V. S. Grigoryan, M. Shin, P. Devgan, J. Lasri, and P. Kumar, "SOA-based regenerative amplification of phase-noise-degraded DPSK signals: dynamic analysis and demonstration," *J. Lightw. Technol.*, vol. 24, pp. 135–142, 2006.
- [73] I. Kang, C. Dorrer, L. Zhang, M. Rasras, L. Buhl, A. Bhardwaj, S. Cabot, M. Dinu, X. Liu, M. Cappuzzo, L. Gomez, A. Wong-Foy, Y. F. Chen, S. Patel, D. T. Neilson, J. Jacques, and C. R. Giles, "Regenerative all optical wavelength conversion of 40-Gb/s DPSK signals using a semiconductor optical amplifier Mach-Zehnder interferometer," in *Proc. ECOC 2005*, vol. 6, pp. 29–30, 2005.
- [74] P. Vorreau, A. Marculescu, J. Wang, G. Bottger, B. Sartorius, C. Bornholdt, J. Slovak, M. Schlak, C. Schmidt, S. Tsadka, W. Freude, and J. Leuthold, "Cascadability and regenerative properties of SOA all-optical DPSK wavelength converters," vol. 18, pp. 1970–1972, Sept. 15, 2006.
- [75] B. Sartorius, C. Bornholdt, J. Slovak, M. Schlak, C. Schmidt, A. Marculescu, P. Vorreau, S. Tsadka, W. Freude, and J. Leuthold, "All-optical DPSK wavelength converter based on MZI with integrated SOAs and phase shifters," in *Proc. OFC 2006*, paper OWS6, 2006.
- [76] T. Tekin, "Semiconductor based true all-optical synchronous modulator for 3R regeneration," in *Proc. ECOC 2003*, vol. 3, pp. 794–795, 2003.
- [77] B. Sartorius, "All-optical clock recovery for 3R optical regeneration," in *Proc. OFC 2001*, paper MG7, 2001.
- [78] J. Leuthold, B. Mikkelsen, G. Raybon, C. H. Joyner, J. L. Pleumeekers, B. I. Miller, K. Dreyer, and R. Behringer, "All-optical wavelength conversion between 10 and 100

- Gb/s with SOA delayed-interference configuration,” *Opt. Quantum Electron.*, vol. 33, pp. 939–952, 2001.
- [79] J. Leuthold, P. A. Besse, J. Eckner, E. Gamper, M. Dulk, and H. Melchior, “All-optical space switches with gain and principally ideal extinction ratios,” *J. Quantum Electron.*, vol. 34, pp. 622–633, 1998.
- [80] O. Leclerc, P. Brindel, D. Rouvillain, B. Dany, R. Brenot, A. Labrousse, A. Coquelin, and B. Dagens, “Regenerated 4 Gbit/s long-haul transmission using all-optical SOA-MZI as loss-free synchronous modulator,” in *Proc. OFC 2001*, paper WF6-1, 2001.
- [81] C.-S. Bres, A. O. J. Wiberg, B. P.-P. Kuo, J. M. Chavez-Boggio, C. Marki, N. Alic, and S. Radic, “Single-gate 320-to-8×40 Gb/s demultiplexing,” in *Proc. OFC 2009*, postdeadline paper PA4, 2009.
- [82] F. Parmigiani, L. Provost, P. Petropoulos, and D. Richardson, “Multi-wavelength all-optical regeneration techniques,” in *IEEE/LEOS Summer Topicals*, 2009 (invited).
- [83] G. Zarris, F. Parmigiani, E. Hugues-Salas, R. Weerasuriya, D. Hillerkuss, N. Amaya, Gonzalez, M. Spyropoulou, P. Vorreau, R. Morais, S. Ibrahim, D. Klondis, P. Petropoulos, A. Ellis, P. Monteiro, A. Tzanakaki, D. Richardson, I. Tomkos, R. Bonk, W. Freude, J. Leuthold, and D. Simeonidou, “Field Trial of WDM-OTDM transmultiplexing employing photonic switch fabric-based buffer-less bit-interleaved data grooming and all-optical regeneration,” in *Proc. OFC 2009*, postdeadline paper C10, 2009.
- [84] D. Marcuse, “Calculation of bit-error probability for a lightwave system with optical amplifiers and post-detection Gaussian noise,” *J. Lightw. Technol.*, vol. 9, pp. 505–513, 1991.
- [85] G. Agrawal, *Fiber-Optic Communication Systems, 3rd Edition*. John Wiley & Sons, Inc., 2002.

Acknowledgements (German)

Die vorliegende Arbeit entstand während meiner Tätigkeit am Institut für Photonik und Quantenelektronik (IPQ) des Karlsruher Instituts für Technologie. Sie war teilweise eingebunden in das Europäische Forschungsprojekt TRIUMPH (Grant IST-027638 STP). Eine große Anzahl von Personen hat in den letzten Jahren direkt oder indirekt zum Gelingen dieser Arbeit beigetragen. Es bleibt mir zum Abschluss die erfreuliche Aufgabe, all diesen Personen zu danken.

An erster Stelle möchte ich mich bei meinem Doktorvater Prof. Jürg Leuthold, dem Leiter des IPQ, für sein stetiges Interesse an meiner Arbeit, für die Freiräume und das entgegengebrachte Vertrauen bedanken. Sein mitreißender Optimismus und sein fachlicher Überblick haben mir seit den ersten gemeinsamen Experimenten 2003 den Weg aus manchem wissenschaftlichen Tal gewiesen.

Bedanken möchte ich mich auch bei Prof. Wolfgang Freude, meinem zweiten Betreuer, für die vielen fruchtbaren fachlichen Diskussionen und die ansteckende Neugier beim Beantworten schwieriger wissenschaftlicher Fragen. Prof. Freude hat mir außerdem Sensibilität im Umgang mit Sprache vermittelt. Ich bedanke mich für die akribische Durchsicht vieler meiner schriftlichen Erzeugnisse, einschließlich dem vorliegenden.

Prof. Uli Lemmer, dem Leiter des Lichttechnischen Instituts (LTI), danke ich für die Übernahme des Korreferats.

Dr. Francesca Parmigiani vom Optoelectronics Reserach Centre (ORC) an der University of Southampton, Großbritannien, danke ich für die erfolgreiche experimentelle Zusammenarbeit und viele erhellende Diskussionen im Zusammenhang mit faserbasierten Regeneratoren und dem OTDM-zu-WDM Subsystem. Ihre Erfahrung im Umgang mit nichtlinearen Fasern war von großem Wert. Dabei ist es uns trotz großer Anstrengungen immer wieder gelungen der harten Laborarbeit auch komische Seiten abzugewinnen.

Meinem Kollegen David Hillerkuss und Dr. Dimitrios Klonidis vom Athens Information Technology Centre (AIT), Griechenland, danke ich für die intensive Arbeit und den großen persönlichen Einsatz im Systemlabor des IPQ in der Endphase des TRIUMPF Projekts.

Bei Christos Kouloumentas vom Photonics Communications Research Laboratory, National Technical University of Athens, Griechenland, bedanke ich mich für die erfolgreiche gemeinsame Arbeit an faserbasierten Mehrkanalregeneratoren.

Für unzählige fachliche Diskussionen und viele wertvolle Anregungen möchte ich mich auch bei Dr. Periklis Petropoulos (ORC), Dr. Shalva Ben-Ezra (Finisar Corp., Nes Ziona , Israel), Rui Morais (Nokia Siemens Networks, Amadora, Portugal), Prof. Ioannis Tomkos (AIT) und Dr. Andrew Ellis (Tyndall National Institute, University College Cork, Irland) bedanken.

Für die sorgfältige Durchsicht des vorliegenden Manuskripts bedanke ich mich herzlich bei Dr. Tino Ortega-Gomez, David Hillerkuss, Prof. Christian Koos, Dr. Jan Brosi, Dr. Stelios Sygletos und Dr. Francesca Parmigiani.

Meinem Bürokollegen Andrej Marculescu danke ich für die vielfache Hilfe in Computerfragen und für die Automatisierung vieler Standardmessungen.

Meinem Kollegen René Bonk danke ich für die äußerst zuverlässige Administration des TRI-UMPH Projekts.

Ein großer Dank geht an die Studenten die zu dieser Arbeit beigetragen haben: Wei-Ting Kuo, Jorge Hueso-Giner, Andrey Efremov, Alexandra Ludwig und David Hillerkuss.

Zu Dank bin ich auch den Mitarbeitern des IPQ verpflichtet, die mich in den vergangenen Jahren in vielfältiger Weise unterstützt haben. Bei Frau Goldmann, Frau Kober und Bernadette Lehmann bedanke ich mich für die administrative Unterstützung und für zuviel Leckeres zwischendurch. Bei Herrn Podszus bedanke ich mich für die Unterstützung in elektronischen Fragen. Dank gebührt auch Herrn Bürger, Herrn Hirsch und Herrn Höhne aus der mechanischen Werkstatt und Oswald Speck aus dem Packaging Labor für die schnelle und saubere Ausführung von vielen kleinen Aufträgen.

Bei allen Kollegen am IPQ bedanke ich mich herzlich für die gute Zusammenarbeit, für die Hilfsbereitschaft und für viele schöne gemeinsame Erlebnisse, auch außerhalb des IPQ: Dr. Christopher Poulton, Prof. Christian Koos, Thomas Vallaitis, Dr. Jan Brosi, Dr. Gunnar Böttger, Dr. Stelios Sygletos, René Bonk, David Hillerkuss, Andrej Marculescu, Moritz Röger, Jingshi Li, Dr. Jin Wang und Dr. Ayan Maitra.

Meinen Eltern Sabine und Lothar Vorreau sowie meinem Bruder Felix und meiner Großmutter Hanna Ecker danke ich für die selbstlose Unterstützung, auf die ich mich immer verlassen konnte.

List of Own Publications

Patents

- P1 D. C. Kilper, J. Leuthold, **P. Vorreau**, “Optical Performance Monitoring using a Semiconductor Optical Amplifier,” US patent 7154665, issued on December 26, 2006.

Journal Papers

- J7 C. Koos, **P. Vorreau**, T. Vallaitis, P. Dumon, W. Bogaerts, R. Baets, B. Esembeson, I. Biaggio, T. Michinobu, F. Diederich, W. Freude, and J. Leuthold, “All-optical high-speed signal processing with silicon-organic hybrid slot waveguides,” *Nat. Photon.*, vol. 3, pp. 216–219, 2009.
- J6 A. D. Ellis, D. Cotter, S. Ibrahim, R. Weerasuriya, C. W. Chow, J. Letuhold, W. Freude, S. Sygletos, **P. Vorreau**, R. Bonk, D. Hillerkuss, I. Tomkos, A. Tzanakaki, C. Kouloumentas, D. J. Richardson, P. Petropoulos, F. Parmigiani, G. Zarris, D. Simeonidou, “Optical Interconnection of Core and Metro Networks,” *J. Opt. Netw.*, vol. 7, pp. 928-935, 2008 (**invited**).
- J5 Ch. Kouloumentas, **P. Vorreau**, L. Provost, P. Petropoulos, W. Freude, J. Leuthold, I. Tomkos, “Investigation of the All-Fiberized Dispersion-Managed Multi-Channel Regenerator at 43 Gb/s,” *Photon. Technol. Lett.*, vol. 20, pp. 1854-1856, 2008.
- J4 J. Wang, A. Marculescu, J. Li, **P. Vorreau**, S. Tzadok, S. Ben Ezra, W. Freude, J. Leuthold, “Pattern Effect Removal Technique for Semiconductor Optical Amplifier-Based Wavelength Conversion,” *Photon. Technol. Lett.*, vol. 19, pp. 1955-1957, 2007.
- J3 **P. Vorreau**, A. Marculescu, J. Wang, G. Böttger, B. Sartorius, C. Bornholdt, J. Slovak, M. Schlak, C. Schmidt, S. Tsadka, W. Freude, J. Leuthold, “Cascadability and Regenerative Properties of SOA All-Optical DPSK Wavelength Converters,” *Photon. Technol. Lett.*, vol. 18, pp. 1970-1972, 2006.
- J2 **P. Vorreau**, D. C. Kilper, and C. A. White, “Gain Saturation Spectrum of Backward-Pumped Broad-band Raman Amplifiers,” *Photon. Technol. Lett.*, vol. 17, pp. 1405-1407, 2005.

- J1 **P. Vorreau**, D. C. Kilper, and J. Leuthold, "Optical Noise and Dispersion Monitoring With SOA-Based Optical 2R Regenerator," *Photon. Technol. Lett.*, vol. 17, pp. 244-246, 2005.

Conference Contributions

- C35 G. Zarris, F. Parmigiani, E. Hugues-Salas, R. Weerasuriya, D. Hillerkuss, N. Amaya Gonzales, M. Spyropoulos, **P. Vorreau**, R. Morais, S.K. Ibrahim, D. Klondis, P. Petropoulos, A.D. Ellis, P. Monteiro, A. Tzanakaki, D. Richardson, I. Tomkos, R. Bonk, W. Freude, J. Leuthold, and D. Simeonidou, "Field Trial of WDM-OTDM Transmultiplexing Employing Photonic Switch Fabric-Based Bufferless Bit-Interleaved Data Grooming and All-Optical Regeneration," in *Proc. OFC 2009*, paper PDPC10, 2009.
- C34 R. Bonk, S. Sygletos, R. Brenot, T. Vallaitis, A. Marculescu, **P. Vorreau**, J. Li, W. Freude, F. Lelarge, G. H. Duan, J. Leuthold, "Optimum Filter for Wavelength Conversion with QD-SOA," in *Proc. CLEO/QEC 2009*, paper CMC6, 2009.
- C33 F. Parmigiani, **P. Vorreau**, L.A. Provost, K. Mukasa, M. Takahashi, M. Tadakuma, P. Petropoulos, D. J. Richardson, W. Freude, J. Leuthold, "2R Regeneration of Two 130 Gbit/s Channels within a Single Fiber," in *Proc. OFC 2009*, paper JThA56, 2009.
- C32 R. Bonk, R. Brenot, C. Meuer, T. Vallaitis, A. Tussupov, J.C. Rode, S. Sygletos, **P. Vorreau**, F. Lelarge, G. Duan, H. Krimmel, T. Pfeiffer, D. Bimberg, W. Freude, J. Leuthold, "1.3/1.5 μm QD-SOAs for WDM/TDM GPON with Extended Reach and Large Upstream/Downstream Dynamic Range," in *Proc. OFC 2009*, paper OWQ1, 2009.
- C31 G. Zarris, **P. Vorreau**, D. Hillerkuss, S.K. Ibrahim, R. Weerasuriya, A. D. Ellis, J. Leuthold, D. Simeonidou, "WDM-to-OTDM Traffic Grooming by Means of Asynchronous Retiming," in *Proc. OFC 2009*, paper OThJ6,, (2009).
- C30 P. Petropoulos, L. Provost, F. Parmigiani, C. Kouloumentas, C. Finot, K. Mukasa, **P. Vorreau**, I. Tomkos, S. Sygletos, W. Freude, J. Leuthold, A. D. Ellis, D. J. Richardson, "Simultaneous 2R regeneration of WDM signals in a single optical fibre," in *Proc. LEOS Winter Topicals*, paper We2.2, 2009 (**invited**).
- C29 **P. Vorreau**, D. Hillerkuss, F. Parmigiani, S. Sygletos, R. Bonk, P. Petropoulos, D. Richardson, G. Zarris, D. Simeonidou, S. Ben Ezra, S. Tsadka, W. Freude, J. Leuthold, "2R/3R Optical Grooming Switch with Time-Slot Interchange," in *Proc. ECOC 2008*, paper Th.3.F.4, 2008.
- C28 W. Freude, C. Koos, J.-M. Brosi, **P. Vorreau**, P. Dumon, R. Baets, B. Esembeson, I. Biaggio, T. Michinobu, F. Diederich, L. Zimmermann, and J. Leuthold, "Silicon

- Photonics for Linear and Nonlinear Signal Processing,” *Fifth Joint Symposium on Opto- and Microelectronic Devices and Circuits (SODC 2008)*, 2008.
- C27 **P. Vorreau**, Ch. Kouloumentas, L. Provost, I. Tomkos, W. Freude, J. Leuthold, “Simultaneous Processing of 43 Gb/s WDM Channels by a Fiber-Based Dispersion-Managed 2R Regenerator” in *Proc. ECOC 2008*, paper Th.1.B.3, 2008.
- C26 C. Koos, J. Brosi, **P. Vorreau**, T. Vallaitis, P. Dumon, R. Baets, B. Esembeson, I. Biaggio, T. Michinobu, F. Diederich, W. Freude, J. Leuthold, “Silicon-Organic Hybrid (SOH) Devices for Optical Signal Processing,” in *Frontiers in Optics, OSA Technical Digest (CD)*, paper FMG6, 2008.
- C25 **P. Vorreau**, F. Parmigiani, K. Mukasa, M. Ibsen, P. Petropoulos, D. Richardson, A. Ellis, W. Freude, J. Leuthold, “TDM-to-WDM Conversion from 130 Gbit/s to 3 x 43 Gbit/s Using XPM in a NOLM Switch,” in *Proc. ICTON 2008*, PDP Th.PD.1, 2008.
- C24 S. Sygletos, R. Bonk, **P. Vorreau**, T. Vallaitis, J. Wang, W. Freude, J. Leuthold, C. Meuer, D. Bimberg, R. Brenot, F. Lelarge, G.H. Duan, “A wavelength conversion scheme based on a quantum-dot semiconductor optical amplifier and a delay interferometer,” in *Proc. ICTON 2008*, paper We.B2.5, 2008.
- C23 J. Li, J. Wang, A. Marculescu, **P. Vorreau**, Z. Zhang, W. Freude, J. Leuthold, “All-Optical SOA-based Wavelength Converter Assisted by Optical Filters with Wide Operation Wavelength and Input Power Range,” in *Proc. APOC 2008*, paper 7135-82, 2008.
- C22 R. Bonk, C. Meuer, T. Vallaitis, S. Sygletos, **P. Vorreau**, S. Ben Ezra, S. Tsadka, A. R. Kovsh, I. L. Krestnikov, M. Laemmlin, D. Bimberg, W. Freude, J. Leuthold, “Single and Multiple Channel operation Dynamics of Linear Quantum-Dot Semiconductor Optical Amplifier,” in *Proc. ECOC 2008*, paper Th.1.C.2, 2008.
- C21 J. Leuthold, W. Freude, S. Sygletos, **P. Vorreau**, R. Bonk, D. Hillerkuss, I. Tomkos, A. Tzanakaki, C. Kouloumentas, D. J. Richardson, P. Petropoulos, F. Parmigiani, A. Ellis, D. Cotter, S. Ibrahim, R. Weerasuriya, “An All-Optical Grooming Switch to Interconnect Access and Metro Ring Networks,” in *Proc. ICTON 2008*, paper Wd.C3.4, 2008 (**invited**).
- C20 W. Freude, J.-M. Brosi, C. Koos, **P. Vorreau**, L.C. Andreani, P. Dumon, R. Baets, B. Esembeson, I. Biaggio, T. Michinobu, F. Diederich, and J. Leuthold, “Silicon Photonics Meets Nonlinear Organic Materials,” in *Proc. COST-MP0702 Workshop and WG Meeting*, paper P2.3.1, 2008.
- C19 **P. Vorreau**, F. Parmigiani, M. Ibsen, P. Petropoulos, D. J. Richardson, W. Freude, and J. Leuthold : “TDM-to-WDM Conversion based on NOLM from 128.1 Gbit/s to 3x42.7 Gbit/s,” *VDE ITG Fachtagung Photonische Netze 2008*, 2008.
- C18 C. Koos, **P. Vorreau**, P. Dumon, R. Baets, B. Esembeson, I. Biaggio, T. Michinobu, F. Diederich, W. Freude, and J. Leuthold: „Highly-Nonlinear Silicon Photonics Slot Waveguide,“ in *Proc.OFC 2008*, PDP25, 2008.

- C17 R. Bonk, S. Sygletos, **P. Vorreau**, T. Vallaitis, J. Wang, W. Freude, J. Leuthold, R. Brenot, F. Lelarge, G. H. Duan: "Performance analysis of an interferometric scheme for media with limited cross-phase modulation nonlinearity," in *Proc. CSNDSP 2008*, pp. 487-491, 2008 (**Best Paper Award**).
- C16 R. Bonk, **P. Vorreau**, S. Sygletos, T. Vallaitis, J. Wang, W. Freude, J. Leuthold, R. Brenot, F. Lelarge, G. H. Duan, C. Meuer, S. Liebich, M. Laemmlin, D. Bimberg: "An Interferometric Configuration for Performing Cross-Gain Modulation with Improved Signal Quality," in *Proc. OFC 2008*, paper JWA70, 2008.
- C15 S. Schuele, U. Hollenbach, **P. Vorreau**, A. Efremov, J. Li, J. Mohr, J. Leuthold, "Modular Integration of Microactuators and Micro-Optical Benches," in *Proc. Photonics Europe 2008*, paper 699202/1-12, 2008.
- C14 A. Marculescu, J. Wang, J. Li, **P. Vorreau**, S. Zadok, S. Ben Ezra, S. Tsadka, W. Freude, J. Leuthold, "Pattern effect removal technique for semiconductor optical amplifier-based wavelength conversion," in *Proc. ECOC 2007*, paper Tu3.4.6, 2007.
- C13 J. Leuthold, J. Wang, T. Vallaitis, Ch. Koos, R. Bonk, A. Marculescu, **P. Vorreau**, S. Sygletos, W. Freude, "New Approaches to Perform All-Optical Signal Regeneration," in *Proc. ICTON 2007*, paper We.D2.1, 2007.
- C12 S. Sygletos, M. Spyropoulou, **P. Vorreau**, R. Bonk, I. Tomkos, W. Freude, and J. Leuthold, "Multi-wavelength Regenerative Amplification based on Quantum-Dot Semiconductor Optical Amplifiers," in *Proc. ICTON 2007*, paper We.D2.5, 2007 (**invited**).
- C11 J. Leuthold, W. Freude, G. Boettger, J. Wang, A. Marculescu, **P. Vorreau**, R. Bonk, "All-Optical Regeneration," in *Proc. ICTON 2006*, (**invited**).
- C10 W. Freude, J. Leuthold, **P. Vorreau**, A. Marculescu, J. Wang, G. Böttger, "All-Optical Processing of Novel Modulation Formats Using Semiconductor Optical Amplifiers," in *Frontiers in Optics, OSA Technical Digest (CD)*, paper FTuV1, 2006.
- C9 J. Leuthold, W. Freude, J. Wang, **P. Vorreau**, A. Marculescu, "A novel all-optical DPSK wavelength converter based on Semiconductor Optical Amplifier (SOA) nonlinearities," *Workshop der ITG Fachgruppe 5.3.1; "Modellierung photonischer Komponenten und Systeme "*, 2006.
- C8 J. Leuthold, W. Freude, **P. Vorreau**, A. Marculescu, J. Wang, G. Böttger, "All-optical signal processing for phase-sensitive modulation formats," in *Proc. APOC 2006*, Paper 635311, (2006) (**invited**).
- C7 D. C. Kilper, C. White, S. Chandrasekhar, W. Etter, M. Waldow, and **P. Vorreau**, "Amplifier Dynamics in Optically Transparent Mesh Networks," in *Proc. COIN-NGNCON 2006*, paper P1299, 2006.
- C6 B. Sartorius, C. Bornholdt, J. Slovak, M. Schlak, Ch. Schmidt, A. Marculescu, **P. Vorreau**, S. Tsadka, W. Freude, J. Leuthold, "All-Optical DPSK Wavelength Con-

- verter Based on MZI with Integrated SOAs and Phase Shifters,” in *Proc. OFC 2006*, paper OWS6, 2006.
- C5 J. Leuthold, W. Freude, G. Boettger, J. Wang, **P. Vorreau**, A. Marculescu, “Trends in the Field of All-Optical Wavelength Conversion and Regeneration for Communication up to 160 Gb/s,” in *Proc. ECOC 2005*, 2005 (**invited**).
- C4 D. C. Kilper, W. Weingartner, C. Xie, A. Azarov, **P. Vorreau**, and J. Leuthold, “Network Applications and Metrics for Optical Performance Monitoring,” in *Proc. OECC 2005*, 2005 (**invited**).
- C3 D. C. Kilper, C. R. Giles, W. Weingartner, A. Azarov, **P. Vorreau**, J. Leuthold “Optical performance monitoring applications in transparent networks,” in *Proc. WOCC 2005*, 2005.
- C2 D. C. Kilper, A. Azarov, W. Weingartner, **P. Vorreau**, “Q-Factor Monitoring for Fault Management Applications,” in *Proc. OFC 2004*, paper FH3, 2004.
- C1 D. C. Kilper, **P. Vorreau**, J. Leuthold, “Noise and Distortion Monitoring in an SOA-based Optical 2R Regenerator,” in *Proc. ECOC 2003*, paper We4.P.132, 2003.

Curriculum Vitae

Philipp Vorreau

born July 7, 1977

in Hamburg, Germany

Citizenship: German

Education

- 11/03 – 06/09** PhD studies at the Institute of Photonics and Quantum Electronics (IPQ), University of Karlsruhe, Germany.
- 03/03 – 08/03** Diploma Thesis, Lucent Technologies, Bell Laboratories, Advanced Photonics Research Group, New Jersey, USA.
- 03/00 – 09/03** Dipl.-Ing., Studies of Electrical Engineering, Flensburg University of Applied Sciences, Germany. Specialization in Optical Communications.
- 03/99 – 02/00** Studies of Electrical Engineering, Hamburg University of Applied Sciences, Germany.
- 08/88 – 06/97** Alexander-von-Humboldt-Gymnasium Hamburg (secondary school), Germany.

Internships and Work Experience

- 06/04 – 08/04** Visiting Scientist, Lucent Technologies, Bell Laboratories, Advanced Photonics Research Group, New Jersey, USA. Work on gain saturation in Raman amplifiers.

- 04/02 – 08/02** Internship, Pandatel AG, Development Department, Hamburg, Germany.
Work on protection switching in optical transceivers.
- 09/98 – 02/99** Mandatory internship, Still GmbH, Mechanical Workshop and Development Department, Hamburg, Germany.
- 09/97 – 09/98** Civilian service, Elbe Werkstätten GmbH, sheltered workshop, Hamburg, Germany.

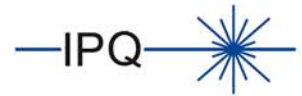
Scholarships and Awards

- 06/04 – 08/04** Scholarship, Lucent Technologies, Early Career Identification Program.
- 11/03** Prof. Dr. Werner Petersen Technology Award for outstanding diploma thesis.
- 10/01 – 07/03** Study Scholarship, Studienstiftung des deutschen Volkes (German National Academic Foundation).

Karlsruhe Series in Photonics & Communications, Vol. 6

Edited by Prof. J. Leuthold and Prof. W. Freude

Karlsruhe Institute of Technology
Institute of Photonics and Quantum Electronics (IPQ)
Germany



High-speed traffic aggregation with switching capability in time, space and wavelength will be key for the interconnection of future high-bitrate metro and core networks. Using wavelength division multiplexing (WDM), 43 Gbit/s per wavelength is emerging as a viable bit rate in metro networks. It is expected that such traffic will be transported by the core network in serial form resulting in a line rate close to 130 Gbit/s. Therefore, grooming from 43 Gbit/s to 130 Gbit/s through optical time-division multiplexing (OTDM) in the switch of an edge node will be required when moving from metro to core networks. However, dynamic OTDM channel grooming functionalities are currently unavailable in the optical layer.

In this book a novel optical switch is designed, developed, and tested. The switch integrates optical switching, transparent traffic aggregation/grooming, and optical regeneration. Innovative switch subsystems are developed that enable these functionalities, including all-optical OTDM-to-WDM converters. High capacity ring interconnection between metro-core rings, carrying 130 Gbit/s OTDM traffic, and metro-access rings carrying 43 Gbit/s WDM traffic is experimentally demonstrated. The developed switch features flexibility in bandwidth provisioning, scalability to higher traffic volumes, and backward compatibility with existing network implementations in a future-proof way.

About the Author

Philipp Vorreau was born in 1977 in Hamburg, Germany. In 2003 he received the Dipl.-Ing. (FH) degree in Electrical Engineering from the University of Applied Sciences Flensburg, Germany, and in 2010 the Dr.-Ing. (PhD) degree from Karlsruhe Institute of Technology, Germany. His research is focused on high-speed opto-electronic and all-optical signal processing, and on design, implementation and characterization of optical communication systems.

ISSN 1865-1100
ISBN 978-3-86644-502-4

